Aerodynamic wake study: oscillating model wind turbine within a turbulent boundary layer

A THESIS
SUBMITTED TO THE FACULTY OF THE GRADUATE SCHOOL
OF THE UNIVERSITY OF MINNESOTA
BY

Christopher J. Feist

IN PARTIAL FULFILLMENT OF THE REQUIREMENTS
FOR THE DEGREE OF
MASTER OF SCIENCE

Michele Guala

March, 2015

Acknowledgements

There are many people that have earned my gratitude for their contribution to my time in graduate school. I would first like to thank my adviser, Michele Guala, who helped guide my research, providing important insight, experience and support. I would also thank Leonardo Chamorro and Kevin Howard, who pioneered much of the wind energy research performed at the St Anothony Falls Laboratory. The next group consists of the technical staff and research engineers at the St Anthony Falls Laboratory, who aided with the experimental apparatus and model designs. This group includes, but is not limited to, Jim Tucker, Erik Steen, Christopher Ellis, James Mullin, Richard Christopher, Ben Erickson, and Matthew Lueker. I would also like to thank my friends and family who provided support during this challenging time in my egineering career. Specifically my parents Ken and Ellie Feist, brother and sister Justin and Kim Feist, close friends Bill Bloomenkranz and Chris Krajnik, and most recently Jesiah Collective. Lastly, the United States Department of Energy whose funding through DE-EE0005482 project supported this work.

Dedication

To those who held me up over the years, family, friends, and the research staff at the St Anthony Falls Lab.

Abstract

An experimental investigation on the aerodynamic wake behind a pitching and/or heaving model wind turbine was performed. The study was split into two quasi-coupled phases; the first phase characterized the motion of an offshore floating wind turbine subjected to linear wave forcing, the second phase replicated specific motion cases, which were driven by results from the first phase, on a model wind turbine within a turbulent boundary layer. Wake measurements were made in an effort to quantify fluctuations in the flow associated with the motion of the turbine. Weak differences were observed in the mean, streamwise velocity and turbulent fluctuations between the static and oscillating turbine cases, $< 3\%$ of U_{hub} everywhere. These weak differences were a result of opposing trends in the mean and fluctuating velocity quantities based on turbine motion phases. The wake oscillations created by the turbine motion was characteristic of a 2D wave (with convection in the x plane and amplitude in the z plane) with a relatively small amplitude as compared to u_{rms}, ΔU_{ξ} value of $\pm 30 - 40\%$ of the u_{rms} for the static turbine. However, the lengthscale of the oscillation is relatively large, $3-4$ rotor diameters, and organized with respect to the wave frequency. Therefore, the turbine structure and controls (generator and blade pitch control) should perceive the fluctuations and make corrections.

Contents

List of Tables

List of Figures

Chapter 1

Introduction

In the past decade, US and worldwide efforts have been aimed at diversifying the energy portfolio, with special interest in increasing efficiency and reducing greenhouse gases. A collaborative effort was started in the US with the goal of reducing greenhouse gas emissions, increase energy independence, and explore the potential role wind energy could play. The result of the effort concluded wind energy would be a necessary component of a diverse energy portfolio and set an ambitious goal of 20% of the nation's energy production from wind by 2030, proposed by the US Department of Energy [1]. Of the required 300 GW of additional wind energy capacity needed to meet this goal, a least-cost optimization model performed by the National Renewable Energy Laboratory (NREL) found that 54 GW could come from offshore wind, this is approximately 18 percent of the total. The authors predicted the potential for energy capture by offshore wind turbines located along the East Coast, West Coast, Gulf of Mexico, Great Lakes, and Hawaii at four times the current U.S. electric capacity [2]. Figure 1.1, reprinted from [2], shows the wind energy resource in GW by region and water depth. Of the estimated energy capacity for offshore wind, approximately 59% is located at water depths greater than 60 meters. At this depth it is no longer economically feasible to have the wind turbine rigidly fixed to the sea floor [2], this is with respect to installation and material costs. As a result, using floating platforms as a means of deploying wind turbines into deep waters may be required.

Offshore wind energy has largely relied on the technology developed for land-based wind turbines as well as adapting structures from the oil and gas industry. As such,

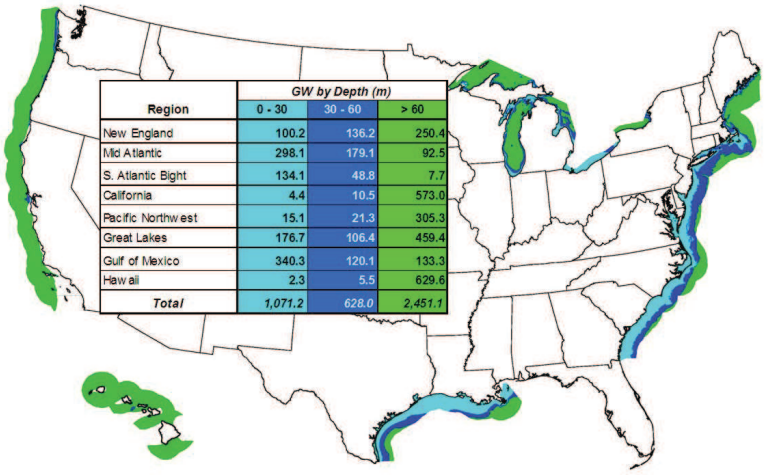

Figure 1.1: United States offshore wind resource by water depth for sites with annual average wind speeds above 7.0 m s^{-1} extending 50 mi from shore [2]

floating structure survivability has been successfully proven in the oil industry, however, applying the technology to wind turbines has seen limited application. Currently there exists two demonstrations of floating platform use at utility-scale offshore wind capture. The Principle Power WindFloat prototype was installed in 2011 off the coast of Portugal employing a 2 MW wind turbine [3]. In 2009, Hywind deployed a 2.3 MW turbine in the North Sea off the coast of Norway.

Floating platform concepts as applied to wind turbines are classified into three major categories with respect to the physical principle in which stability is achieved [4]. The three categories are: ballast, mooring line, and buoyancy stabilized. Figure 1.2 shows the different types of platforms. The ballast class achieves stability by having a center of gravity below the center of buoyancy. When the system is perturbed from equilibrium, a righting moment is created by a torque arm represented by the horizontal distance between the center of buoyancy and center of gravity. One example of this type of platform is the spar-buoy, the first platform type on the left in figure 1.2. The mooring line class uses mooring line tension attached to a buoyancy tank and the sea floor for stability. Perturbations from equilibrium are restricted due to the line tension. Lastly, the buoyancy class uses a large water plane area and it's distribution of buoyancy in the horizontal plane to achieve stability. There are advantages and disadvantages to

each platform type with respect to production, deployment, and maintenance costs, as well as kinematic characteristics, i.e. pitching and heaving motions and the platforms ability to limit these motions.

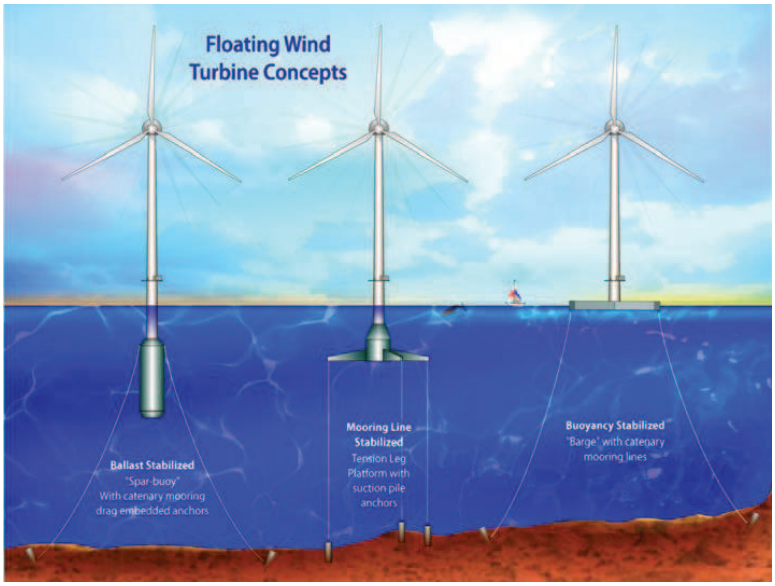

Figure 1.2: Offshore floating wind turbine platform concepts [4]

The use of a floating platform introduces a dynamic coupling between the wind and waves which results in an array of new engineering challenges. The platform must provide buoyancy for the system as well as limit the pitch, roll, and heave motion to within design constraints. These motions are influenced by wave forcing as well as the mean and fluctuating incoming flow properties. Additional stresses on turbine components such as the tower, blades, and main shaft are associated with the degrees of freedom in pitch, roll, and heave. Further, these additional degrees of freedom will have an impact on the turbine performance and wake-flow interaction which is a critical component to safe and efficient wind farm siting.

Of great interest to the field of wind turbine engineering is the inflow conditions from which the wind turbine will extract energy. Available power in the wind scales with the streamwise velocity cubed, U^3. Velocity fluctuations from the mean introduces increased dynamic and fatigue loading as well as effecting the ability of the wind turbine to extract energy. Neglecting turbulence in the incoming flow can lead to overestimation

of power extraction by 10% or more as reported by [5].

As the wind passes through a wind turbine farm, downstream turbines see a reduced inflow velocity as upstream turbines extract energy from the flow. The upstream wind turbines create a region of velocity deficit known as an aerodynamic wake. The aerodynamic wake is characterized by complex turbulence structures induced by upstream turbine blades, topography, thermal stratification, and other turbine geometries. The wake region is commonly split into two regions, the near wake and the far wake [6]. The near wake is defined as the region imediately downstream of the turbine and approximately extends to 1-2 rotor diameters downstream. The near wake is characterized primarily by turbulence associated with turbine specific geometry such as tip and hub vortices. The far wake depends less on turbine geometry and more on inflow conditions as well as turbulence generated by the upstream turbine. Within a wind farm there is potential for many of the turbines to be located within the wake of upstream turbines. This leads to a need for detailed understanding and an ability to model the properties of turbine wakes.

A review of work in the field of the aerodynamic wake of land based wind turbines is summarized well in [7]. A wind tunnel investigation of the wake for a model wind turbine within a turbulent boundary is presented in [8],[9], and [10]. The former investigated the spatial distribution of the velocity deficit and turbulence intensity where the vertical inhomogeneity of the incoming boundary-layer flow is considered. Another set of work characterized the response of a model turbine due to complex inflow conditions, i.e. a turbine in the wake of a hill or turbine [11] [12]. Field scale measurements of the wake behind a single turbine using PIV is given in [13]. Experimental work has also explored wake development at the model farm scale, [14], [15], [16], [17],

Numerical models have recently been applied, at the farm scale utilizing large-eddy simulation (LES), on wind turbine wakes for floating offshore wind farms where the turbine motion is neglected, notably [18] and [19]. The focus of these studies investigated how oceanic waves effect the marine atmospheric boundary-layer and the wind farm performance. However, there is a lack of experimental research investigating how an oscillating offshore wind turbine, where the motion is induced by wind and/or waves, effects the turbine wake. This thesis is intended to start the process by which to explore the complex interactions of a moving rotor within a turbulent boundary layer.

In order to design efficient, robust, cost-effective, and safe commercial scale floating offshore wind turbines and farms, the complex wind-wave and wind-rotor interactions and their influence on the turbine wake will need to be investigated. This work covers a set of state of the art experiments designed to 1) measure the response of a model floating wind turbine to different wave and simulated wind conditions and 2) investigate the rotor wake response to various platform motions in a turbulent, atmospheric boundary layer. The primary goals are:

- define the scaling parameter space used to relate wind tunnel and wave channel experiments
- identify the range of platform oscillations under prescribed linear waves and steady or gusty wind
- and characterize the differences, if any, between the aerodynamic wake of a static turbine and that of an oscillating turbine within a turbulent boundary layer.

An additional objective of this work is to validate specific capabilities of numerical models being developed at University of Minnesota (UMN). These capabilities include turbine-wave interaction and turbine-wind interaction.

Due to limitations on experimental facilities, the problem is decoupled into two separate but related experiments. The quasi-coupled experiments, being a wave-basin study and a wind tunnel study, limit the motion of a model wind turbine to two degrees of freedom, namely heave and pitch in the vertical plane aligned with the direction of wave propagation and primary wind flow. The major challenge was to set the correct scaling and boundary conditions in each set of experiments, such that the floating turbine model is subjected to the effect of realistic waves and mean wind shear and incoming turbulent flow conditions, with the rotor extending up to 25% of the boundary layer height. These constraints were satisfied using the 80 m long St. Anthony Falls Laboratory (SAFL) wave testing facility (Phase I) and the SAFL atmospheric wind tunnel (Phase II).

Phase I includes scale model tests, at 1/100 scale, of a Sandia National Laboratories (SNL) 13.2 MW prototype offshore floating horizontal axis wind turbine (HAWT) in a wave channel. This experimental investigation is intended to describe the basic and

complex kinematics of a floating turbine system under the effect of both waves and variable wind. While the waves are reproduced in the laboratory, wind is accounted for through a variable thrust force induced by a controlled spinning rotor. The thrust force is further coupled to the wave-induced platform oscillation through a open-loop control system designed to mitigate platform pitch. Under the limiting constraint of two allowable degrees of freedom, platform pitch and heave, the floating turbine system is investigated under realistic oceanic and atmospheric conditions, including the effect of large scale wind gusts consistent with the signature of the meandering wake generated by an upwind turbine. The parameter space investigated includes variability in wave height, length, and period, wind magnitude, wind gust amplitude and period, thus covering a wide range of platform heave and pitch motions that will serve as benchmark experiments for coupled wind-wave numerical simulations.

Phase II experiments are designed to investigate the turbine-wind interaction of a scale model under pitching and heaving motions in a turbulent boundary layer, experiments conducted in the SAFL closed return wind tunnel. These model tests are performed at 1/1562.5 scale (prototype to wind tunnel scale). Constant temperature anemometer (CTA) cross-wire and wall-parallel particle image velocimetry (PIV) is used to study the aerodynamic wake development of the pitching and heaving model turbine. The parameter space includes pitch and heave amplitude and frequency of the motion. Motion data sets recorded in Phase I are used to prescribe the wind turbine model (scaled) motion which is implemented through a synchronized linear actuator system.

The focus of this thesis is outlined in the following chapters:

- Description of the prototype 13.2 MW SNL floating offshore wind turbine is presented in Chapter 2. This includes geometric dimensions, mass properties, performance characteristics, and stability characteristics of the wind turbine system.

- Wave channel experimental setup including sections on the wave channel experimental facility, prototype model and scale model development, wind-wave environment, and data acquisition and control system is discussed in chapter 3.

- Chapter 4 presents the wave channel test procedure. This includes free decay testing, response amplitude operator (RAO) procedure and calcuations, gerneration of variable thrust, and a pitch control strategy to be implemented.

- Chapter 5 discusses the wave channel results. Specifically results are presented for the free decay tests, linear response characteristics, or RAOs, effect of rotor thrust on platform dynamics, and a subset of experiments on pitch mitigation through open-loop control of rotor speed based on current platform pitch.

- Chapter 6 overviews the experimental setup for Phase II work. The chapter includes sections on the closed-circuit atmospheric wind tunnel and turbulent boundary layer generation and characteristics, wind turbine model overview and scaling, data acquisition and motion control hardware, and the electro-mechanical system used to realize the turbine motion.

- Results of the aerodynamic wake study, primarily streamwise velocity statistics, are presented in chapter 7.

- Chapter 8 gives concluding remarks on the results of the thesis work.

Chapter 2

Prototype Wind Turbine

The prototype wind turbine used as a reference for the model testing is the SNL 13.2 MW floating offshore HAWT. Table 3.1 gives the significant geometric dimensions, mass properties, and stability characteristics. Details of the turbine development, and specifically details on the 100 m rotor blade development used on this turbine, are discussed in [20]. The prototype turbine has a 200 m rotor diameter with a hub height, as measure from mean sea level (MSL), of 119.5 m. The barge-type platform used as the floating structure has a radius R of 28.0 m and height of 15.0 m with a draft of 8.0 m. Details on the platform development are covered in §3.2.

Performance characteristics of the 13.2 MW were investigated using NREL's FAST (Fatigue, Aerodynamics, Structures, and Turbulence) code. FAST is an aeroelastic model used to predict performance and loading of horizontal-axis wind turbines. FAST has been evaluated by Germanischer Lloyd WindEnergie and was found suitable for calculating wind turbine loads for design and certification of land based wind turbines.

A second computational tool is integrated with FAST to provide wind conditions with which to subject the prototype turbine to. This tool is called IECWind and was used to generate wind profiles for simulation of the steady-state response over the operating wind speed range. Mean wind speeds ranging from cut-in velocity, 3 m s^{-1}, to cut-out velocity, 25 m s^{-1}, are modeled with the wind turbine response shown in figure 2.1 and 2.2. Figure 2.1 gives the aerodynamic steady-state thrust in kN. Thrust at cut-in is 695.1 kN and thrust at rated power is 2334.7 kN. Figure 2.2 gives rotor speed as a function of wind speed. Rotor speed varies from 4.34 rpm at cut-in to 7.44

rpm at rated power.

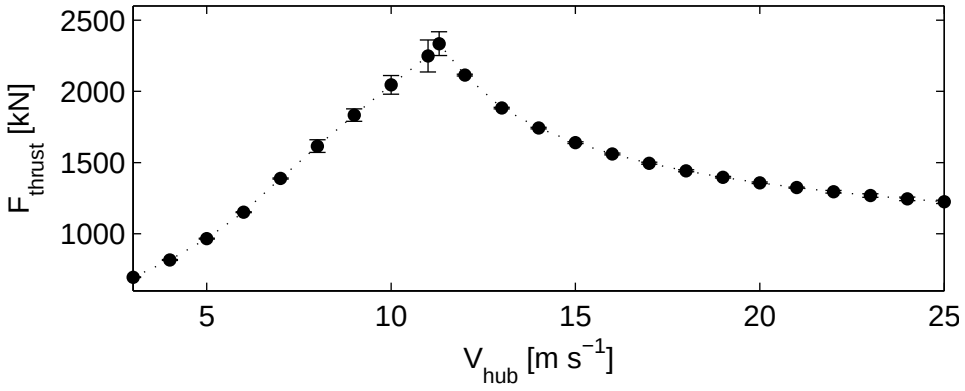

Figure 2.1: SNL 13.2 MW thrust vs wind speed, turbine is subjected to steady-state wind profile, error bars indicate thrust rms

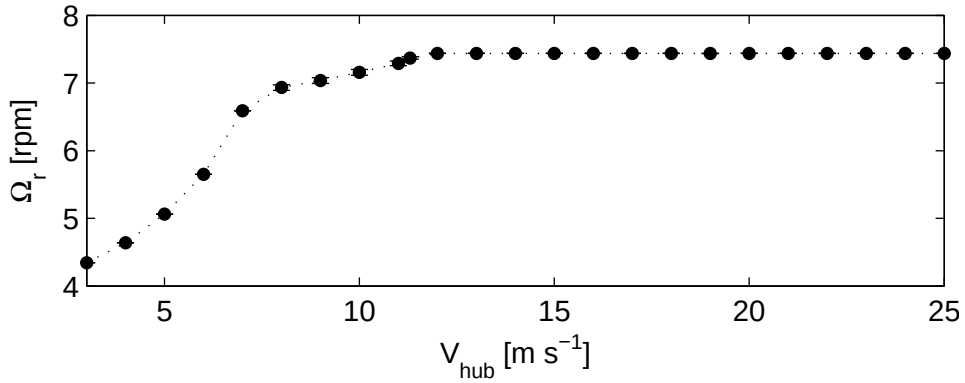

Figure 2.2: SNL 13.2 MW rotor speed vs wind speed, turbine is subjected to steady-state wind profile, error bars indicate rotor speed rms

Figure 2.3 shows the tip-speed ratio (TSR) as a function of wind speed. TSR is defined as the ratio between the tangential speed of the rotor tip and the hub height velocity V_{hub}. TSR is relatively large at slow wind speeds and decreases with increasing wind speed.

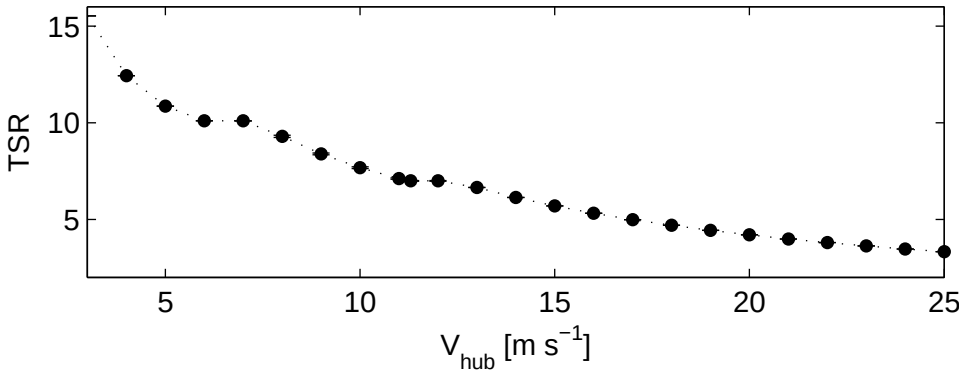

Figure 2.3: SNL 13.2 MW TSR vs wind speed, turbine is subjected to steady-state wind profile, error bars indicate TSR rms

Chapter 3

Experimental Setup: Wave Channel

3.1 Wave channel

Phase I experiments were conducted in the SAFL wave testing facility encompassing a rectangular channel (2.75 m wide, 1.8 m high, 84 m long), a hinged-paddle type wave generator, and an artificial beach located at the opposite end. The wave maker has an oscillating paddle hinged at the bottom of the channel and spanning its entire width and height. A moving stroke-arm attached to the paddle is connected through gear reducers to a 72 hp electric motor. The motor is controlled with a frequency drive able to maintain a desired rpm. All the experiments were run at a fixed water depth d of 4.5 ft, leaving the upper portion of the paddle above the water level. The angular velocity, Ω, of the rotating arm defines the period of the paddle oscillations and thus of the generated waves. The length of the arm, S, is adjustable in order to set the paddle stroke length. The wave height results from a non-linear combination of the stroke-arm length and angular velocity. A partial investigation of the $\Omega - S$ parameter space produced a desired wave height H and period T_w in a range of $[1 - 15]$ cm and $[0.6 - 3]$ s respectively.

The wave testing facility is capable of testing deep water waves, where deep water waves are defined by the condition $d/L \geq 1/2$, for wave lengths L up to 2.74 m and corresponding wave period of 1.3 s. Wave type definition based on water depth is

described in [21]. The remaining wave periods tested are classified as intermediate water depth waves. Intermediate water depth is defined by $1/20 < d/L < 1/2$.

The sloped beach is located 80 m from the paddle. The beach spans the entire width of the channel and is 6.1 m in length with an adjustable slope. The beach consists of an impermeable aluminum panel covered in permeable CavClear Masonry Mat with a thickness of 1.75 in. The optimal configuration was determined by subjecting the beach to various wave lengths. However, due to design limitations, as the beach needed to be easily removed, it was concluded the performance was not acceptable. As a result, all experiments were performed in a time window where reflected waves were not present. This clean wave window is a function of wave period and thus changed depending on the wave parameters of interest for each test. The presence of the wave absorber did aid in returning the wave channel to still water conditions after each run. Details on the clean wave window are discussed in §4.2. Figure 3.1 shows the beach installed in the wave channel.

Figure 3.1: Wave absorber setup with 10 deg. slope, 6.1 m in length, 1.75 in permeable masonry mat

3.2 Scaled turbine model

Model tests in the wave facility were performed on a 1/100 scale model of the SNL 13.2 MW prototype floating offshore wind turbine. Table 3.1 gives the prototype and experimental model parameters. The experimental model was designed to match the Froude scaled prototype parameters. Froude number similitude is used to properly scale the gravitational and inertial forces which dominate offshore platform motion [21]. This is the typical scaling scheme used in offshore platform wave basin testing. The Froude number for free surface wave is

$$Fr = \frac{C}{\sqrt{gL}}, \tag{3.1}$$

where C is the wave celerity, g is the gravitational acceleration, and L is the characteristic length which is equivalent to the platform diameter, D. The scaling relationship maintained between the prototype scale and model scale is therefore

$$Fr_p = Fr_m, \tag{3.2}$$

where p denotes prototype and m model. Table 3.1 outlines the scaling factors for prototype to model geometric and dynamic properties. The platform has a radius of 0.28 m and height of 0.15 m with 0.08 m draft. Hub height as measured from MSL is 0.986 m. The parameters governing the assumed rigid body motion of the platform and turbine, and thus of importance to model accurately, are the system mass, center of gravity, mass moment of inertia, overturning moment due to rotor thrust, and structure geometry in contact with the water, platform radius and draft. This gives a degree of freedom on hub height allowing the overall inertia and center of gravity to be tuned.

The floating platform used in these experiments is a barge type which pertains to the buoyancy stabilized category of floating platforms. The classification system for floating platforms as they relate to wind turbines is described in [4]. The buoyancy class primarily achieves stability through the water plane area, or the distribution of buoyancy in the horizontal plane. Ballast is also used achieve a desirable draft and center of gravity. This class of platform was chosen for its simple geometry which aided the ease of construction, implementation and numerical validation. Additionally, the water plane area restoring method has a significant portion of the structure at or near the free surface resulting in larger translational and rotational motion. This may lead

Table 3.1: Prototype and experimental model properties for the SNL 13.2 MW with scaling parameter $\lambda = 100$. Relevant properties are w.r.t. MSL

	Prototype model	Scale factor	Experimental model	
Platform radius	28.0	λ^{-1}	0.28	[m]
Platform height	15.0	λ^{-1}	0.15	[m]
Draft	8.0	λ^{-1}	0.8	[m]
Hub height	119.5		0.986	[m]
Rotor diameter	200.0		0.60	[m]
Mass	19704	λ^{-3}	19.704	[kg]
Center of gravity	8.580	λ^{-1}	0.858	[m]
Center of buoyancy	-4.00	λ^{-1}	-0.04	[m]
Thrust overturning moment	1.08×10^8	λ^{-4}	1.077	[N-m]
Mass moment of inertia I_y	3.82×10^{10}	λ^{-5}	3.81	[kg-m^2]
Restoring coefficient	2.30×10^9	λ^{-4}	23.040	[N-m]

to violations of the Morison equation simplifications, which many models employ, and a requirement of more complex models to accurately predict the platform dynamics [4]. The potentially large translational and rotational motions are also of greater interest in phase II where these motions will be replicated on a scale turbine in an atmospheric boundary layer.

The platform for the prototype scale was designed with a similar approach as outlined in [22]. The platform used in this experiment is based on the Massachusetts Institute of Technology/National Renewable Energy Laboratory (MIT/NREL) Shallow Drafted Barge (SDB). The MIT/NREL SDB was designed for the NREL 5 MW Offshore Baseline Wind Turbine model. For use with the SNL 13.2 MW prototype, the MIT/NREL SDB was scaled up to achieve a starting point for geometric and mass properties. Static performance of the wind turbine system in pitch was then used to fine tune geometric properties and adjust mass distribution. The static performance is defined by the floating turbine position due to steady-state forces exerted on the structure. The full 6 degrees of freedom for rigid body motion of the wind turbine system in matrix form is defined as

$$(M + A)\ddot{\xi} + B\dot{\xi} + C\xi = aXe^{\mathrm{i}\omega t}, \tag{3.3}$$

where M is the mass matrix, A is the added mass matrix, ω is the wave frequency, ξ represents the six modes of displacement: translational; surge, sway, and heave and rotational; roll, pitch, and yaw, B is the damping matrix, and C is the restoring matrix.

For steady-state performance, equation 3.3 is solved for static overturning moments and results in the following static equilibrium equation

$$C\xi = F_{steady-state}. \tag{3.4}$$

Equation 3.4 can then be solved for the steady-state pitch response due to a static overturning moment about the pitch axis giving

$$\xi_5 = \frac{F_5}{C_{55}}, \tag{3.5}$$

where ξ_5 is the static pitch response [rad], F_5 is the overturning moment in pitch [N-m], and C_{55} is the platform restoring property in pitch coefficient [N-m rad^{-1}]. F_5 is the result of aerodynamic thrust generated by the wind loading, denoted by F_{thrust}, acting on the torque arm defined by the distance from the hub to MSL, Z_{hub}. F_5 is therefore given by

$$F_5 = F_{thrust} Z_{hub}. \tag{3.6}$$

Hydrostatic and inertial properties govern the process by which a circular cylinder achieves restoring at steady-state. The hydrostatic properties consists of the waterplane area moment and the location of the center of buoyancy. The inertial properties are defined by the location of the center of mass and ballast placement. These processes result in the following equation for pitch restoring coefficient

$$C_{55,HI} = F_B Z_B - M_{11} g Z_G + \rho\pi \frac{R^4}{4}, \tag{3.7}$$

where F_B is the buoyant force, Z_B is the center of buoyancy, M_{11} is the system mass, Z_G is the center of gravity, g acceleration due to gravity, water density ρ, and R is the platform radius.

Beyond pitch angles of 10 degrees, it is speculated aerodynamic efficiency decreases substantially and therefore is used as a design limit [22]. The minimum pitch restoring moment is then determined by applying the maximum wind loading, 2330 kN at rated speed, to equation 3.5 and solving for C_{55} which gives

$$C_{55} = \frac{F_{rotor} Z_{hub}}{\xi_5} = \frac{2330 \times 10^3 \times 119.5}{0.1745} = 1.782 \times 10^9. \tag{3.8}$$

This is the minimum restoring coefficient in pitch required to limit the motion to 10 degrees of pitch. Using this result and equation 3.7, the geometric and mass properties

are tuned to achieve a desirable steady-state response in pitch. Table 3.1 gives the designed restoring coefficient of 2.30×10^9 and other properties used in equation 3.7.

Figure 3.2 is an image of the experimental setup and coordinate system. The $x-y$ plane is in the plane of MSL with the z-axis aligned with the turbine platform center and center of gravity with positive pointing up. The x-axis points with the wave propagation direction. Heave is the measure of displacement along the z-axis with zero position being defined when the turbine system is at rest. Pitch is defined as rotation about the y-axis with positive pitch being a counter-clockwise rotation when looking down the y-axis toward the origin. Zero pitch is defined as when the system is at rest.

The platform is restricted to two degrees of freedom, pitch and heave. The mechanism for achieving this is a combination of radial and linear roller bearings. Two radial bearings, one on each side, are located along the pitch axis at the center of gravity. The radial bearings allow for pitching motion and secure the platform to the linear roller bearings. Two linear roller bearings, one located on each side and directly above their respective radial bearings, restrict the platform motion in the y and x axes, and allow heaving motion. The combination of the two bearing styles prevents rotation about the z-axis, yaw, and the x-axis, roll. By attaching the bearing system to the center of gravity and along the pitch axis there are no additional and unknown forces that cannot be accounted for in the numerical models i.e. the pitch and heave damping associated with the bearings can be determined through free decay tests.

The motion of the floating wind turbine system due to regular linear waves parallel with the x-axis and wind loading is dominated by translation in heave and surge and the rotational mode pitch. These dominant modes are coupled with sway, roll, and yaw, however, responses in these modes are relatively small as compared to the dominant modes. Additionally, heave and pitch may have a significant impact on turbine-wind interaction, specifically on wake development. Yaw misalignment, with respect to wind direction and wave propagation direction does have the potential to significantly change turbine-wind interaction, however, this is not the focus of this set of experiments.

Figure 3.3 gives a schematic of the floating platform model. The model platform is constructed from a stiff, closed-cell foam cylinder compressed between two aluminum plates. The aluminum plates compress the foam cylinder via tension from four steel rods penetrating through the foam. Two steel ballast masses, cylindrical geometry, are

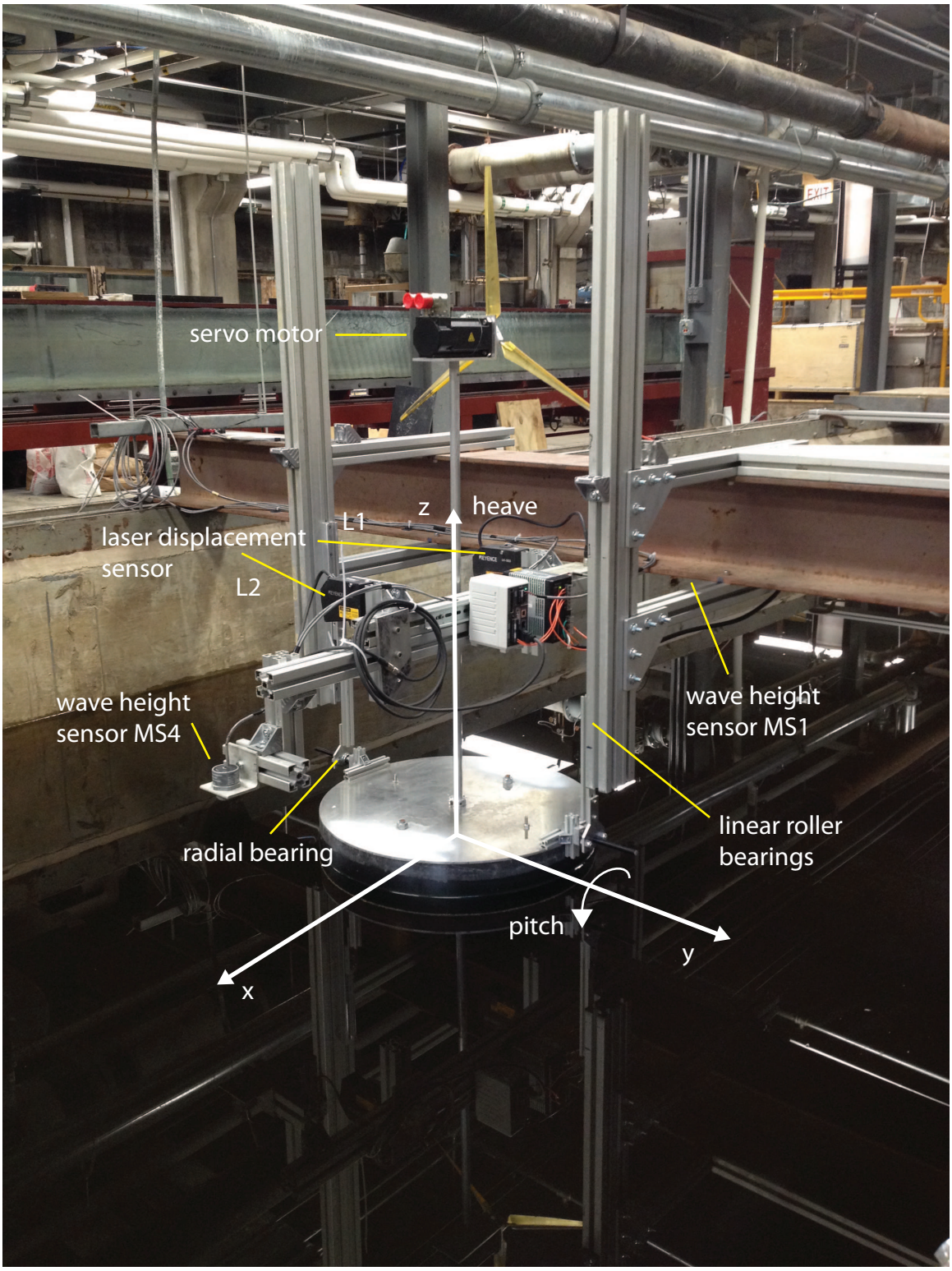

Figure 3.2: Wave Basin experimental setup

attached to two of the tension rods, where the rods extend below the platform, and are located along the x-axis. The aluminum tower is attached via aluminum tube clamp to the top and bottom aluminum plates.

3.3 Scaled wind-wave environment

For the 1/100 scale testing of the floating offshore platform, a Froude scaled combined wind and wave resource based on U.S. deployment sites was created by SNL. The scaled wind-wave resource was then used to determine experimental parameters with which to subject the floating platform to. The combined wind-wave resource was characterized using wave data from the Pacific Northwest (PNW) National Data Buoy Center (NDBC) Buoy 46041. The West Coast is of particular interest with regards to floating offshore wind development as the sea shelf drops rapidly creating water depths in excess of 60 m. As indicated from figure 1.1, nearly 59% of the available wind resource is located in water depths greater than 60 m. This implies any offshore wind deployment to this region is very likely to require floating wind turbines to remain cost competitive. The NDBC Buoy 46041 is located in Cape Elizabeth, approximately 45 nautical miles Northwest of Aberdeen, WA. The buoy has gathered wind, anemometer located at 5 m, and wave data since 1987 providing a thorough resource assessment. Water depth at this location is approximately 114 m which provides deep water waves for a range of wave lengths up to 230 m. The wave channel facility utilizes a water depth of 1.37 m providing a similar scaled water depth and range of deep water waves. Hub height wind velocity is extrapolated from the 5 m anemometer to a height of 119.5 m using the International Electromechanical Commission (IEC) standard outlined in part 1 of the wind turbine design requirement document [23]. The extrapolation from wind speed at 5 m to hub is performed by using a power law equation for the normal wind profile (NWP) model. The NWP is given by the following equation:

$$V(z) = V_{hub}(z/z_{hub})^{\alpha}, \tag{3.9}$$

where $V(z)$ is the wind speed at height z, V_{hub} is the wind speed at hub height, z_{hub} is the hub height, and α is the wind shear power law exponent with a value of 0.2. Equation 3.9 is solved for V_{hub} using the average velocity data at 5 m. Figure 3.4 is the

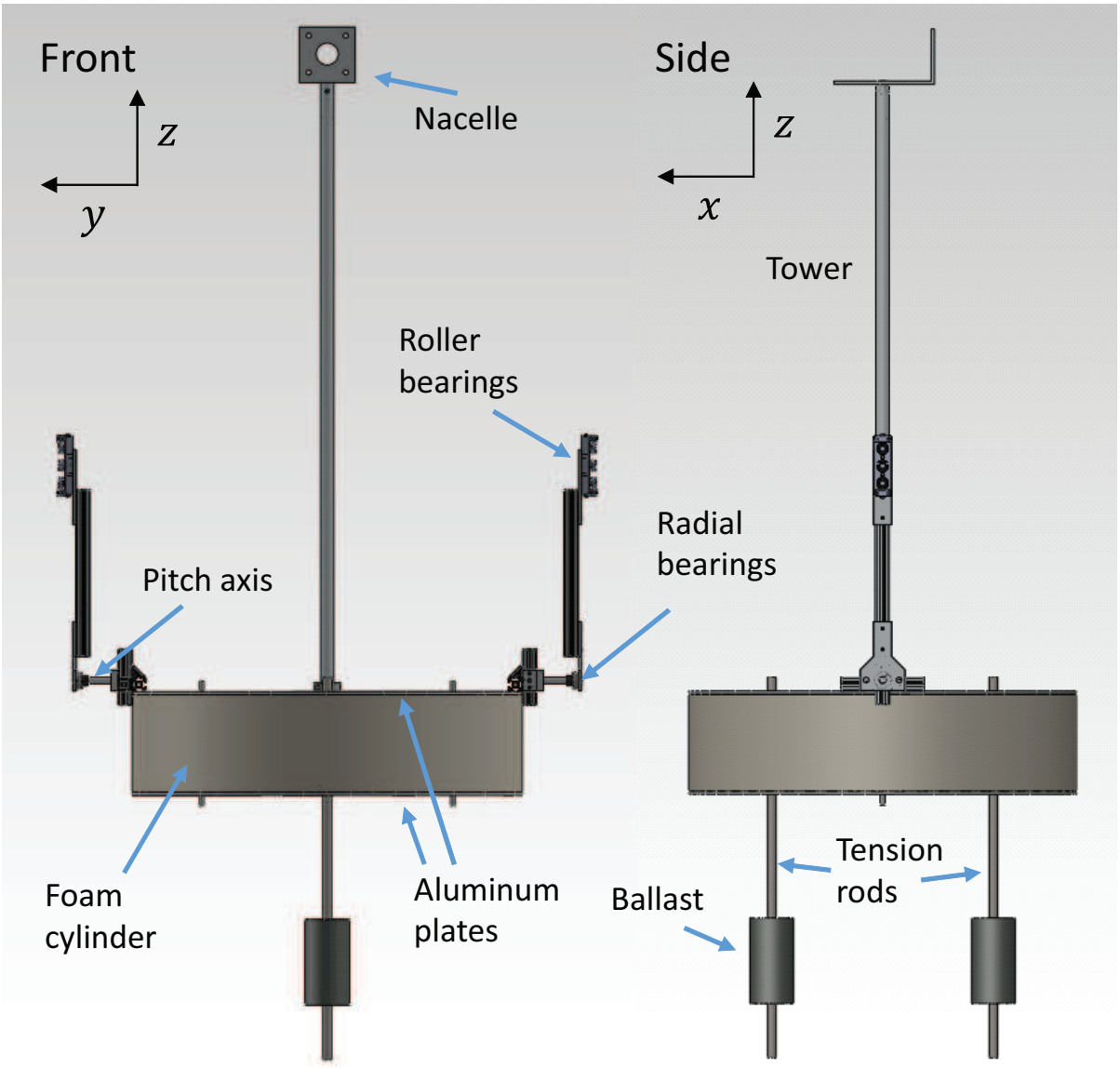

Figure 3.3: Platform drawing, redo drawing, add 3D model showing fixture system

resulting extrapolated averaged wind speed by month for NDBC Buoy 46041 from 1987 to 2010. The average wind speed for this time frame is 8.21 m s^{-1}.

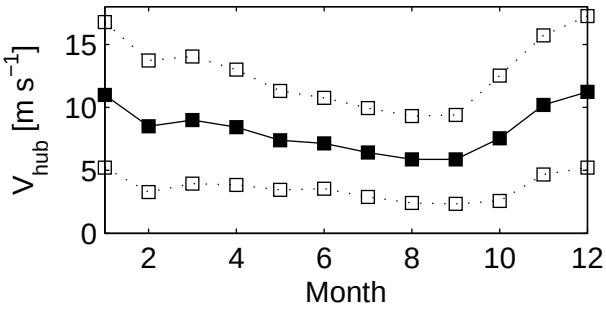

Figure 3.4: Extrapolated wind speed at z_{hub}, prototype scale. Solid square is the average wind speed, open square represents ±1 standard deviation

Figure 3.5 shows the monthly average wave period and significant wave height for the same period as the wind speed as recorded by the NDBC Buoy 46041. The average wave period for this period is 10.96 s and the average significant wave height is 2.18 m. Significant wave height, H_s is defined by the mean wave height, trough to crest, of the highest third of the waves.

Froude similarity is used to scale the wave environment to be used in the experimental modeling. Figure 3.6 shows the scaled monthly averaged wave period and significant wave height. The average wave period is 1.10 s and average wave height is 2.18 cm.

The annual joint probability distribution (JPD) of wave characteristics at the prototype scale is given in table 3.2 showing the most commonly occurring waves at the buoy site. Consistent with the mean, the most common wave is in the range of $T_w = [10.0 - 12.9]$ s and $H = [1.5 - 2.4]$ m with an occurrence rate of 18.2%. The model scale wave environment is given in table 3.3. Froude scaling using 1/100 scale ratio is used. The most common wave, at the model scale, has $T_w = [1.0 - 1.29]$ s and $H = [1.5 - 2.4]$ cm. These model scale wave characteristics will be used to drive the experiments.

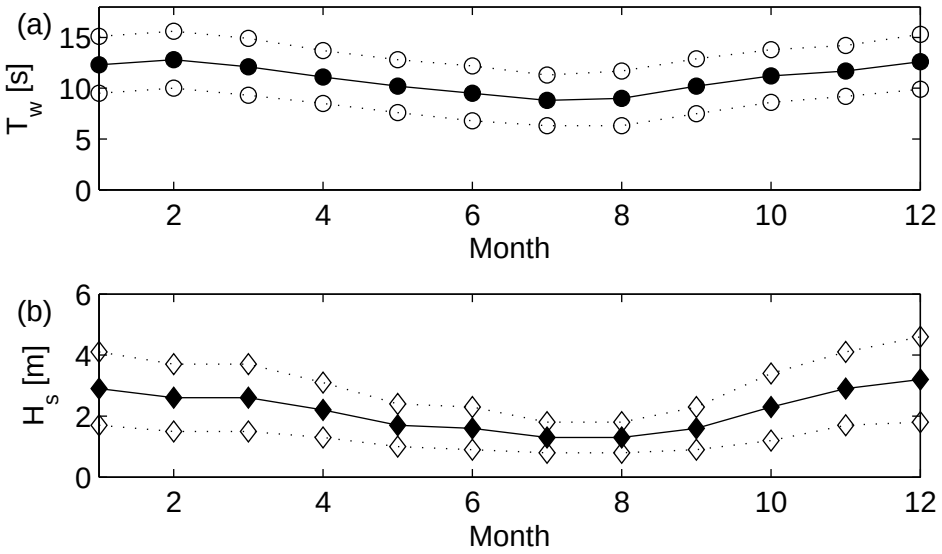

Figure 3.5: Average prototype wave environment by month with average shown in solid symbol and ± 1 standard deviation with open symbol (a) wave period T_w and (b) significant wave height H_s

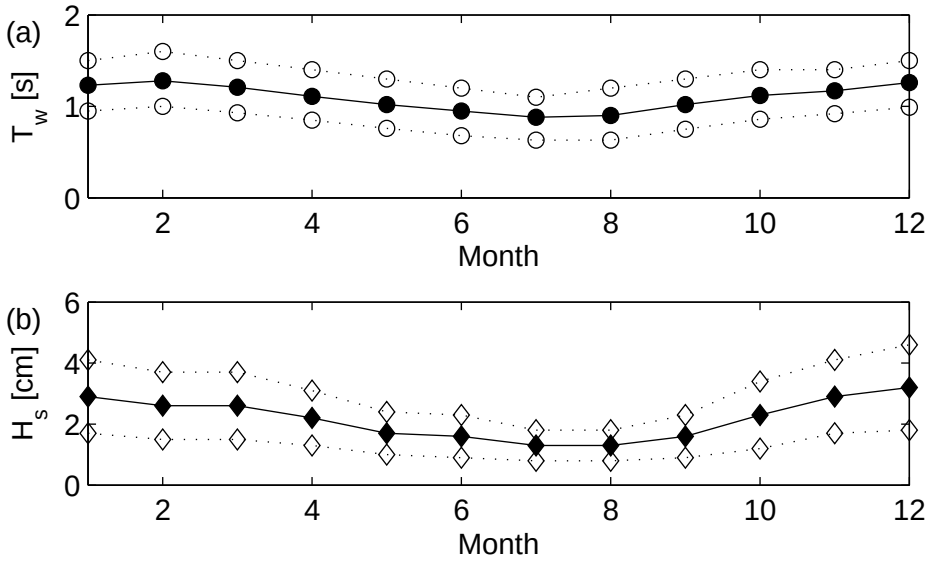

Figure 3.6: Average wave environment, model scale, by month with average shown as solid symbols and ± 1 standard deviation with open symbols (a) wave period T_w and (b) significant wave height H_s

Table 3.2: Prototype JPD of wave properties

	H [m]													
T_s [s]	0-0.4	0.5-1.4	1.5-2.4	2.5-3.4	3.5-4.4	4.5-5.4	5.5-6.4	6.5-7.4	7.5-8.4	8.5-9.4	9.5-10.4	>10.5	TOT %	TOT N
<3.0	*	*	-	-	-	-	-	-	-	-	-	-	0	3
3.0-3.9	-	0.1	-	-	-	-	-	-	-	-	-	-	0.1	212
4.0-4.9	-	0.5	0.1	-	-	-	-	-	-	-	-	-	0.6	836
5.0-5.9	*	1.5	0.6	0.1	*	-	-	-	-	-	-	-	2.1	2989
6.0-7.9	*	8.6	4.5	0.9	0.2	*	-	-	-	-	-	-	14.2	20420
8.0-9.9	*	8.1	8.5	2.3	0.7	0.2	*	*	-	-	-	-	19.9	28683
10.0-12.9	*	8.1	18.2	10.6	4.4	1.5	0.5	0.1	*	*	-	-	43.5	62624
13.0-15.9	*	2.6	3.2	3.0	2.0	1.0	0.4	0.1	*	*	*	*	12.4	17890
16.0-20.0	*	1.4	1.1	0.7	0.4	0.2	0.1	*	*	*	*	*	6.0	8703
≥20.0	-	0.3	0.4	0.3	0.1	*	*	*	*	*	-	-	1.2	1697
TOT %	0.0	31.8	36.9	18.3	8.1	3.1	1.1	0.3	0.0	0.0	0.0	0.0	100	
TOT N	71	45910	53167	26448	11762	4439	1590	472	153	40	15	8		144072

Table 3.3: Model scale JPD of wave properties

T_s [s] \ H [cm]	0-0.4	0.5-1.4	1.5-2.4	2.5-3.4	3.5-4.4	4.5-5.4	5.5-6.4	6.5-7.4	7.5-8.4	8.5-9.4	9.5-10.4	>10.5	TOT %	TOT N
<0.3	*	*	-	-	-	-	-	-	-	-	-	-	0	3
0.3-0.39	-	0.1	-	-	-	-	-	-	-	-	-	-	0.1	212
0.4-0.49	-	0.5	0.1	-	-	-	-	-	-	-	-	-	0.6	836
0.5-0.59	*	1.5	0.6	0.1	*	-	-	-	-	-	-	-	2.1	2989
0.6-0.79	*	8.6	4.5	0.9	0.2	*	-	-	-	-	-	-	14.2	20420
0.8-0.99	*	8.1	8.5	2.3	0.7	0.2	*	*	-	-	-	-	19.9	28683
1.0-1.29	*	8.1	18.2	10.6	4.4	1.5	0.5	0.1	*	*	-	-	43.5	62624
1.3-1.59	*	2.6	3.2	3.0	2.0	1.0	0.4	0.1	*	*	*	*	12.4	17890
1.6-2.0	*	1.4	1.1	0.7	0.4	0.2	0.1	*	*	*	*	*	6.0	8703
≥2.0	-	0.3	0.4	0.3	0.1	*	*	*	*	*	-	-	1.2	1697
TOT %	0.0	31.8	36.9	18.3	8.1	3.1	1.1	0.3	0.0	0.0	0.0	0.0	100	
TOT N	71	45910	53167	26448	11762	4439	1590	472	153	40	15	8		144072

3.4 Data acquisition system and control

Data acquisition and control is performed by a National Instruments cRIO-9024. The cRIO-9024 is a stand-alone measurement and control device running LabVIEW Real-Time allowing deterministic motor control and data logging. The system was designed to perform wave channel experiments, where motor control and analog measurements would be required at 100 Hz, and wind tunnel experiments, where the system would need to control two linear actuators, integrate with a PIV capture system, and record hotwire measurements and precise motor positions at 10,000 Hz. The following will be a description of the system as it pertains to wave channel experiments. A different configuration of the same system is used in the wind tunnel.

The cRIO is integrated with an 8-slot reconfigurable chassis, NI 9112, where an analog I/O module is added. The analog module, NI 9205, has 16 bit precision, capture rates up to 250 kS-s^{-1}, 32 input channels, and programmable measurement range.

A 7.26 Nm brushless DC servo motor, AKM32H, is used to control rotor speed. Rotor speed is used to vary the overturning moment caused by the thrust produced. Section §5.3 covers the calibration of the thrust-rotor speed curve. The servo motor is controlled by the cRIO which sends control commands via EtherCAT to a motor drive (6 Amp AKD motor drive). Motor position is captured via a Smart Feedback Device (SFD) at the motor shaft and sent back to the cRIO. Motor speed capture and control is performed at 100 Hz.

Wave height, H, is directly measured by 4 Massa ultrasonic M-300/150 sensors at a point. The sensors are programmed to measure water elevation in a vertical window of $\pm$12 cm with a resolution and accuracy of 0.25 mm in this configuration. Two sensors are located near the platform at $\pm$1D where D is the platform diameter, 56 cm. The incident waves are measured at -8D with two M-300/150 sensors, one sensor being -80 cm from the sensor located at -8D. These two sensors are used to determine wave period (T_w), celerity (c), and length (L), through wave peak tracking. Wave height is measured from MSL at 20 Hz.

The offshore floating platform position is measured using two Keyence laser displacement sensors located on the x-axis at $\pm$220 mm from the origin. Restricting the motion to heave and pitch and assuming rigid body motion allows the two displacement

sensors to fully define the turbine position. As shown in figure 3.2 the two sensors are termed L1 and L2. L1 is a Keyence LK-501 sensor with analog output of ±10 V and measurement window of ±250 mm. The L1 sensor has measurement repeatability of 50 μm. The L2 sensor is a Keyence LK-G502 with programmable output voltage and measurement range set to that of the L1 sensor. The L2 sensor has a repeatability of 2 μm. Platform postion is captured at 100 Hz.

A subset of experiments were performed to investigate the effect of a mean and fluctuating rotor thrust on platform dynamics, exploring strategies to minimize pitch with thrust (rotor speed) being a function of platform pitch. Limited reduction of pitch was observed with the implemented closed-loop control strategy, results are discussed in §5.4. Section 4.4 covers the control strategy in more detail. Current platform pitch is used as a control variable in determination of rotor speed. A differential control strategy is implemented to determine the magnitude of rotor speed to be applied to minimize current pitch state. As the platform pitch accelerates, rotor speed (or thrust) is increased to counteract this acceleration.

Current theoretical platform pitch dampening control strategies are discussed in [24]. The strategies discussed in this paper utilize tower-top acceleration, similar to using platform pitch acceleration, to control current blade pitch with the goal of minimizing pitch oscillation amplitudes, however, very limited success was observed in the simulations. A consequence of the active pitch mitigation control is a significant impact on generator speed and therefore power generation and main shaft loading. The author concluded unconventional control strategies would need to be investigated in order to minimize platform pitch while maintaining desirable generator speed and main shaft loading.

Chapter 4

Test procedure: wave channel

Model tests started with a partial investigation of the $\Omega - S$ parameter space with the floating structure not present. Values of Ω and S were varied to achieve the desired environmental conditions as discussed in §3.3. This test also served to verify wave period and height were consistent in the x and y directions, specifically in the region where the floating wind turbine would be installed. Figure 4.1 is an image of the wave channel with the sensors used to verify wave statistics along the y-axis with the hinged-paddle shown in the background. A total of 8 water elevation sensors are used to quantify the wave height and period. Shown in the figure, however, not used in platform response tests, are 4 Ocean Sensor Systems Wave Staff: OSSI-010-002E. The Wave Staff is a fast capacitive type water level sensor with ± 2.5 mm accuracy. In addition to the Wave Staffs, 4 Massa ultrasonic M-300/150 sensors were used. Details on the Massa sensors were covered in §3.4. Statistics of the incident waves are discussed in 5.2.

4.1 Free decay procedure

Free decay tests were performed on the floating wind turbine to measure the response to initial displacements in pitch and heave and determine the system natural periods and damping in these modes, results are given in §5.1. Heave decay tests were performed by raising the platform to specific z positions and holding the turbine system in place. Once the turbine system reached steady-state, as the system would vibrate during the process of attaching the turbine to the release system, a mechanical release switch would

Figure 4.1: Measurement setup for wave generator calibration and wave statistics prior to platform installation

be triggered and the floating wind turbine model would drop and be free to oscillate in heave. The mechanical release is shown in figure 4.2. Pitch decay tests were performed by using a rod to push and hold the platform into an initial pitch and then released once steady-state is achieved. After the rod is released the platform was free to oscillate in pitch.

In the pitch free decay tests, only the pitch is initially displaced. Likewise, for heave tests, only the heave is initially perturbed from equilibrium. A minimum of three different initial displacements are used in pitch and heave to test the turbine-platform system response to different perturbations. Additionally, this set of tests was performed on three different turbine configurations, table 4.1 summarizes the free decay tests. The first set considered the wind turbine without wind and without motor cables attached. This setup would be used to validate the computational model and simulate motion in the wind tunnel experiments. The motor cables were then attached and tests were performed using this configuration, again without wind. The third and last set of free decay tests employed a spinning rotor, meaning motor cables are attached. Decay tests in pitch only were performed at mean rotor speeds of 8, 12, and 16 rps to investigate

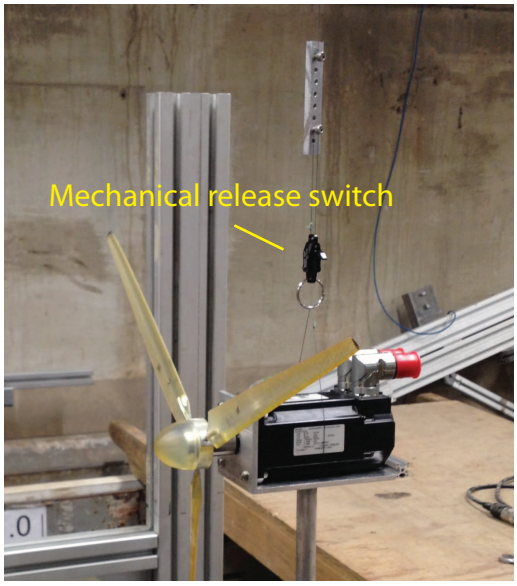

Figure 4.2: Heave free decay mechanical release

Table 4.1: Free decay test summary

Turbine Configuration	Test Type
Baseline; no wind, no motor cables	heave and pitch free decay
No wind, motor cables attached	heave and pitch free decay
Wind; 8, 12, 16 rps	pitch free decay

if variations in rotor speed (thrust) had an effect on pitch damping. Rotor speeds correspond to 0.44, 1.09, and 2.10 N of thrust respectively.

4.2 RAO procedure

Once the free decay tests were completed, with damped natural frequencies for the pitch and heave modes known, a campaign to characterize the linear response of the floating wind turbine system subjected to linear waves was performed. The linear response of the floating turbine is used to calculate a response amplitude operator (RAO). RAOs are used to determine the positional behavior of the floating wind turbine while operating

in a given sea state. RAO in pitch is defined as the pitch height, maxima to minima, normalized by the wave height [deg m^{-1}]. The heave RAO is defined as heave height normalized by wave height [m m^{-1}]. The RAOs were generated using wave periods ranging from 0.91 to 3.00 s and wave heights from 0.93 to 3.5 cm.

As discussed in §3.1 measurements are performed in a clean-wave window, which is a function of wave period, where the window is determined by using incident wave height measurements at -8D. The window is defined by consistent wave height and period as well as quasi-consistent heave and/or pitch response. A quasi-consistent response is used as wave periods near the damped natural frequency may produce an unsteady response. i.e. pitch amplitude may oscillate at additional frequencies within a clean-wave window. Figure 4.3 gives an example of a clean-wave window. The top graph shows time resolved measurements from two sensors of the incident wave at -8D. The measurement window includes a transitional period, (a), where the paddle frequency ramps up, creating waves of varying height and period. After the transitional period is the clean-wave window, denoted by (b). Wave statistics are determined here. The clean-wave window is characterized by consistent wave height between the two sensors as well as wave period. The two water height sensors located at -8D are separated by -80 cm (1.28D) with MS2 being at -8D and MS3 at -9.28D. The figure depicts waves generated with $T_w = 1.01$ s and $H = 2.60 \pm 0.12$ cm as measured from MS2 and $H = 2.54 \pm 0.09$ cm using MS3 measurements. RAOs in pitch and heave are determined by using an average wave height from MS2 and MS3 within the clean-wave window and the maximum measured pitch or heave within that same window. The period where reflected waves are present is depicted in (c).

RAOs for pitch and heave were determined for two wind turbine configurations, one being the baseline case with no wind or motor cables present. Figure 4.4 shows the baseline turbine configuration subjected to linear waves. In the second configuration motor cables were attached and the rotor spun at 12 rps. Spinning the rotor at 12 rps corresponds to 1.09 N of thrust and an overturning moment of 1.08 N-m. This rotor speed was chosen as the resulting thrust had relatively low variance, as seen in figure 5.6 and provided a low enough rps value where the speed could be varied as the wave frequency. Larger values of thrust would have safety concerns when controlling the speed at periods of 2-3 s. 1.08 N-m at model scale corresponds to 901.26 kN of thrust

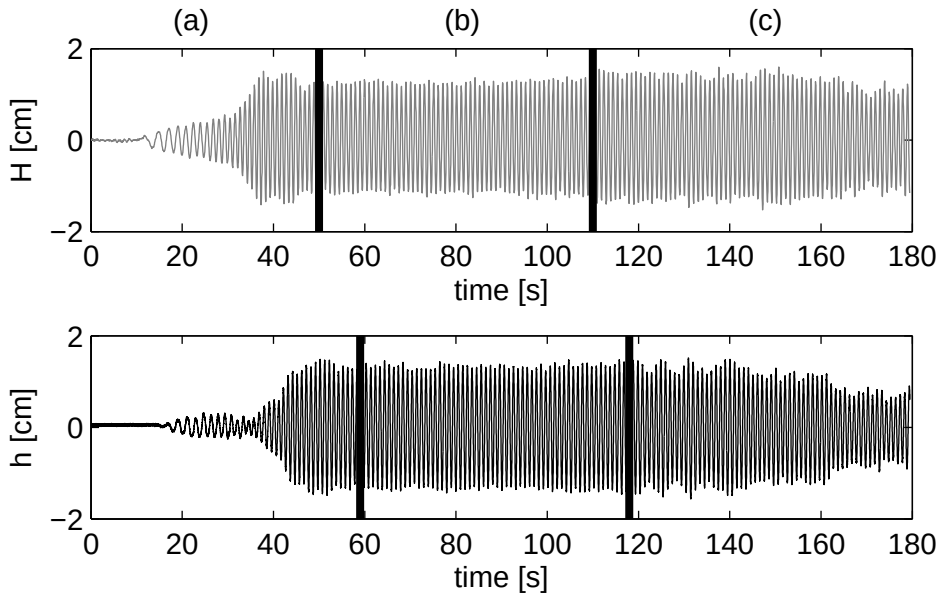

Figure 4.3: Depiction of the clean wave window with (a) transitional wave period, (b) clean wave window and corresponding quasi-steady-state response in heave, h, and (c) reflective waves present. Top figure shows the wave height H as measured at -8D, bottom figure gives heave, h

at prototype scale and is achieved at approximately 6 m/s wind speed.

Figure 4.4: Baseline turbine configuration under linear wave excitation

4.3 Variable thrust procedure

Simulated rotor thrust is calibrated using an Advanced Mechanical Technology Inc. (AMTI) multi-axis force transducer, MC3A-100-6691. The horizontal thrust component, F_x, in the x-direction is recorded for rotor speeds ranging from 2 to 20 rps. The measurement setup is shown in figure 4.5 where the model tower, nacelle, DC servo motor, and rotor are attached to the force-balance sensor.

Figure 5.6 (a), with specific results discussed in §5.3, gives the corresponding thrust as a function of rotor speed. As first introduced in §3.4 a subset of experiments were performed to investigate the effect of a fluctuating aerodynamic thrust on system dynamics as well as a control strategy to minimize pitch amplitude. A first set of experiments looked at fluctuating rotor speed around a mean of 12 rps. The rotor speed was varied sinusoidally with periods of 5 and 10 seconds and amplitude of ± 10 and ± 20 percent from the mean. This corresponds to a thrust range of [0.86 - 1.36] N and [0.66 to 1.65] N

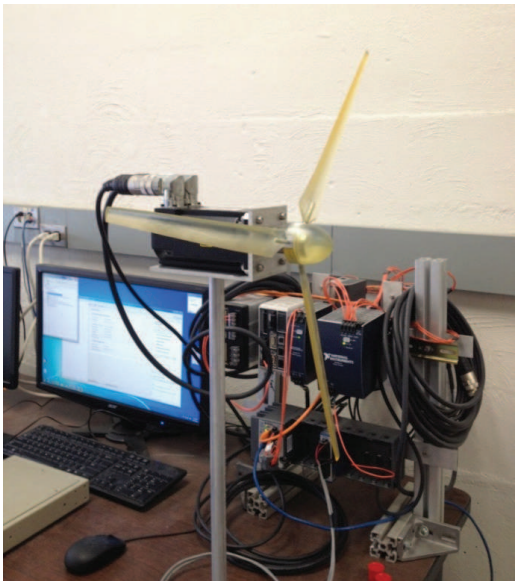

Figure 4.5: Rotor thrust calibration

respectively, with the mean being 1.09 N. The oscillation period of the rotor was chosen to represent the wake meandering frequency of an upwind turbine. [25] suggests there is a constant Strouhal number of 0.23, independent of operating conditions, associated with instabilities in the far wake of a wind turbine rotor. The Strouhal number (St) is a dimensionless number which describes an oscillation in a fluid flow. The Strouhal number is defined as

$$St = \frac{fD}{V_\infty}, \tag{4.1}$$

where f is the wake fluctuation frequency, D is the characteristic length (rotor diameter in this case), and V_∞ is the free stream velocity. The frequency at the prototype scale is determined by solving equation 4.1 for f and using $D = 200$ m, $V_\infty = 8.7$ m s^{-1} which is the approximate average wind speed during the year at elevation of $z = 119.5$ m from the PNW environmental data, and $St = 0.23$. This gives $f = 0.01$ Hz which corresponds to 100 s oscillation period. At the model scale, the meandering frequency is found by applying Froude similarity, and has a value of 10 s. Using this result, the model rotor fluctuations were set to 5 and 10 s.

Wave periods for the variable thrust tests were chosen to look at a broad spectrum of platform responses. Table 4.2 gives a summary of the wave periods and rotor speed

Table 4.2: Summary of variable thrust test cases

Wave Period [s]	Variable Rotor Speed
2.52	±20 percent at 10 s
2.21	±10, 20 percent at 5 and 10 s
1.51	±20 at 10 s
0.99	±10, 20 percent at 10 s
0.82	±10, 20 percent at 5 s

fluctuations used in these tests with results discussed in §5.3.

4.4 Pitch mitigation

A control strategy intended to minimize platform pitch by manipulating rotor thrust was implemented and tested for large waves near the peak pitch response period, $T_w = 2.2$ s and $H = 7.65$ cm. Large waves are used in order to obtain large pitch amplitudes due to the wave forcing. The pitch mitigation uses an open-loop control method to set rotor speed as a funciton of the time rate of change of the platform pitch measurement. This is a derivative type controller. During large platform pitch accelerations the rotor speed is adjusted to dampen the oscillation amplitude. Conceptually, as the platform begins to pitch back (positive pitch), rotor thrust is decreased. Forward pitching (negative pitch) of the platform results in an increasing of rotor thrust. The following equation describes the derivative control law:

$$\Omega_r(t) = -K_d \frac{d}{dt}\phi(t) + \Omega_{r,0} \tag{4.2}$$

where Ω_r is the rotor speed, $\Omega_{r,0}$ is the rotor speed set point, K_d is the derivative control gain, and ϕ is platform pitch. In the control space equation 4.2 is represented as

$$\Omega_r = -K_d(\phi_i - \phi_{i-1}) + 12 \tag{4.3}$$

where $i = 1, 2, 3, ...n$ and n is the number of pitch measurements, n is based on the current pitch update rate of the control strategy.

All tests were performed on the same wave generator settings resulting in waves having $T_w = 2.2$ s and $H \approx 7.6$ cm. The platform response is measured through

Table 4.3: Summary of platform pitch control test cases

$T_w = 2.2$ [s]	$H \approx 7.6$ [cm]
K_d	f_ϕ [Hz]
12	20
15	20
22	20
15	10
18	10
20	10
22	10

a time window which includes reflected waves in order to increase the total number of oscillations on which to perform statistics. Here, it is assumed environmental conditions are statistically similar and therefore any differences measured in platform pitch will be a result of the pitch control method being applied. Two variables in the control strategy are varied, K_d and the pitch update rate, f_ϕ. Table 4.3 summarizes the variables used in the experiments. Values of K_d were chosen to limit the variation in rotor speed to what was considered reasonable values. Due to hardware limitations, f_ϕ had a maximum value of 20 Hz with 10 Hz being a second update rate used. Details are presented in §5.4

Chapter 5

Results: wave channel

5.1 Free decay tests

Free decay tests were performed in pitch and heave to characterize the system natural periods and damping in these modes. For the free decay tests of each mode, the system is treated as having a single degree of freedom. Viscous and frictional damping are small resulting in an underdamped system with oscillitory motion. For an underdamped system, the resulting displacement x due to an initial displacement X is described by the following equation [21]:

$$x = X \exp(-\zeta \omega_n t) \sin[\sqrt{1-\zeta^2}\omega_n t], \tag{5.1}$$

where ω_n is the system natural frequency and ζ is the damping ratio, or damping factor. The solution for the underdamped system is an exponential decay function with an oscillating term. The oscillations have a frequency of $\sqrt{1-\zeta^2}\omega_n$ which is defined as the damped natural frequency, ω_d. The damping ratio is found by determining the logarithmic decrement, δ, which uses a ratio of two successive peaks from the time-domain response of the system. As applied to the initial displacement, X, and the immediate successive peak, δ can be defined by

$$\delta = \ln\left(\frac{x_0}{x_1}\right), \tag{5.2}$$

where x_0 is the initial displacement and is equal to X, x_1 is the first damped oscillation amplitude after one period. The period T is defined as the time from peak to peak

and is used to determine ω_d by $\omega_d = 2\pi/T$. The damping ratio ζ is found from the logarithmic decrement by

$$\zeta = \frac{1}{\sqrt{1 + \left(\frac{2\pi}{\delta}\right)^2}}. \tag{5.3}$$

With ζ and ω_d known, the system natural frequency is determined by

$$\omega_n = \frac{\omega_d}{\sqrt{1 - \zeta^2}}. \tag{5.4}$$

Figure 5.1 shows the measured platform pitch response to two different initial angles of 0.5 and 6 degrees. The decaying oscillations with time can be observed. Similarly, figure 5.2 shows the heave response to two initial displacements, 10 and 20 mm. As compared to the heave decay response, the pitching motion has a relatively low damping factor resulting in many oscillations before coming to rest. For comparison, the damping factor is 8 times larger for heave than pitch.

Results for averaged ω_d and ζ over multiple tests of both pitch and heave decay responses are presented in table 5.1. The damped natural frequency in pitch is 0.41 Hz with standard deviation of 0.008 Hz (2% of the mean) for the baseline test with $\zeta = 0.02$, rms of 0.007 (30% of the mean). The addition of cables increases the pitch damping to $\zeta = 0.06, 0.04$, and 0.05 and results in a slower oscillation with $\omega_d = 0.38$ Hz. The latter average frequency is consistent for all tests where motor cables were attached. The perceived change in pitch damping ratio with different simulated wind cases is a function of the average calculation. As seen in figure 5.4 (a) and discussed below, ζ is consistent over the range of rotor speeds tested. From this it can be concluded the addition of steady, simulated wind does not change the turbine system frequency response.

Figures 5.3 (a) and 5.4 (a) give the damping ratio as a function of initial platform pitch and heave displacement, respectively. Damping ratio tests in pitch where cables were both present and not present, as well as with simulated wind, show some dependency on initial pitch angle. Small initial pitch angles correspond with a larger damping ratio. Above initial angles of 2 degrees, ζ flattens and remains relatively consistent for tests with motor cables present. After flattening out, ζ begins to increase with increasing initial pitch angles for the baseline case. It is also shown that the damping ratio is consistent across simulated wind speeds. Although ζ in pitch has a relatively large

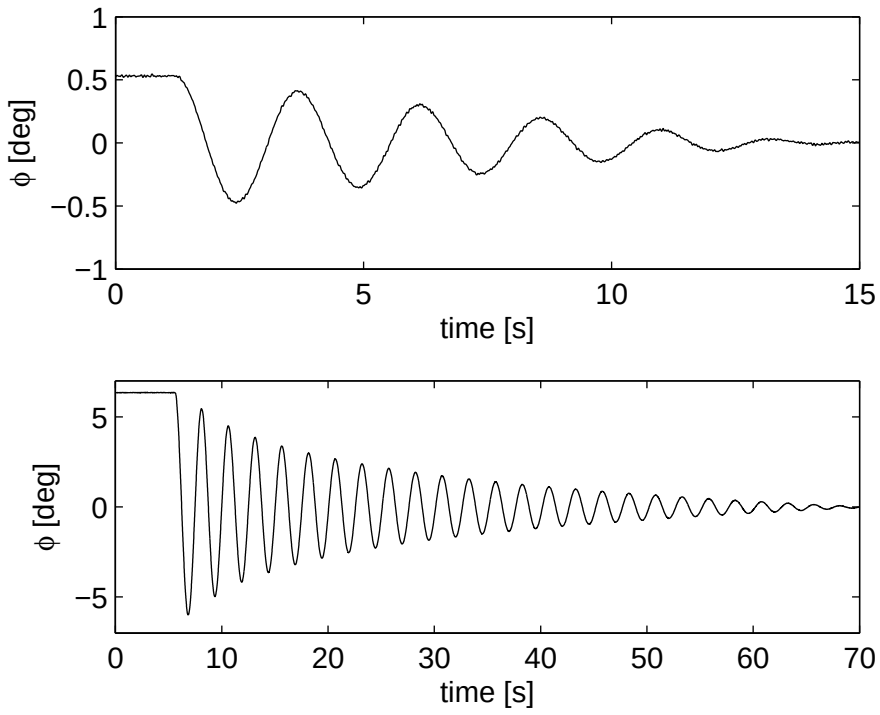

Figure 5.1: Pitch response in time due to an initial pitch of 0.5 (top) and 6 (bottom) degrees

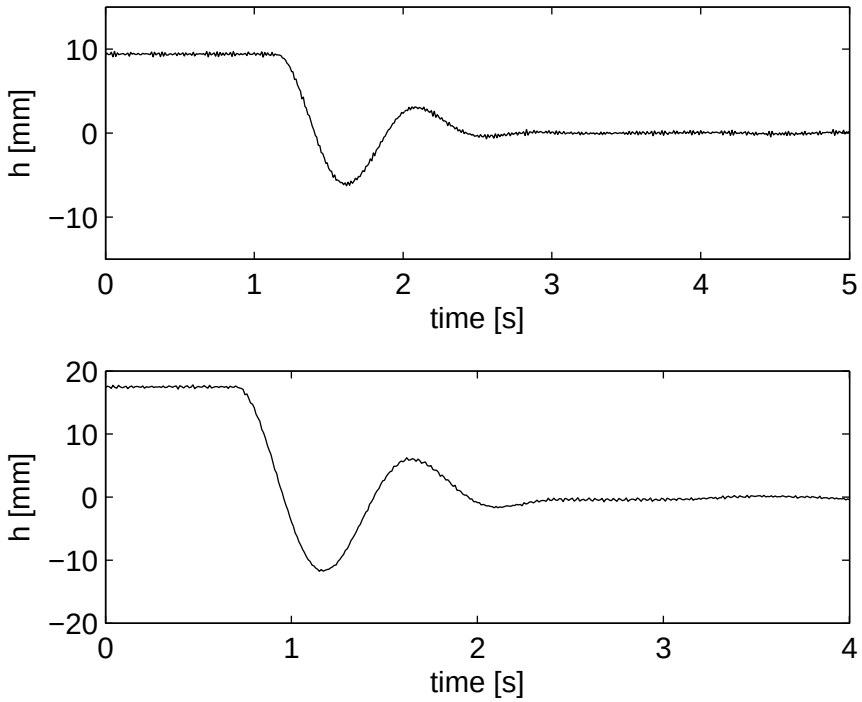

Figure 5.2: Heave response in time due to an initial displacement of 10 (top) and 20 (bottom) mm

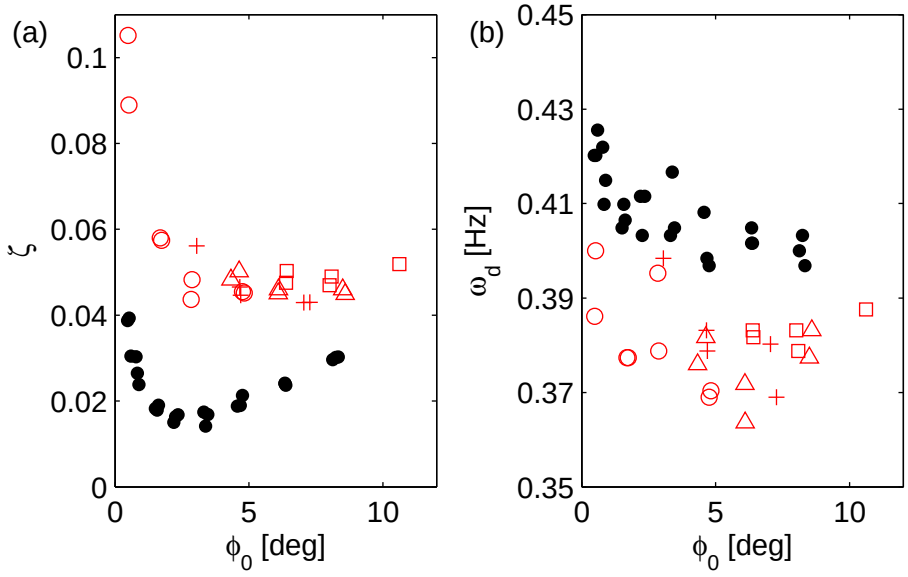

Figure 5.3: (a) damping ratio ζ for varying initial pitch displacements ϕ_0 and (b) damped natural frequency for varying initial pitch displacements ϕ_0. Black dot: baseline case, red circle: cables, red plus: cables and wind 8 rps, red triangle: cables and wind 12 rps, red square: cables and wind 16 rps

Table 5.1: Free decay response, damped natural frequencies and damping ratios

Turbine Configuration	Pitch ω_d [Hz]	Heave ω_d [Hz]	Pitch ζ	Heave ζ
baseline	0.41 (2.45 s)	1.09 (0.92 s)	0.02	0.16
cables	0.38 (2.62 s)	1.06 (0.94 s)	0.06	0.15
cables + wind 8 rps	0.38 (2.62 s)	-	0.04	-
cables + wind 12 rps	0.38 (2.66 s)	-	0.05	-
cables + wind 16 rps	0.38 (2.61 s)	-	0.05	-

Table 5.2: Free decay response, natural frequencies

Turbine Configuration	Pitch ω_n [Hz]	Heave ω_n [Hz]
baseline	0.41 (2.45 s)	1.10 (0.91 s)
cables	0.38 (2.61 s)	1.07 (0.93 s)
cables + wind 8 rps	0.38 (2.62 s)	-
cables + wind 12 rps	0.38 (2.66 s)	-
cables + wind 16 rps	0.38 (2.61 s)	-

variance, the effect on ω_d is very small.

As with the pitch response, there is a dependency on initial heave displacement for damping values. Both the baseline case and turbine with cables show a trend of decreasing damping factor for increasing initial heave height. However, the relationship is more pronounced in the baseline turbine configuration. Additionally, there is not as significant a difference in the damping ratio between the two turbine configurations as compared with the pitch decay tests.

Damped natural frequency as a function of initial pitch angle is shown in figure 5.3 (b). Smaller initial angles are associated with higher oscillation frequencies with ω_d slightly decreasing with increasing ϕ_0. However, the standard deviation is relatively small, 2% of the mean. The same trend is observed with the heave decay tests as shown in figure 5.4 (b).

Interesting point: the increased damping ratio in pitch, as a result of the addition of motor cables, provides for a slower osciallating platform. Here, an increase in damping ratio decreases frequency. However, looking at damping ratio as a function of

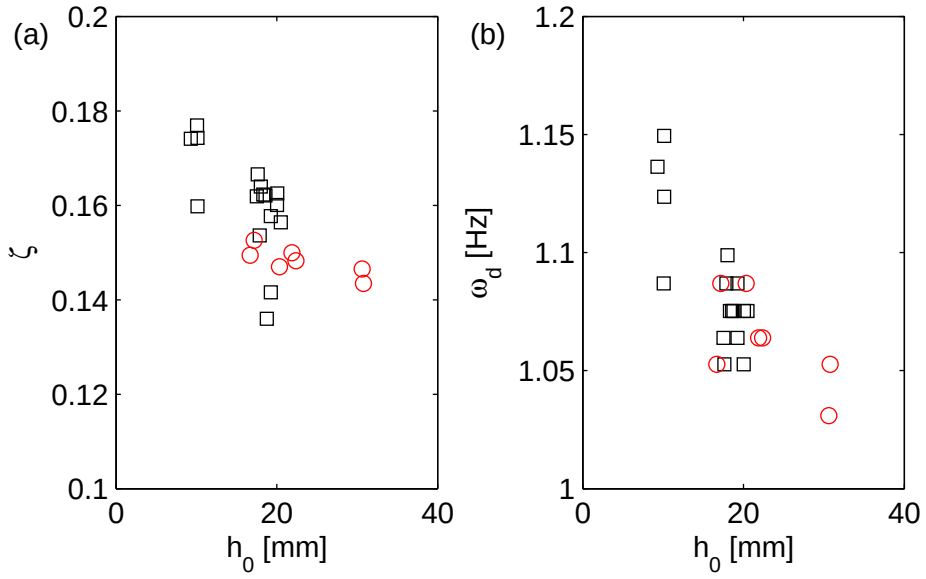

Figure 5.4: (a) damping ratio ζ for varying initial heave displacements and (b) damped natural frequency for varying initial heave displacements. Black square: baseline case, red cirlce: cables

initial pitch displacement, the larger values of damping factors correspond with higher frequencies. This is a direct relationship, opposite of what was first discussed.

5.2 Response amplitude operator

This section covers the dynamic response of the model platform in pitch and heave due to linear wave forcing with and without steady, simulated wind. Waves are varied from $T_w = [0.91 - 3.00]$ s with H between 0.96 and 3.41 cm. The dynamic response consists of the RAOs which are shown in figure 5.5. The results indicate a strong response in both pitch and heave near their respective resonant frequencies. Table 5.3 summarizes the findings for the baseline turbine.

Baseline turbine results in heave are shown as black circles in (a) of figure 5.5. The heave natural frequency is 1.10 Hz ($\omega_d = 1.09$ Hz) for the baseline turbine. The heave RAO has a peak response at $T_w = 1.01$ s, 0.99 Hz, with a value of 1.21 m m^{-1}. Heave response quickly drops for frequencies higher than the peak heave frequency. Slower

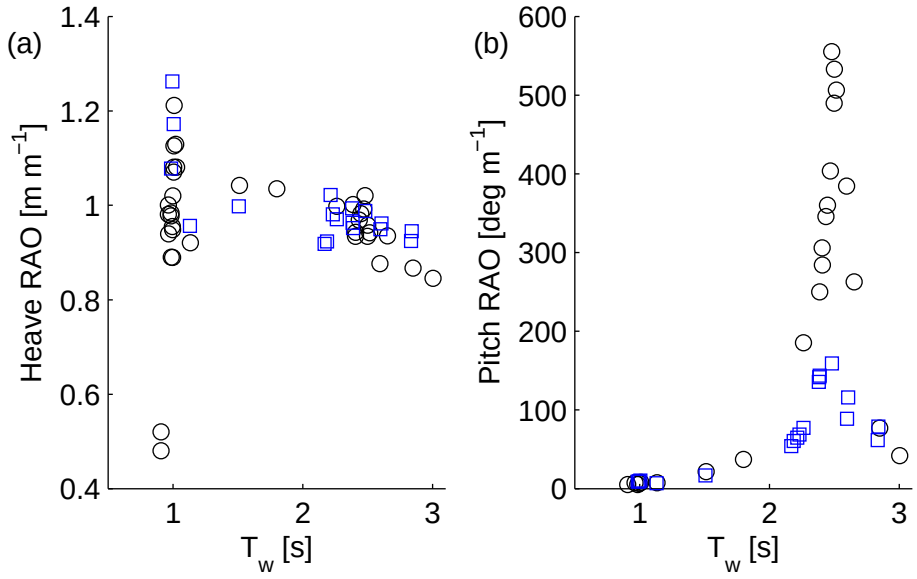

Figure 5.5: Response Amplitude Operator for (a) Heave and (b) Pitch
black circle: baseline turbine configuration, blue square: cables + constant wind $\Omega_r = 12$ rps ($F_{thrust} = 1.09$ N)

frequencies result in a near unity response in heave with a drop off beginning near the pitch peak at $T_w = 2.48$ s. It is important to note the heave natural frequency is near the typical wave periods as given by the PNW data with the most common waves between $T_w = 0.8$ s and $T_w = 1.59$ s. This is an unfavorable design characteristic, however, the heave motion is relatively small. At full scale, the most common waves would cause heaving amplitudes of 1-2 m.

The RAO in pitch for the baseline turbine is shown as black circles in (b) of figure 5.5. The pitch response exhibits a much larger excitation near its natural frequency as compared with the heave response. The period associated with the pitch natural frequency is 2.45 s. The RAO shows a peak response at 2.48 s with a value of 553.5 deg m^{-1}. This gives a response amplitude approximately 100 times larger than what is seen at the most common wave periods from the PNW data. Pitch response quickly diminishes at wave periods above and below the resonant period. Platform pitch response to typical waves, $T_w = [0.8 - 1.59]$s, is < 1 deg which is a very desirable response. Wave periods near the resonant frequency can induce large pitch amplitudes i.e. 4-5

deg from relatively small waves, 1-2 m in height at prototype scale. This identifies a need to carefully design floating wind turbine systems specifically tuned for the wave environment they will be deployed in.

Figure 5.5 also shows the RAOs for the case with steady, simulated wind corresponding to 1.09 N of thrust. Results for pitch and heave are shown as blue squares in (a) and (b) respectively. Heave peak response occurs at 1.00 s with a value of 1.26 m m^{-1}. Peak response in pitch occurs at $T_w = 2.48$ s with a value of 159.1 deg m^{-1}. As compared to the baseline wind turbine, the addition of wind and cables results in a similarly shaped ROA with pitch amplitude being significantly diminished. As was discussed in §5.1, this is not caused by the addition of wind, however, is a result of the motor cables.

5.3 Effect of rotor thrust

The calibrated rotor thrust, F_{thrust}, as a function of rotor speed is given in figure 5.6. Experimental results using the force sensor are shown as black dots with rms values as the error bars. Using a least-square log-fit, equation 5.5 is generated to produce a mean theoretical thrust as a function of rotor speed. Theoretical thrust values are shown as red circles.

$$F_{thrust,t} = 10^{-2.40}\Omega_r^{2.26} \tag{5.5}$$

In order to make the assumption that a fluctuating rotor generates a fluctuating thrust, a test using the force sensor with $\Omega_r = 12$ $\pm 10\%$ rps with a period of 10 s was performed. Results are shown in figure 5.7 with the measured force in gray and the predicted force based on rotor speed in red. Measured thrust and rotor speed are acquired at the same time-stamp. Equation 5.5 is applied to the measured rotor thrust in order to compare theoretical with empirical results. As shown in the figure, equation 5.5 predicts thrust well with rms of the error being 0.08 N. A cross-correlation was performed on the two time-varying signals to determine whether a delay exists between rotor speed and thrust. The cross-correlation of the signals gave a delay of zero samples. From this it was concluded a mean thrust could be determined from a fluctuating rotor speed.

As outlined in §4.3, similated thrust is varied at the Strouhal frequency of an upwind

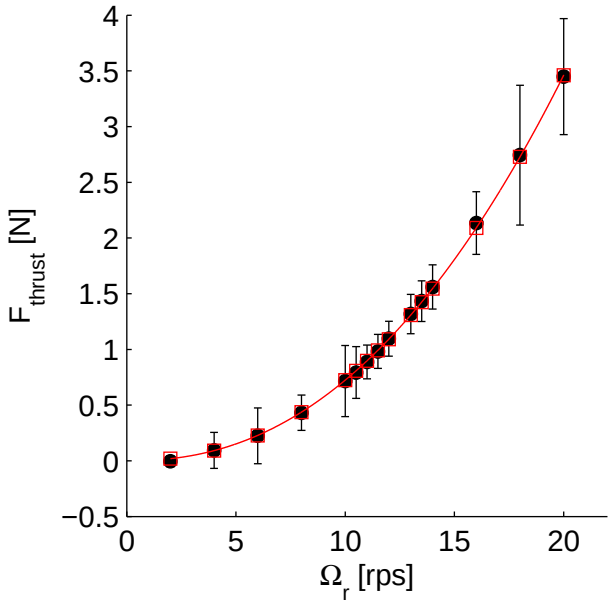

Figure 5.6: Model thrust curve vs rotor speed, experimental results shown as black dots with rms bars, theoretical thrust equation 5.5 as a function of Ω_r (red square)

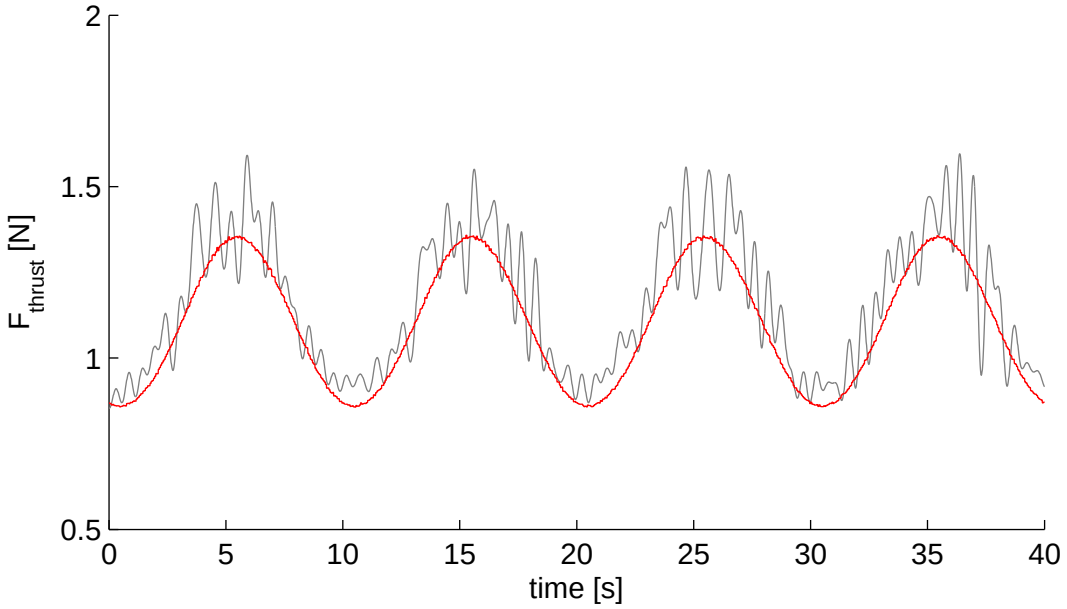

Figure 5.7: Recorded thrust variation, grey, compared with thrust as a function of rotor speed

turbine. At model scale the frequency, as found by equation 4.1, is 0.1 Hz or 10 s. Table 4.2 summarized the test cases used to look at platform pitch response to waves and varying wind. Here, two cases are highlighted with wind being varried around $\Omega_r = 12$ rps at $\pm 10\%$ and 5 s period. This rotor variation corresponds with wind fluctuations of approximately 2 m/s in amplitude with a period of 50 s at prototype scale. Half the Strouhal period is used in order to increase the number of oscillations in a clean wave window. The pitch energy spectra [deg^2] normalized by the pitch rms [deg^2] is used to study the effects of variable thrust. The two cases being compared have wave periods of $T_w = 2.21$ s and $T_w = 0.83$ s with similar wave heights. These wave periods are chosen as to represent the platform motion near the pitch natural frequency, $T_w = 2.21$ s, and far from $\omega_{n,pitch}$ in the range of common wave periods, $T_w = 0.83$ s.

Firgures 5.8 and 5.9 give the power spectral density (PSD) responses of the pitch normalized by the variance, S_ϕ/σ^2. At each wave period, a baseline case with static simulated wind, $\Omega_r = 12$ rps, $F_{thrust} = 1.09$ N, is given to contrast the effects of variable wind. Figure 5.9 gives results for $T_w = 0.83$ s. The baseline case is given with the solid black line. Pitch energy is concentrated at the wave frequency, 1.21 Hz, producing a dominant peak, with some energy represented at the natural frequency, 0.37 Hz. In contrast, the pitch spectra associated with fluctuating thrust (dot-dashed red), at the same wave period, gives a dominant peak at the rotor frequency. The energy at the wave and natural frequencies are largely washed out by the dominant frequency.

Figure 5.8 shows the PSD for $T_w = 2.21$ s. As with $T_w = 0.83$ s, the dominant frequency is present at the wave frequency, 0.45 Hz, for the baseline case (solid black line). The variable thrust case at this wave frequency, shown in the dashed blue line, maintains a clear peak at the wave frequency as well as a larger peak at the rotor frequency. With the addition of fluctuating wind, wave periods near the pitch damped natural frequency maintain a significant contribution to platform pitch oscillations from frequencies associated with the waves. Away from the pitch ω_d, thrust fluctuations will dominate the pitching motion.

The peaks associated with $T_w = 2.21$ s are broader and less defined as compared to the waves at $T_w = 0.83$ s. This is due to a relatively small number of oscillations within the clean wave time window, approximately 30 s for the former.

In general, the results of the pitch RAO can be used to predict the spectra pitch

response to wave and wind forcing of known frequencies. Wave frequencies far from the pitch natural frequency result in small pitch oscillations, or low energy. Variations in wind, and therefore thrust, will dominate the pitching motion at these frequencies. Near the pitch natural frequency, the pitch amplitude associated with the waves is of a similar magnitude as those produced by the thrust fluctuations.

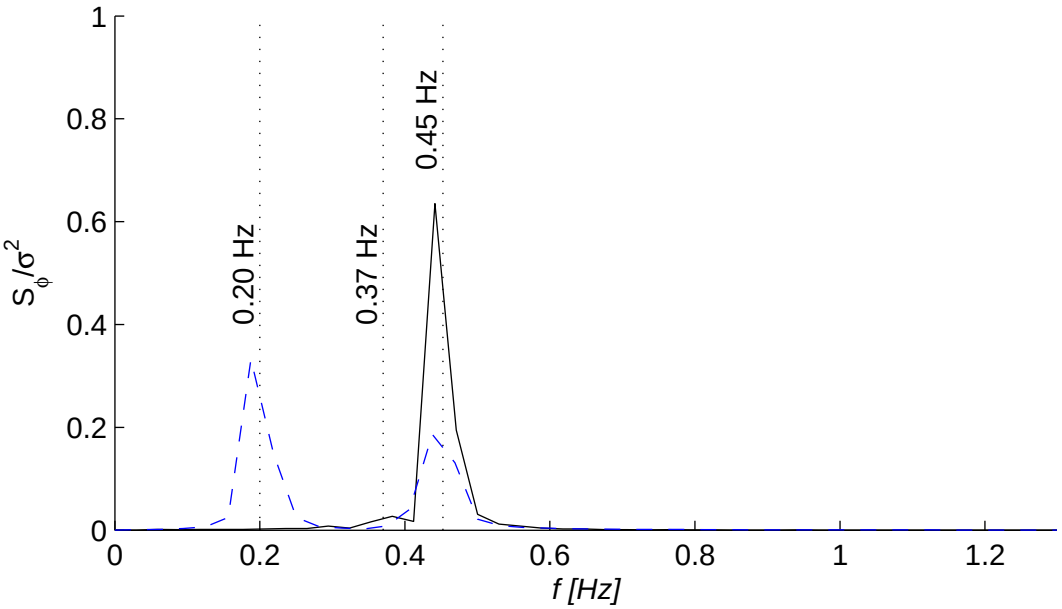

Figure 5.8: Power spectral density (PSD) for platform pitch at $T_w = 2.21$ s with static thrust (solid black) and variable thrust: $F_{thrust} = [0.86 - 1.36]$ N at 5 s (dashed blue)

5.4 pitch mitigation through open loop control

Results of the pitch control strategy are discussed in this section. As discussed in §4.4, equation 4.3 gives the derivative control strategy as implemented. K_d is varried from 12 to 22 with increasing values giving a larger thrust variation. Table 5.4 summarizes the values of K_d used as well as the approximate corresponding range of Ω_r and F_{thrust}. In addition to these two parameters, the pitch update rate, f_ϕ, is also varied. The pitch update rate is the time between successive pitch measurements used in the rotor speed control, equation 4.3. Figure 5.10 illustrates the effect of f_ϕ on Ω_r (a) and F_{thrust} (c). A lower pitch update frequency results in larger psuedo-accelerations and more thrust

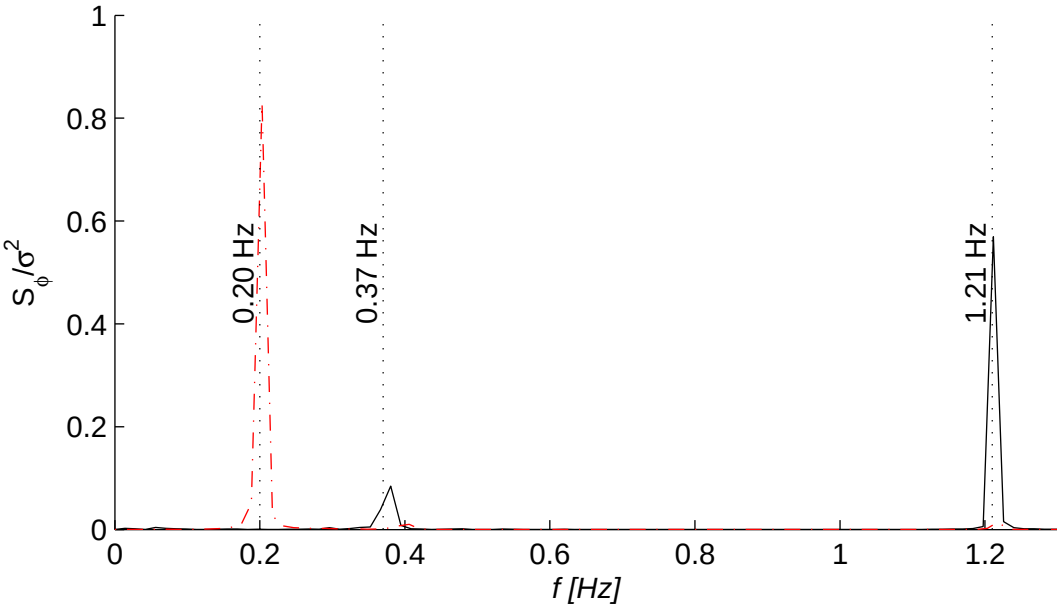

Figure 5.9: Power spectral density (PSD) for platform pitch at $T_w = 0.83$ s with static thrust (solid black) and variable thrust: $F_{thrust} = [0.86 - 1.36]$ N at 5 s (dot-dash red)

variation.

The effects of the control strategy as compared to a baseline case, no pitch control, are shown in figure 5.11. The y-axis gives a time-averaged pitch peak normalized by the time-averaged wave height, similar calculation as in the RAO, which is then normalized by the baseline case ($K_d = 0$). Results for $f_\phi = 10$ Hz (black circle) and $f_\phi = 20$ Hz (red square) are given. The maximum reduction in pitch was approximately 6.5% which is a result of a rotor speed variation of $\pm 15\%$. This is an insignificant reduction in pitch while undesirable consequences in power production and turbine loading may result. At prototype scale, using $T_w = 20$ s and $\Omega_r = 7.4$ rpm, this would be a 1 rpm variation with a frequency of 0.05 Hz.

Although peak values in pitch are not significantly affected, the distribution of pitch with respect to wave height is altered, as is seen in figure 5.12. As compared to the baseline case, the pitch control results in a narrowing of platform pitch for given wave height. Wave height measurements here are taken at -1D. This apparent narrowing of pitch with wave height is further investigated by looking at a pitch density distribution, figure 5.13, and the cross-correlation of H to ϕ, figure 5.14.

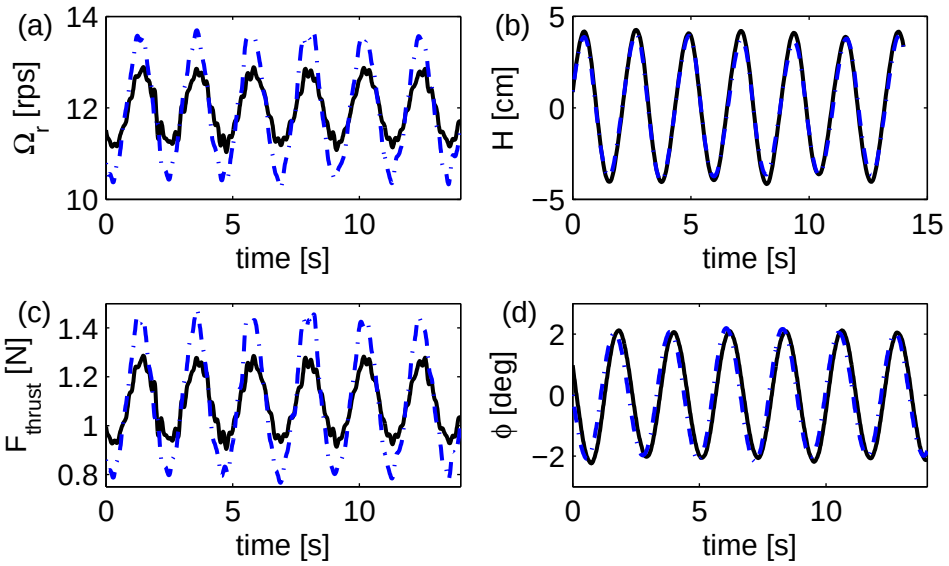

Figure 5.10: Rotor speed (a), corresponding rotor thrust (c), H recorded at -1D (b), and platform pitch ϕ (d) for $K_d = 22$ and $f_\phi = 20$ Hz (solid black) and $f_\phi = 10$ Hz (dot-dash blue)

Figure 5.13 compares the pitch distribution, normalized by H, for the baseline case, $K_d = 0$, and the pitch control case with the most impact on ϕ, $K_d = 22$ with $f_\phi = 10$ Hz. The slight reduction in peak pitch values of the pitch control scheme can be observed. However, as suggested by the distribution of ϕ_i with H_i in figure 5.12, there is not a large weighting of pitch values near the peaks. Pitch distribution at small angles (-20 to 20 deg m^{-1}) is nearly identical for the two cases. Pitch distribution with ϕ control does have an increased peak density of $\approx 15\%$ as compared to the baseline. The relatively unchanged pitch distribution density suggests there may be a change in phase between H and ϕ for the two cases, which would account for the narrowing of ϕ with H as observed in figure 5.12. Figure 5.14 (c) gives the cross-correlation of H to ϕ for the baseline case (solid), with time-series of ϕ and H given in (a), and $K_d = 22$ (dot-dash), with time-series of ϕ and H given in (b). The baseline ϕ lags wave height, as measured at -1D, by 0.8 s, or 36.2% of T_w. With the addition of pitch control ($K_d = 22$ with $f_\phi = 10$ Hz), the phase difference, or lag, changes to 1 s (45.3% of T_w). This is a difference, between the two phase lags, of $\approx 10\%$ of the wave period and helps explain

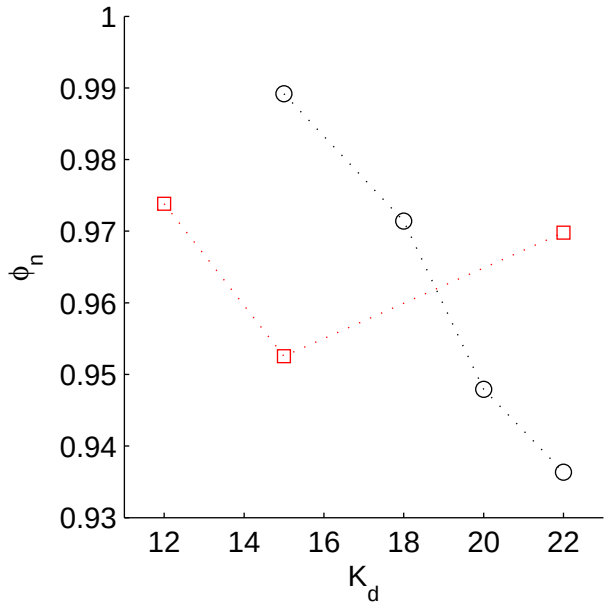

Figure 5.11: Time averaged pitch peak normalized by H and baseline pitch response ($K_d = 0$) $\phi_n = \frac{\phi_i/H_i}{\phi_0/H_0}$. $K_d = 22$ and $f_\phi = 10$ Hz (black circle) and $f_\phi = 20$ Hz (red square)

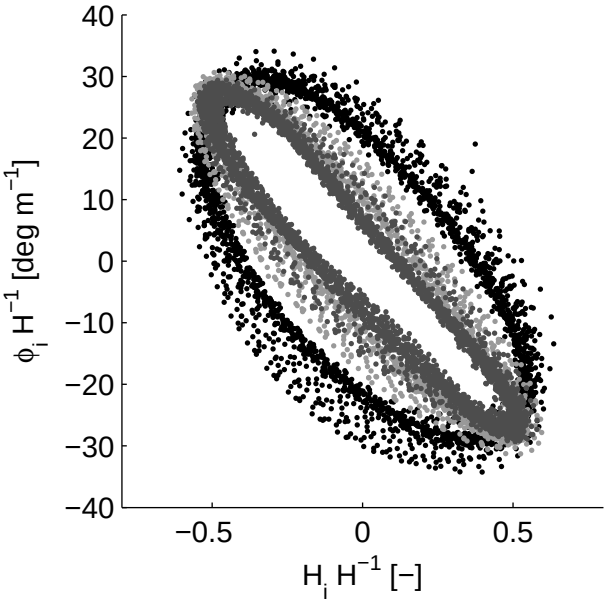

Figure 5.12: Normalized pitch distribution, $\phi_i H^{-1}$ [deg m^{-1}], by wave height, H_i H^{-1} [-]. Black: $K_d = 0$, light gray: $K_d = 18$, dark gray: $K_d = 22$ with $f_\phi = 10$ Hz

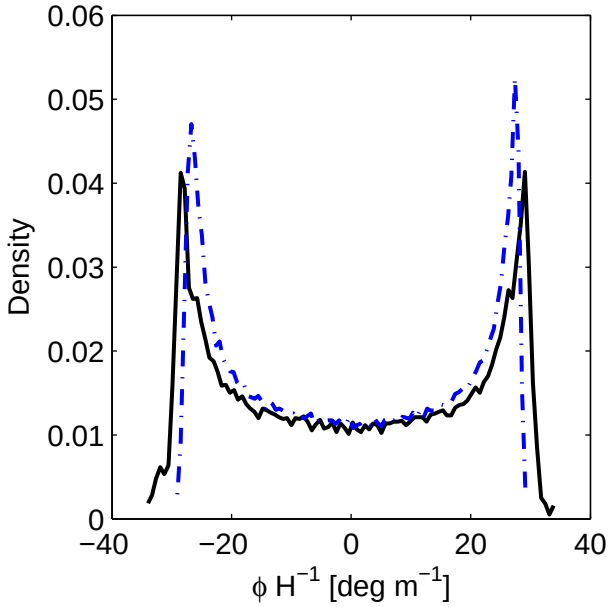

Figure 5.13: Normalized pitch distribution density by wave height, $\phi\ H^{-1}$ [deg m^{-1}] for $K_d = 0$ (solid black) and $K_d = 22$ with $f_\phi = 10$ Hz (dot-dash blue)

why the pitch mitigation strategy performs poorly. For the pitch control strategy to work optimally, the phase difference between Ω_r and ϕ, as Ω_r acts on the acceleration of ϕ, is 0.55 s, or 1/4 of T_w. Due to hardware limitations, the control loop is required to run four times before Ω_r is updated, this precise phase lag between measured ϕ and prescribed Ω_r is not maintained. Errors in the phase lag results in moments of rotor acceleration (increased thrust) during ϕ accelerations, causing increased pitching motion. Through the majority of the pitch oscillation, rotor thrust is acting to reduce pitch, however, during short periods rotor thrust acts to increase the pitching motion. The net result is an insignificant reduction in ϕ. This phase lag error can be observed in figure 5.15. The solid line represents the cross-correlation of Ω_r to ϕ with the lag having a value of 0.55s (1/4 of T_w) which is ideal. The dot-dashed line is the cross-correlation results for the ϕ control case being considered above. The lag for this control case is 0.31 s. This difference in phase lag is explained by in the hardware loop time required to update rotor speed.

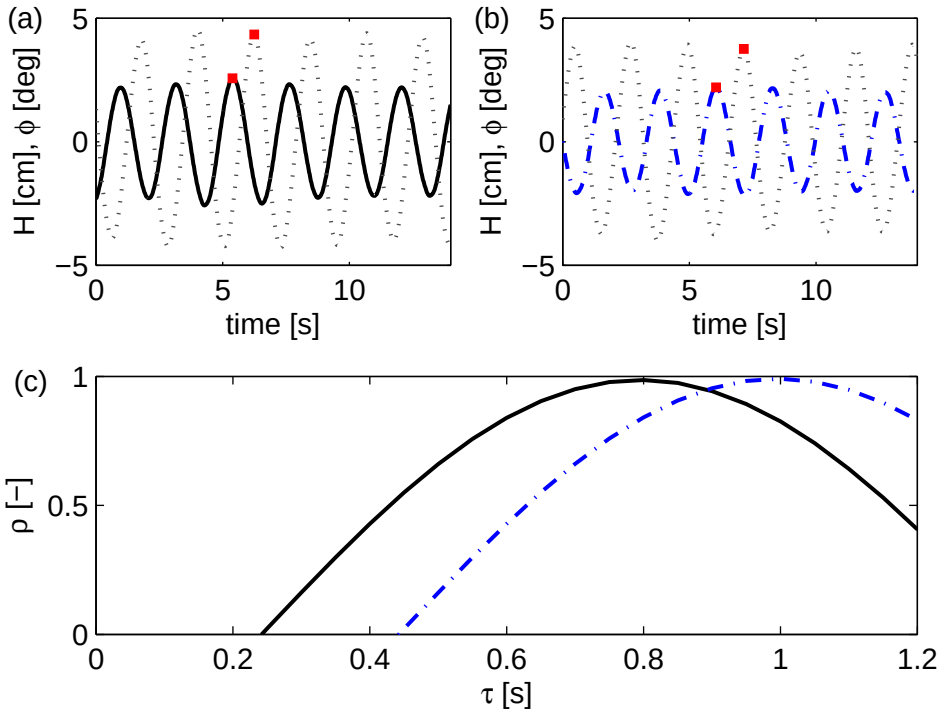

Figure 5.14: (a) Time-series of H (dot) and ϕ (solid) for $K_d = 0$. (b) Time-series of H (dot) and ϕ (dot-dash) for $K_d = 22$ with $f_\phi = 10$ Hz. (c) Cross-correlation of H to ϕ for $K_d = 0$ (solid black) and $K_d = 22$ with $f_\phi = 10$ Hz (dot-dash blue)

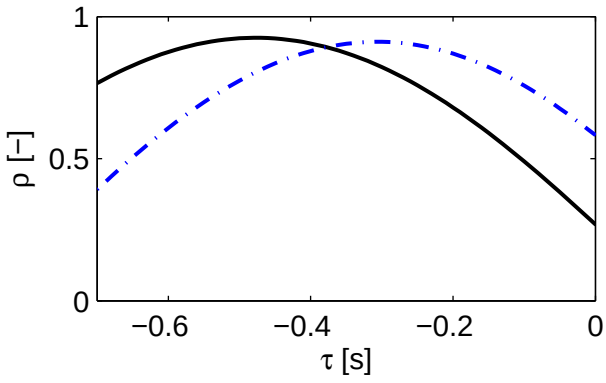

Figure 5.15: (Cross-correlation of Ω_r to ϕ for $K_d = 0$ (solid black) and $K_d = 22$ with $f_\phi = 10$ Hz (dot-dash blue)

Table 5.3: Pitch and Heave RAOs for baseline wind turbine system

T_w [s]	H [cm]	H_{rms} [cm]	Heave RAO [m m^{-1}]	Pitch RAO [deg m^{-1}]
3.00	0.96	0.07	0.85	41.97
2.85	1.09	0.17	-	76.94
2.65	0.99	0.10	0.94	262.84
2.60	1.26	0.04	-	384.29
2.52	1.43	0.09	-	506.53
2.50	1.42	0.10	-	532.85
2.50	1.45	0.11	-	498.62
2.48	1.45	0.15	-	555.18
2.47	1.37	0.11	0.99	403.58
2.45	1.39	0.10	-	360.02
2.43	1.37	0.09	-	345.76
2.41	1.37	0.09	-	305.95
2.41	1.41	0.07	-	284.33
2.39	1.43	0.09	1.00	249.97
2.26	1.19	0.08	1.00	185.26
1.80	2.22	0.07	1.04	37.18
1.51	1.94	0.05	1.04	21.50
1.13	2.84	0.09	0.92	7.38
1.03	2.42	0.10	1.08	-
1.01	2.43	0.09	1.21	8.12
1.00	2.90	0.11	0.95	6.58
0.99	2.90	0.10	-	5.13
0.96	2.77	0.12	0.98	7.40
0.91	3.41	0.12	0.47	5.15

Table 5.4: free decay response, natural frequencies

K_d [-], f_ϕ [Hz]	Ω_r range [rps]	F_{thrust} range [N]
12, 20	11.5-12.5	1.0-1.2
15, 20	11.3-12.7	0.95-1.25
22, 20	11.0-12.9	0.9-1.3
15, 10	10.8-13.3	0.9-1.35
18, 10	10.6-13.4	0.85-1.4
20, 10	10.4-13.5	0.8-1.45
22, 10	10.2-13.7	0.75-1.5

Chapter 6

Experimental setup: wind tunnel

Phase II work investigates the turbine-wind interaction of a scale model under pitching and heaving motions in a turbulent boundary layer. Constant temperature anemometer (CTA) cross-wire, wall-parallel PIV, and downwind, static turbine voltage measurements are used to characterize the wake behind a model OFWT. The model wind turbine used in this set of experiments, originally designed and built by Leonardo P. Chamorro and James Tucker of SAFL, utilizes a fixed tip-speed ratio (TSR), and a DC generator with the ability to capture voltage or apply a torque to manipulate rotor speed (vary TSR). The hub height, z_{hub}, is 10.4 cm and rotor diameter, D, is 12.8 cm.

6.1 Wind tunnel

Phase II experiments were performed in the closed-circuit atmospheric wind tunnel at the St. Anthony Falls Laboratory (SAFL), within the University of Minnesota - Twin Cities. The wind tunnel has a length of 37 m with a 16 m test section. The test section has a cross-section of 1.5 x 1.7 m (W x H) where the roof is adjustable in order to enforce zero pressure gradient in the streamwise direction. Upwind of the test section is a contraction with a 6.6:1 area ratio. Preceding the contraction is an aluminum honeycomb and coarse wire mesh designed to straighten the flow and produces a uniform, turbulent flow at the contraction inlet. At the beginning of the test section a flow trip is used, 0.04 m picket fence, to generate a turbulent boundary layer over a smooth surface. By controlling the wind tunnel height, a zero pressure gradient in the

streamwise direction is achieved, resulting in a fully developed boundary layer. Figure 6.1 is a photograph of the wind tunnel test section with the oscillating wind turbine shown.

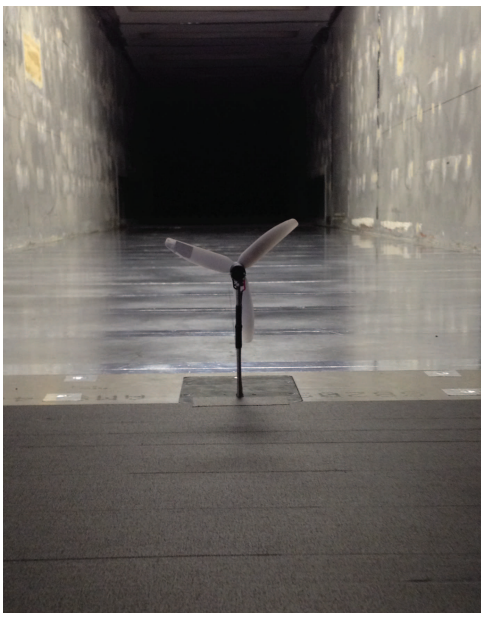

Figure 6.1: Wind tunnel test section photograph

Wind tunnel temperature of the air and test section floor are controlled to create a neutrally-stratified boundary layer. Air temperature is controlled via heat exchanger, downwind of the flow driving fan and upwind of the test section contraction, to ±0.1 deg C with temperature measurements made within the freestream at the end of the test section by thermocouples (E type). Floor temperature is controlled through circulating a water-glycol mixture within the aluminum test section floor to ±0.1 deg C. Temperature of the floor is measured at the end of the test section, as with the air, with a thermocouple (E type).

Figure 6.2 shows the vertical profiles of the mean velocity (a), turbulence intensity (b), and turbulent shear stress (c), measured in the boundary layer with a CTA cross-wire at 10 kHz and no wind turbine present. The hub height velocity was measured as $U_{hub} = 2.26$ m s^{-}1 which is used to normalize the vertical profiles. The zero pressure gradient, neutrally stratified boundary layer has a Reynolds number, based on the shear

Table 6.1: Turbulent boundary layer flow characteristics and scaling parameters

D [m]	z_{hub} [m]	δ [m]	T [deg C]	ν [m^2 s^{-1}]	U_{hub} [m s^{-1}]	U_∞ [m s^{-1}]	u_* [m s^{-1}]	Re_D [-]
0.128	0.104	0.4	20	1.6e-5	2.26	2.73	0.01	18276

velocity, of $Re_\tau \approx 0.3 \times 10^4$ where $Re_\tau = u_* \delta / \nu$. The shear velocity, or friction velocity, u_* is found by fitting the logarithmic law of the wall, equation 6.1, to the meausured velocity profile. A friction velocity of $u_* = 0.01$ m s^{-1} was estimated. The logarithmic law of the wall is defined as

$$U = \frac{u_*}{\kappa} \ln \frac{z}{z_0}, \tag{6.1}$$

where κ is the Von Kármán constant, taken as 0.35, and z_0 is the aerodynamic surface roughness length estimated to be 0.03 mm. The boundary layer height, δ, is approximately 0.4 m in height which is roughly four times the model wind turbine hub height.

Table 6.1 summarizes the boundary layer characteristics as well as scaling parameters, i.e. rotor diameter, D, and hub height, z_{hub}. Re_D is the Reynolds number associated with the rotor diameter and is calculated as $Re_D = U_{hub} D / \nu$.

6.2 Wind turbine model

The wind turbine model(s) used in Phase II experiments consists of three-blades (GWS/EP-6030x3), giving diameter $D = 0.128$ m, fixed to a small DC generator (2 V). Geometric similarity between the prototype wind turbine and the wind tunnel model, using the rotor diameter, gives a scaling ratio of 1/1562.5. The model hub height is 0.104 m which occupies approximately 25% of the lower portion of the boundary layer. This is consistent with utility-scale wind turbines in the atmospheric boundary layer. The top-tip position, $z_{top-tip}$, is 0.168 m and the bottom-tip, $z_{bottom-tip}$, is located at 0.040 m.

Figure 6.3 gives a schematic of the model turbine. A front view, looking downstream, is shown in (a). The z axis is vertical, with zero position coinciding with the wind tunnel floor and positive pointing up, is aligned with the tower and corresponds with the vertical velocity component, W. The y axis is aligned with the spanwise velocity, V, and has a

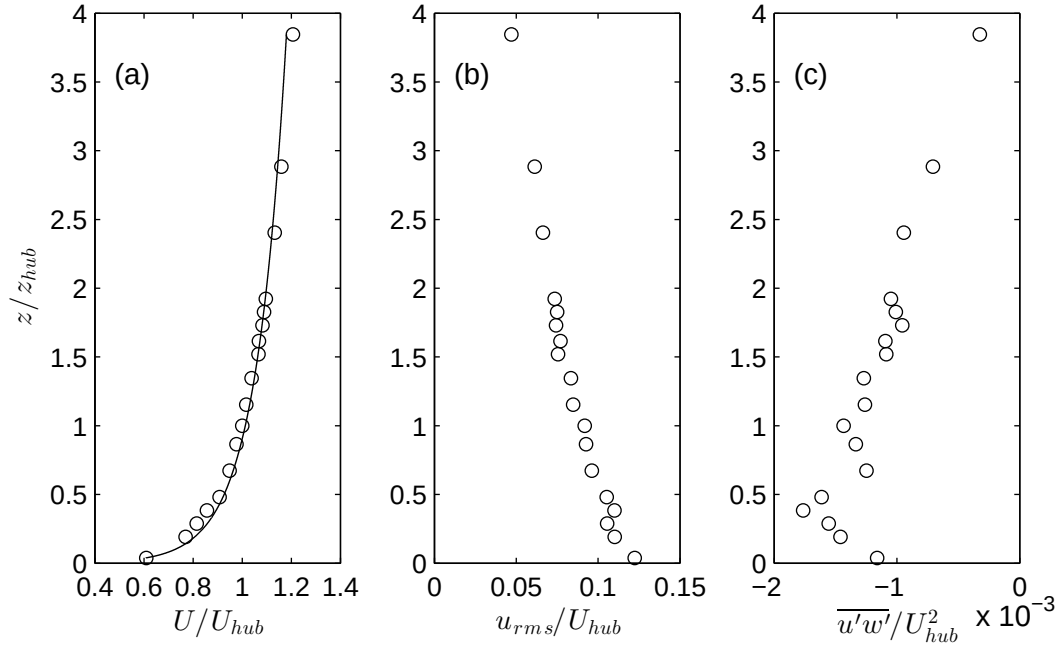

Figure 6.2: Turbulent boundary layer characteristics: (a) mean vertical velocity profile at turbine location with logarithmic law of the wall fit, (b) turbulence intensity, and (c) kinematic shear stress. Height, z, is normalized by the turbine hub height, z_{hub}. Velocity characteristics are normalized by the velocity at hub height, U_{hub}

zero position along the centerline of the nacelle/tower. A side view is presented in (b), looking in positive y direction. The x axis is aligned with the streamwise velocity, U. Pitch is defined as a rotation about the y axis and has a zero value aligned with the z axis. Positive pitch is a rotation forward, into the flow, as illustrated in the figure.

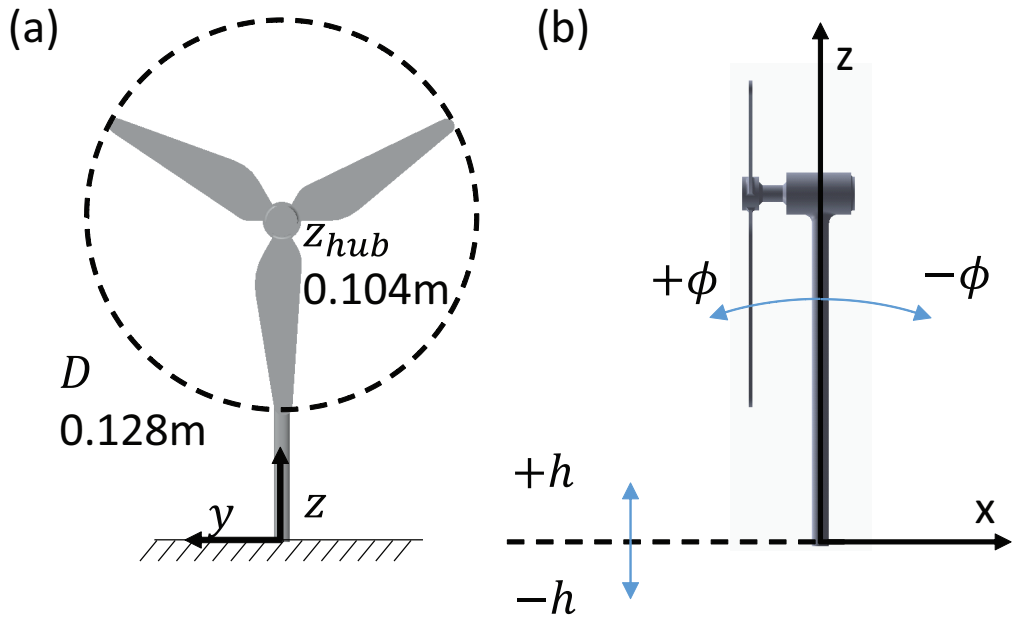

Figure 6.3: Model wind turbine schematic, (a) front view ($y-z$ plane) and (b) side view ($x-z$ plane)

The rotor is fixed to the shaft of the DC motor generating a voltage linearly proportional to the incoming flow speed. This linear increase in voltage with U_{hub} is a result of a constant tip-speed ratio (TSR), λ. TSR is the ratio between the tangential velocity of the blade tip and the wind speed at hub height and is defined as $\lambda = \omega r/U_{hub}$ where r is the rotor radius ($0.5D$) and ω is rotational speed of the rotor [rad s^{-1}]. Constant TSR results from a proportional increase in both electrical torque and friction with increasing aerodynamic torque. TSR for the free-spinning rotor, i.e. no electrical current is applied to the motor to slow the rotational speed, was found to be $\lambda = 4.5$. This tip-speed ratio is within the range of utility-scale wind turbines, where λ is between 3 and 9, and has been determined to be a significant parameter in wake development in previous studies.

Wind tunnel and engine dynamometer tests were conducted by [26] to evaluate the

model wind turbine performance, i.e. power coefficient, C_p. The maximum C_p was found to be 0.16 at $\lambda = 3$. Work outlined in chapter 7 will include results with the turbine operating in a free-spinning condition, $\lambda = 4.5$ and $C_p \approx 0$, and operating at the optimal TSR, $\lambda = 3$ and $C_p = 0.16$. Optimal TSR is obtained by applying a current to the DC generator, via external constant-current power supply, effectively increasing electrical torque and slowing the rotor.

One of the major challenges in studying the wake behind a pitching and heaving wind turbine is the temporal scaling from prototype to wind tunnel scale. The question therefore is, at what frequency should the wind tunnel model fluctuate in pitch and/or heave in order to represent the dynamics at utility-scale. Conventional Reynolds number scaling, based on rotor diameter and U_{hub}, is not practical and would require the turbine to oscillate in these modes at several thousands of Hz. [27] reports if the Reynolds number of the wake flow is sufficiently large, the wake development will be similar. That is, many features such as the tip vortices and wake rotation will be the same in the model and full scale. Consequently, a new scaling method would need to be developed. As will be discussed in §6.4, there are limitations on the frequency at which the model turbine can be oscillated. The system used to oscillate the turbine, the linear actuation system, was designed to allow frequencies up to 10 Hz, however, practically, the model turbine would not be able to withstand the accelerations. A value of 4 Hz was set as the maximum frequency at which to vibrate the system in pitch and heave. This limitation was a major driver in the scaling approach.

The first approach utilized the ratio between the rotor and wave frequency as

$$\frac{f_{r,p}}{f_{w,p}} = \frac{f_{r,m}}{f_{w,m}}, \tag{6.2}$$

where f_r is the rotor frequency and f_w is the wave frequency. The p and m subscripts denote prototype and model scale respectively. The turbine model provided some control of rotor frequency where the rotor could be slowed in order to decrease the required frequency at which to oscillate. $f_{w,m}$ is controlled by setting the oscillation frequency of the actuator system.

At prototype scale, the rotor frequency at rated speed is $f_{r,p} = 0.12$ Hz. Using results from the wave basin testing, specifically the range of wave periods used to generate the Response Amplitude Operator, and scaling up to prototype scale, the wave frequency

has a range of $f_{w,p} = [0.04 - 0.1]$Hz. Wind tunnel tests will be performed with a hub height, streamwise velocity of 2.5 m s^{-1}. This velocity was chosen as it would reduce the rotor speed allowing for slower oscillations in pitch and heave and is within the operational wind speed range for the model turbine. At this wind speed, the model turbine has an adjustable rotor frequency range of $f_{r,m} = [20 - 28]$Hz. $f_{r,m} = 20$Hz corresponds with the optimal TSR of $\lambda = 3$ and $f_{r,m} = 28$Hz corresponds with a free-spinning rotor (frictional loading only) and TSR of $\lambda = 4.5$. Solving for $f_{w,m}$ in equation 6.2 gives a range of oscillations of $f_{w,m} = [5.6 - 25.9]$Hz. As mentioned earlier, a mechanical limitation on the oscillation frequency has been set as 4 Hz. As such, a different time scaling scheme was developed.

Of specific interest in the wake study of an oscillating wind turbine was how the meandering wake, large scale oscillations in the flow related to the vortex shedding of the rotor, would be effected, i.e. as compared to a static turbine. Recent experimental work on the topic of wake meandering for wind turbines have suggested a range of Strouhal numbers which characterize this large-scale instability in the far wake. The Strouhal number is a dimensionless parameter which describes the oscillating wake mechanisms behind a body in a flow and is defined as

$$St = fD/U, \tag{6.3}$$

where f is the frequency of the oscillation, D is the characteristic length of the body, and U is the free stream speed. In the near wake behind a model wind turbine, where measurements were made one diameter downstream, [27] suggests a Strouhal number ranging from 0.1 to 0.3. Far wake measurements in a study performed on a hydrokinetic turbine by [28], and computational modeling by [29], gave a Strouhal number of approximately 0.28. Most recently, measurements in the far wake of a model wind turbine found a Strouhal number of 0.23 for instabilities associated with the rotor [25].

Using the range of Strouhal numbers associated with the meandering wake behind a static turbine, this work looks at oscillating a model turbine at a frequency similar to that of the wake meandering. That is, based on the inflow velocity at hub height, the geometric properties of the rotor, and using the range of Strouhal numbers from literature, use equation 6.3 to estimate the frequency of the large-scale instabilities in the wake and oscillate the model turbine in pitch and/or heave at a similar frequency.

Following this idea we have $U = U_{hub} = 2.5$ m s^{-1}, $St = [0.1 - 0.3]$, and $D = 0.128$ m. Equation 6.3 is solved for f which gives a range of $f = [2 - 6]$ Hz. Taking mechanical limits into consideration and the range of frequencies determined from the Strouhal number range, an oscillation frequency of 3 Hz was chosen for the test cases. The test cases will be outlined in §7.

6.3 Data acquisition and control: wind tunnel

The data acquisition and control system used in the wave basin experiments was also used in the wind tunnel tests. The major differences are the number of electric motors being controlled, two motors as compared to one in the wave basin, the addition of a digital input/output module (NI 9403 with 140 kS-s^{-1}), and the speed of the measurements (10,000 Hz). The objectives of the data acquistion and control system were the following:

1. precise control of a linear actuator system (two electric motors) which provides the heave and pitch motion of the model wind turbine (vertical position accuracy within 0.05 mm)

2. High temporal resolution (10 kHz) flow measurements with CTA cross-wire synchronized with turbine postion, velocity, and acceleration

3. PIV measurements synchronized with motor turbine position, velocity, and acceleration.

A custom LabVIEW program was written to control the position of the turbine (motor position) and acquire flow measurements/signals. Model turbine motion in pitch and heave are sinusoidal motions with a defined amplitude and frequency. Turbine motion profiles for pitch, heave, and combined pitch and heave are generated in MATLAB where the amplitude and frequency of the motions are prescribed. Pitch and heave positions are then converted to motor revolution positions and loaded into the LabVIEW motion control program. Details on the motion control mechanism are presented in the following section. The system then simultaneously moves the model turbine, following the commands for sinusoidal motion in pitch and/or heave, and acquires either cross-wire

measurements or PIV laser pulse signal. The PIV laser pulse signal is used for syncing the PIV images with motor positions.

The system will operate in two different measurement configurations which are based on the device being used to measure the wake flow, i.e. cross-wire of PIV. For cross-wire measurements, turbine position and cross-wire voltage measurements are synced in time and captured at 10 kHz to provide high-resolution measurements in the wake. The second configuration used wall-parallel PIV measurements captured at 7.25 Hz and synced in time with turbine position measurements being recorded at 10 kHz. Note, turbine position measurements are recorded at 10 kHz for convenience with respect to data reduction.

The cross-wire, which will be termed as hotwire, measured the streamwise and vertical velocity components at 10 kHz. The hotwire sensor consisted of two tungsten wires with diameter of 5 μm and was connected to an A.A. Lab Systems AN-1003 10-channel CTA/CCA amplifier system. Output from the amplifier was recorded by the data acquisition and control system. The hotwire was calibrated using a range of velocities from approximately 0.5 m s^{-1} to 5 m s^{-1}, the range of velocities exceeded any velocities expected in the experiment. In total, nine calibration velocities were used. At each calibration velocity, the hotwire probe was rotated from +30 to -30 degrees by 10 degree increments. The angle was defined as the angle from the streamwise velocity. Temperature during the calibration was maintained to within $\pm$0.2 degree C of the test temperature. Voltage measurements from the hotwire were calibrated against pitot tube pressure measurements using a look-up table calibration method [30].

Figure 6.4 gives a schematic of the model wind turbine located in the turbulent boundary-layer within the wind tunnel. Hotwire measurements are taken in the wake of the model turbine at $y/D = 0$ and various x and z positions. Spatial measurements in the streamwise direction are taken at $x/D = 1, 2, 3, 4$ and 5 for $z = z_{hub}$ and $z_{top-tip}$. A refinement in vertical measurement positions is performed at $x/D = 5$ with measurements starting at 4 mm above the floor and continuing up to 40 cm. This creates a detailed vertical profile at $x/D = 5$ which is a location generally considered as the minimum horizontal spacing in wind farms (typical range of $5 - 10D$ for streamwise spacing).

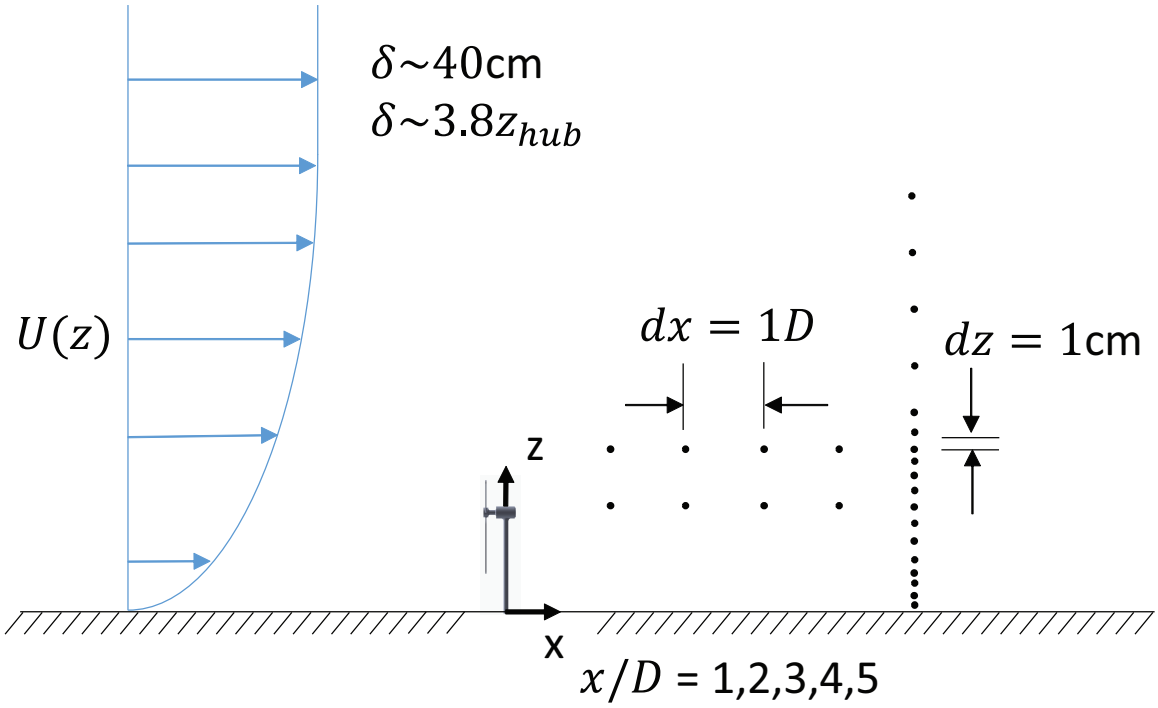

Figure 6.4: $x - z$ plane view of wind tunnel setup, CTA crosswire measurements resprented by dots.

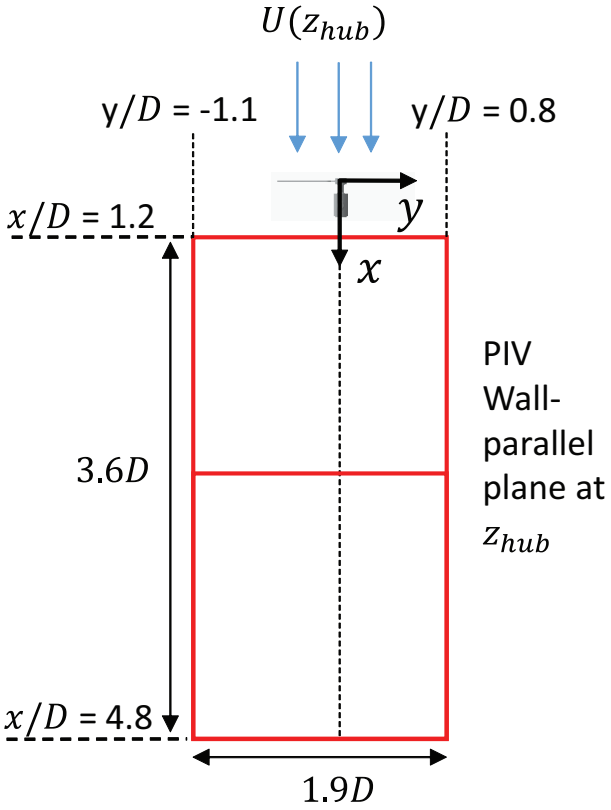

Figure 6.5: PIV schematic

PIV measurements were also made in the turbine wake horizontal plane with $z = z_{hub}$ for spatially resolved streamwise and spanwise velocity components. Figure 6.5 gives a schematic of the PIV measurement window. The measurement windows spans from $y/D = -1.1$ to $y/D = 0.8$ and in the streamwise direction from $x/D = 1.2$ to $x/D = 4.8$. The PIV system consisted of two CCD cameras with 2048 by 2048 pixel resolution. These cameras simultaneously captured images to generate the large field of view observed in figure 6.5. Additional components included TSI Insight 4G software coupled with a TSI synchronizer controlling the timing of the laser and cameras. The laser used was a Big Sky dual-head Nd:YAG laser which illuminated olive oil particles, with diameter on the order of 10 microns, used to seed the flow. The oil particles were generated by a Laskin nozzle and entrained into the flow.

6.4 Linear actuator system

A dual linear actuator system was used to perform the desired motions of pitch and heave on the model wind turbine. The actuator system was located under the wind tunnel floor so as to not affect the flow. Figure 6.6 shows (one of) the wind tunnel floor panel where the actuator system was attached. As is shown, only the turbine is above the floor and within the boundary layer. All moving components for the actuator system are located below the floor panel.

The system is comprised of two linear actuators by Ultra Motion. Each linear actuator is driven by a brushless DC servo motor, AKM11B, capable of applying 0.61 Nm and rotational speeds up to 4000 rpm. The DC motor drives a belt which in turn drives a screw through a 1:1 speed ratio. The screw converts the rotation to a vertical displacement through a known conversion factor, 0.01016 meters per revolution. Precise motor position is captured by a Smart Feedback Device (SFD), 2^{24} counts per revolution, which is recorded by the LabVIEW system. Each actuator is connected to the model turbine, which is attached to a plate, through a hinge allowing for the pitch rotation. Theoretically, the system is capable of motion at speeds up to 10 Hz with amplitude of approximately $0.1z_{hub}$. However, a practical limit of 4 Hz was decided, based on longevity of the system.

A detailed view of the linear actuator system, specifically the rotation mechanisms,

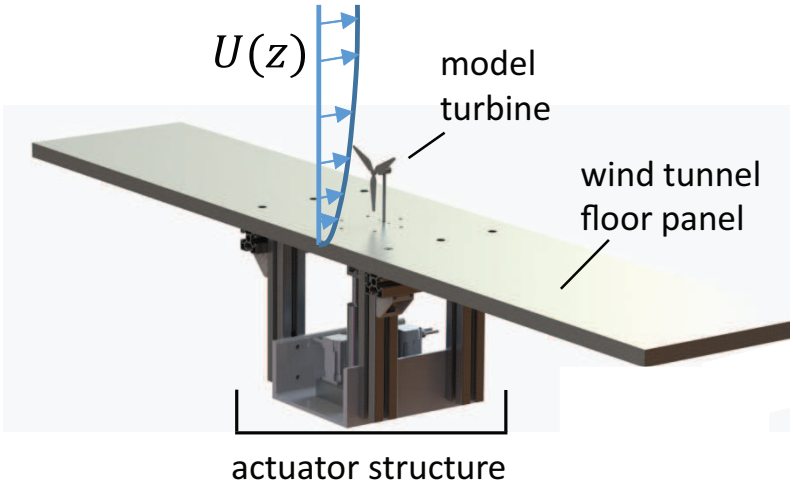

Figure 6.6: Overview of actuator system

is shown in figure 6.7. Figure 6.7 (a) gives a front view, $y-z$ plane, with the wind tunnel floor being represented by the dashed line. Figure 6.7 (b) is an isometric view of the system. Shown are the two actuators at the connection point to the model turbine. The mechanism consists of a mid-actuator and a front-actuator. Each actuator is attached to a plate through a bracket and hinge. The model turbine is then attached to the plate. The mid-actuator includes a single hinge which acts as the pitch axis. Additionally, the mid-actuator acts as the primary driver for heaving motion and fixes the turbine in the x and y directions. The front actuator comprises a dual-hinge mechanism which allows for the pitching motion and is the primary driver of pitch. The two actuators work in tandem to provide the desired heave in time, $h(t)$. The front actuator matches the heave value of the mid-actuator and then deviates to create the pitching motion in time, $\phi(t)$.

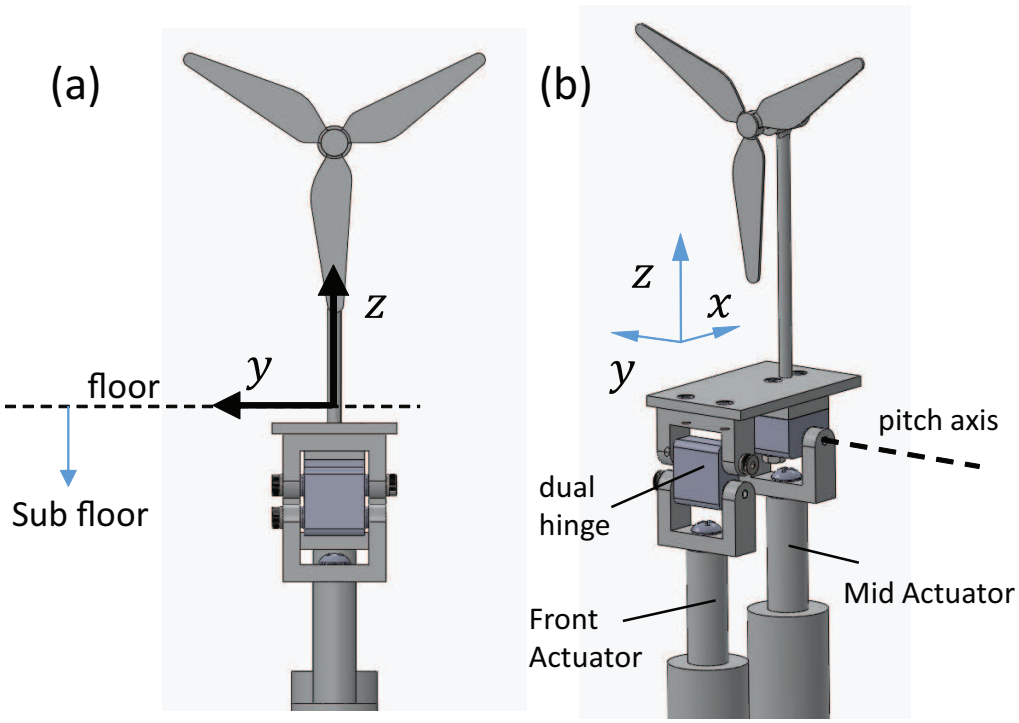

Figure 6.7: Detail view of actuator attachments for the model wind turbine. (a) front view ($y-z$ plane) with wind tunnel floor represented by the dotted line. (b) isometric view showing the mid and front actuators

Chapter 7

Results: wind tunnel

7.1 Wind turbine motion cases

The response amplitude operator (RAO) generated in the wave basin study is used to predict the wind turbine motion response due to a known wave period, T_w, and wave height, H. A single point, with respect to T_w, on the RAO was chosen with which to replicate the predicted motion of the model turbine in the wind tunnel. The main factor behind choosing this point in the RAO was a desired pitch amplitude, ϕ_{amp}, of 4 degrees. A pitch amplitude of 4 degrees was chosen as it is on the extreme end of pitch values associated with typical wave heights (as suggested by data from PNW). The second driving factor in choosing this specific operating point was to investigate extreme wave heights, specifically wave heights near 10 m (prototype scale, equivalent to 10 cm at wave basin scale). This allowed a separate investigation of pitch and heave, that is moving the turbine in only one of the degrees of freedom, where both would be operating in extreme conditions. Separating the two forms of motion would give insight into which type of motion would most contribute to large scale variations, if any, in the mean wake flow.

With the desired pitch and heave amplitudes in mind, a point was solved for using the RAO. The point chosen corresponds to $T_w = 2$ s (wave basin scale). This point gives a heave response of 1.02 m m^{-1} and a pitch response of 74.26 deg m^{-1} for a given wave height. Figure 7.1 shows the RAO point chosen, represented by the solid circle, for heave (left) and pitch (right). To achieve $\phi_{amp} = 4$ a wave height of $H = 10.77$

cm is required. This wave height gives a heave amplitude of $h_{amp} = 5.5$ cm at wave basin scale, $h_{amp} = 5.5$ m at prototype scale, and $h_{amp} = 3.5$ mm at wind tunnel scale ($h_amp \approx 0.03 z_{hub}$).

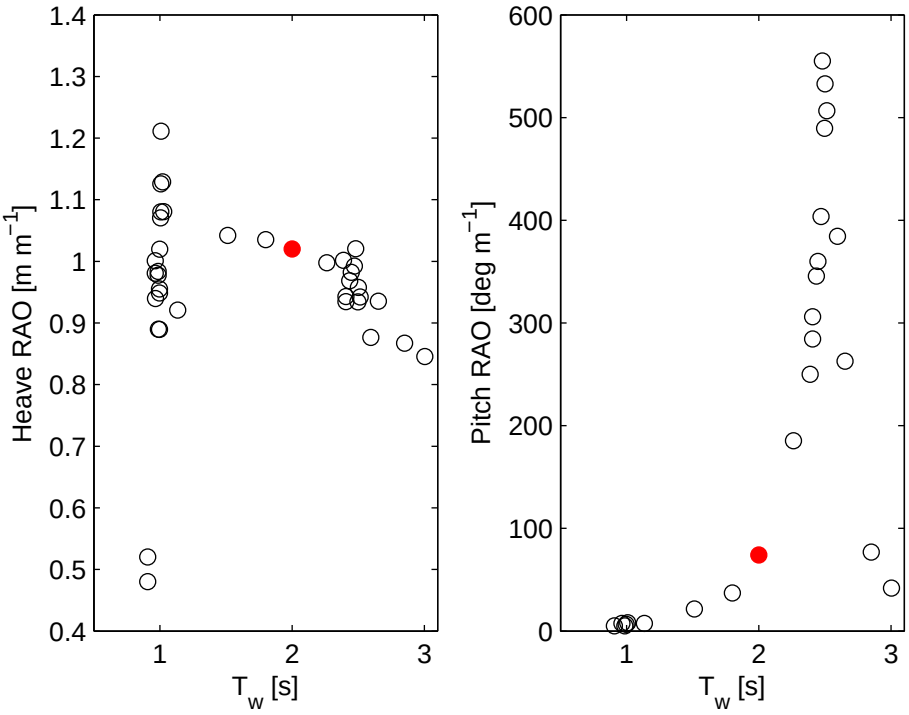

Figure 7.1: Response amplitude operator (RAO) for heave (left) and pitch (right). Solid circle indicates the point chosen for wind tunnel testing

The wind turbine motion cases studied are as follows:

- Static turbine: free-spinning rotor, $\lambda = 4.5$ (static fr case)
- Pitch only: oscillating turbine at 3 Hz, $\phi_{amp} = \pm 4$ degrees, $\lambda = 4.5$ (pitch case)
- Heave only: oscillating turbine at 3 Hz, $h_{amp} = \pm 0.03 z_{hub}$, $\lambda = 4.5$ (heave case)
- Static turbine: optimal TSR, $\lambda = 3$ (static opt case)
- RAO: coupled pitch and heave, oscillating turbine at 3 Hz, optimal TSR, $\lambda = 3$ (RAO case)

Table 7.1: Summary of platform pitch control test cases

case	f_w [Hz]	ϕ_{amp} [deg]	h_{amp}	λ	measurement method
static fr	0	0	0	4.5	PIV, hotwire
pitch only	3	± 4	0	4.5	PIV, hotwire
heave only	3	0	$\pm 0.03 z_{hub}$	4.5	PIV
static opt	0	0	0	3	PIV, hotwire
RAO	3	± 4	$\pm 0.03 z_{hub}$	3	PIV, hotwire

- $\phi_{amp} = \pm 4$ degrees
- $h_{amp} = \pm 0.03 z_{hub}$
- ϕ leads h by $0.34T$ where T is the oscillation period

Table 7.1 summarizes the test cases performed in the wind tunnel as well as the flow measurement sensor used. Comparison of results are broken down by TSR used in each case. The static turbine, pitch only, and heave only cases are compared against each other, where all cases use TSR of $\lambda = 4.5$. This set of comparisons allows insight into which mechanism, pitch or heave, will have a greater effect on the aerodynamic wake. The static turbine and RAO case, where TSR of $\lambda = 3$ was used, compares a static turbine to an oscillating turbine in both pitch and heave. This case is of significant importance for verifying computational models as well as giving insight into any coupling effects of the two forms of motion on the wake.

7.2 Mean streamwise flow profiles

This section covers the results of hotwire and PIV measurements for the mean streamwise velocity component in the aerodynamic wake for the different test cases. Figure 7.2 gives a vertical profile for the average streamwise velocity $U(z)$, normalized by U_{hub}, for the different turbine test cases at $x/D = 5$ and $y/D = 5$. Results are shown for hotwire measurements of the static turbine cases, optimal and free-spinning TSR, the pitch only case, free-spinning TSR, and the RAO case, optimal TSR. The non-uniform, boundary-layer, incoming flow results in a non-axisymmetric velocity reduction within

the wake of the turbine. However, as seen in figure 7.3, the velocity deficit is largely axisymmetric with the axis of symmetry located at z_{hub}. Axisymmetry starts to break down near the surface. Velocity deficit is defined as $\Delta U(z) = U_{case}(z) - U_{base}(z)$ where $U_{case}(z)$ is the average streamwise velocity for a specific turbine case, as outlined in table 7.1, and $U_{base}(z)$ is the average streamwise velocity of the incoming boundary-layer (baseline).

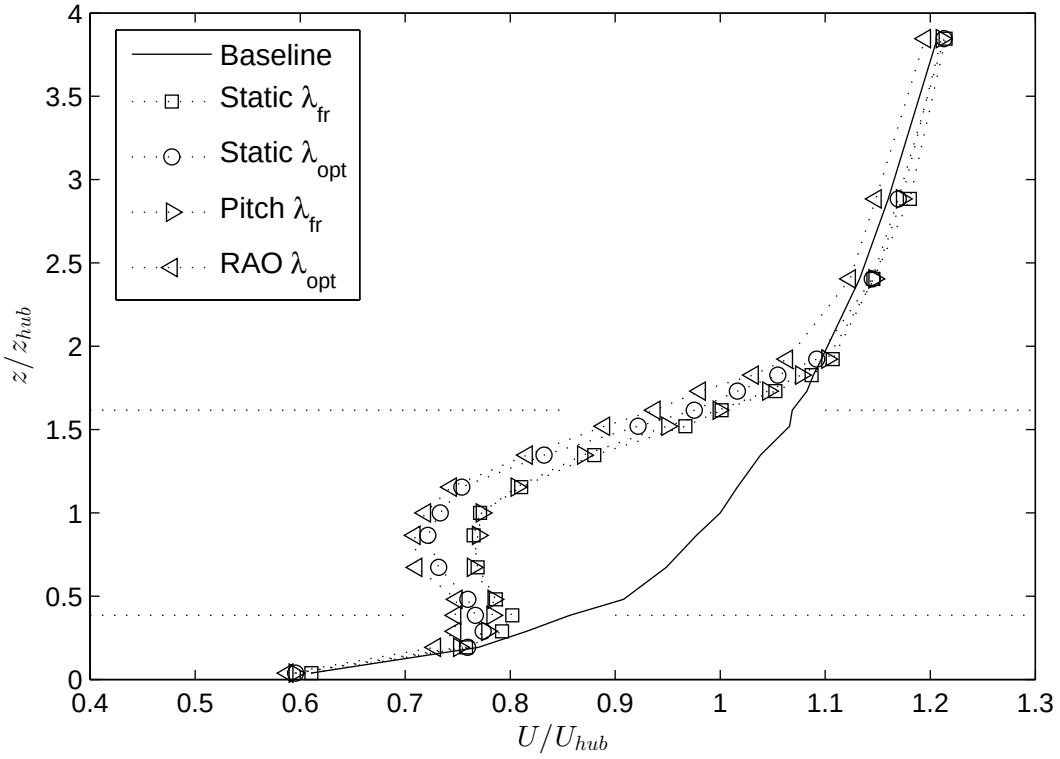

Figure 7.2: Vertical profile of average streamwise velocity $U(z)$ normalized by U_{hub} in the wake measured at $x/D = 5$ and $y/D = 0$ for different turbine operating configurations. Horizontal dotted lines represent bottom and top-tip locations. Baseline - no turbine present

In general, the results show very similar trends and values in the velocity reduction for all turbine cases. That is, no significant differences exist in the average velocity between turbine cases where TSR is consistent. The optimal TSR cases, static and RAO, show an increased velocity deficit as compared with the free-spinning rotor cases due to increased energy capture. The largest velocity deficit with respect to baseline

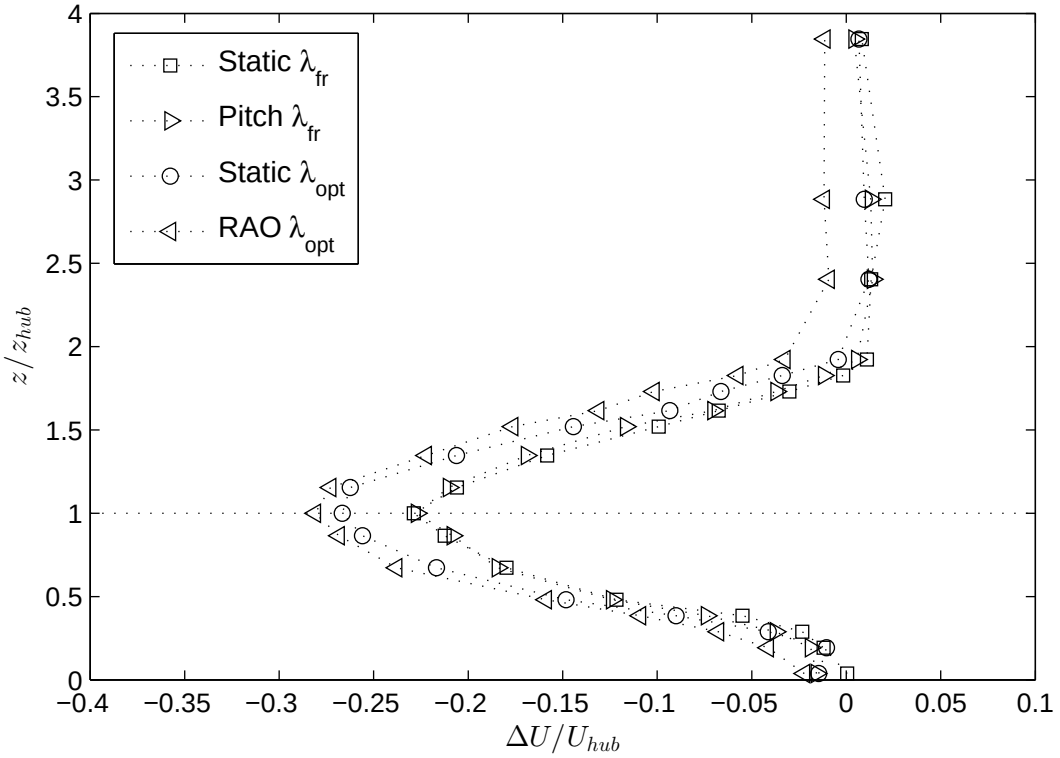

Figure 7.3: Vertical profile of the velocity deficit $\Delta U/U_{hub}$ in the wake measured at $x/D = 5$ and $y/D = 0$ for different turbine operating configurations. Horizontal dotted line represents the hub location

flow is observed at hub height. Minimal mean shear, dU/dz, is observed in the lower half of the wake (hub to bottom-tip). However, large shear is observed in the upper half (hub to top-tip). The trends and weak differences between the turbine cases are also observed in streamwise measurements along z_{hub} and $z_{top-tip}$ for $x/D = 1, 2, 3, 4$, and 5. Figure 7.4 gives the streamwise profiles at the two z locations. Wake recovery with increasing x is observed in (a). As with the vertical profile, here there are no significant differences in wake recovery between the turbine cases where TSR is consistent.

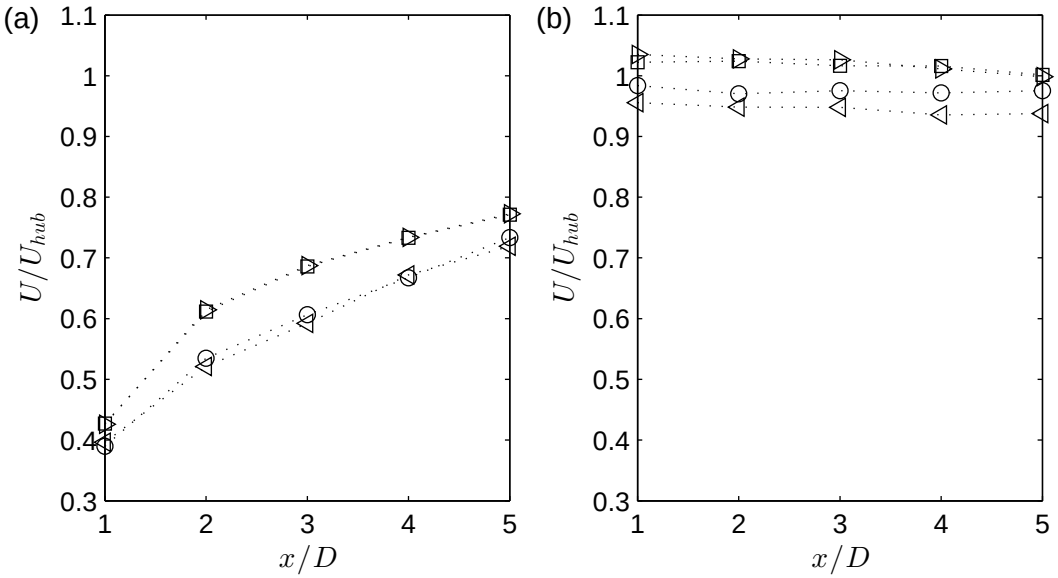

Figure 7.4: Streamwise profile of average streamwise velocity U normalized by U_{hub} in the wake measured at z_{hub} (a) and $z_{top-tip}$ (b) for $x/D = 1, 2, 3, 4$, and 5 and $y/D = 0$. Symbols used are the same as those for figures 7.2 and 7.3

Here, we will specifically compare the results from the RAO case and the static turbine where $\lambda = 3$, as is shown in figure 7.5 which gives average streamwise profile $U(z)/U_{hub}$. At $z(\delta)$ there is a small difference in velocity between the cases as $U(\delta)$ does not completely converge. This accounts for approximately a 1% difference of U_{hub} between the cases. Near the top-tip, $z/z_{hub} = [1.5 - 2]$ there is a difference of $\approx 4\%$ of U_{hub} with the RAO case having a slight increase in velocity deficit. Accounting for the difference at $z = \delta$, it is a good assumption that the RAO case has an increase in velocity deficit, as compared to the static turbine, of 2-3% of U_{hub}. Near the hub

and in the range $z/z_{hub} = [0.5 - 1.5]$ differences are very small. When considering the velocity difference at $z = \delta$, a variation of $< 1\%$ of U_{hub} is observed. In the region of the bottom-tip ($z/z_{hub} = [0.2 - 0.5]$), an increase in the velocity deficit for the RAO case is again observed ($\approx 2\%$ of U_{hub}). These larger differences near the top-top and bottom-tip are likely attributed to the dynamic location of the rotor tips due to the pitching and heaving motions. However, these difference are very small, less than 3% of U_{hub} everywhere, and a general conclusion of weak differences in the mean streamwise velocity at $x/D = 5$ between an oscillating and static turbine is being made.

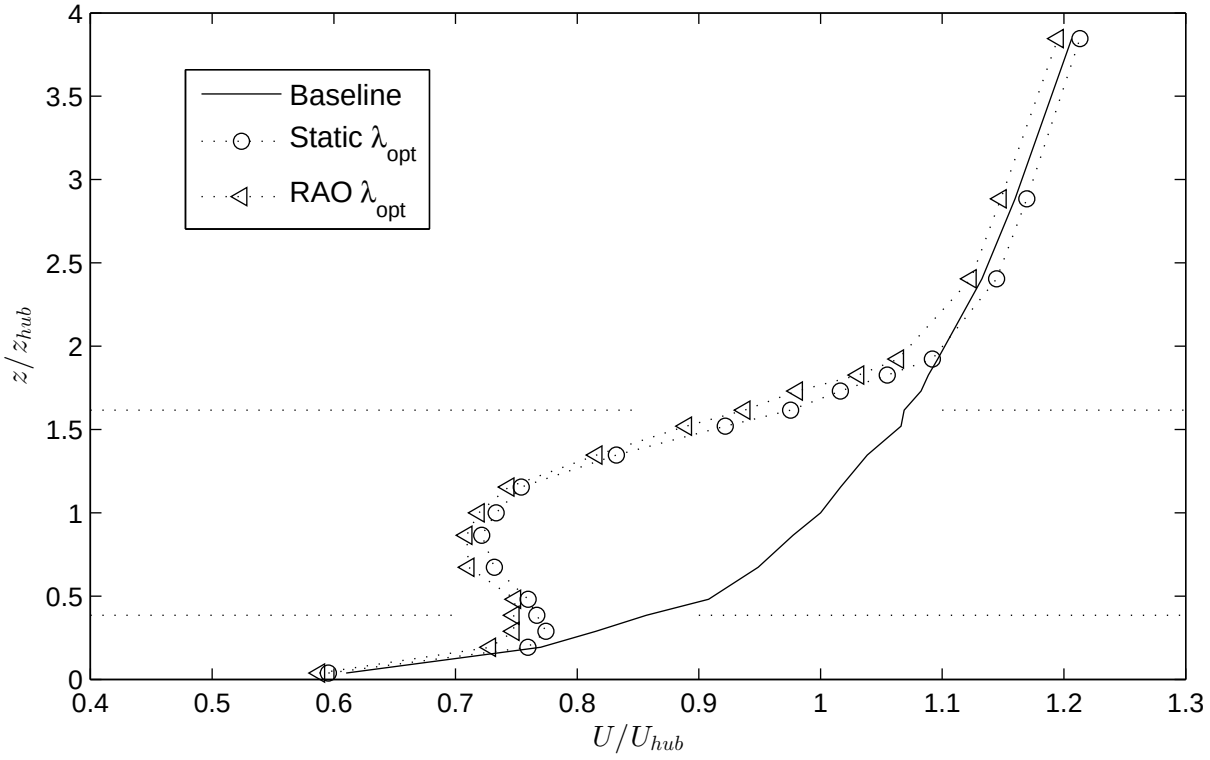

Figure 7.5: Vertical profile of average streamwise velocity $U(z)$ normalized by U_{hub} in the wake measured at $x/D = 5$ and $y/D = 0$ for turbine operating configurations with $\lambda = 3$. Horizontal dotted lines represent bottom and top-tip locations. Baseline - no turbine present

Streamwise and vertical measurements of the average U velocity show minimal variations between the cases. In figure 7.6 spanwise profiles of U/U_{hub} are examined from

PIV measurements. Average streamwise velocities at z_{hub} are shown for the static turbine (black solid line), pitch only (dashed blue line), and heave only (dot-dashed red line) motion cases at (a) $x/D = 2$, (b) $x/D = 3$, and (c) $x/D = 4.5$. Peak velocity reduction is seen along the hub axis with decreasing deficit with increasing magnitude in y, nearly axisymmetric wake about $y = 0$. Wake recovery and expansion can also be observed with increasing x position.

Comparing the results for figure 7.6, virtually no distinction can be observed between the pitch only and heave only cases for locations corresponding with (a), (b), and (c). Weak differences between the two oscillating turbines and that of the static turbine can also be seen. At $x/D = 4.5$ there is a noticeable increase in axisymmetry (for $y = 0$) of the oscillating turbine cases. However, differences between the moving turbine cases and the static turbine are less than 2% of U_{hub} everywhere. Results for spanwise profile of the RAO and static turbine with optimal TSR show no variation between the two cases, results not included here.

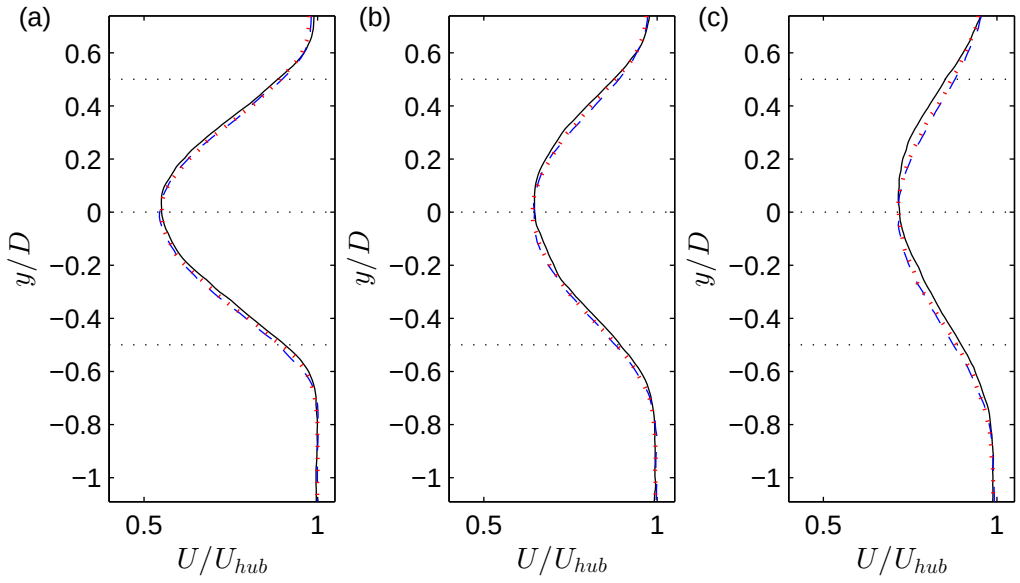

Figure 7.6: Spanwise profiles of average streamwise velocity $U(y)$ normalized by U_{hub} in the wake measured at (a) $x/D = 2$, (b) $x/D = 3$, (c) and $x/D = 4.5$ at the $z = z_{hub}$ plane for turbine operating configurations with $\lambda = 4.5$. Horizontal dotted lines represent the lateral tip locations and the hub axis. Turbine cases shown are the static case (solid black line), pitch only case (dashed blue line), and heave only case (dot-dashed red line)

In general, average streamwise velocities show weak differences in the vertical, spanwise, and streamwise profiles when comparing oscillating to static turbine cases. The weak differences can be quantified as $< 3\%$ of U_{hub} everywhere.

7.3 Streamwise velocity fluctuations

Streamwise velocity fluctuations, u_{rms}, or turbulence intensity I_u are presented in the section. Turbulence intensity is defined as the standard deviation of the wind velocity component, u_rms, divided by the wind velocity at the turbine hub height, U_{hub}:

$$I_u = \frac{u_{rms}}{U_{hub}}. \tag{7.1}$$

Figure 7.7 shows the vertical profile of I_u at $x/D = 5$ and $y = 0$. With the turbine present, a large increase in turbulence intensity is seen near the top-tip, for all motion cases. This is explained by the strong mean shear seen in the $U(z)$ profile with the turbine present. Near the bottom tip, a reduction in I_u is observed, which is similarly explained by a weak mean shear in the $U(z)$ profile, with the turbine present.

In general, the various turbine motion cases, oscillating or static, show very similar trends in the turbulence intensity for the vertical profiles seen in figure 7.7. Weak differences, when comparing a static case to an oscillating case, are observed. The weak differences can be quantified as variations in u_rms of less than 2% with respect to static turbine. However, a relatively large difference is observed at a single point just above the top-tip location where an increase in u_{rms} of 8% for the RAO case as compared to the static turbine.

As with the vertical profiles of u_{rms}, streamwise profiles show similar trends between the oscillating and static turbine cases. Figure 7.8 gives the results for streamwise measurement positions of u_{rms} at $x/D = 1, 2, 3, 4$, and 5 at $y = 0$ and (a) $z = z_{hub}$ and (b) $z = z_{top-tip}$. At the top-tip location, the RAO motion case shows an increase in u_{rms} of 3% over the static turbine with optimal TSR for positions $x/D = 2$ and 3. Along the hub axis, figure 7.8 (a), results are more complex to interpret as the oversized hub has a large influence on the wake structures in the near wake, near wake is considered as $x/D < 2$. Even so, both the static turbine and oscillating turbine cases agree well with each other.

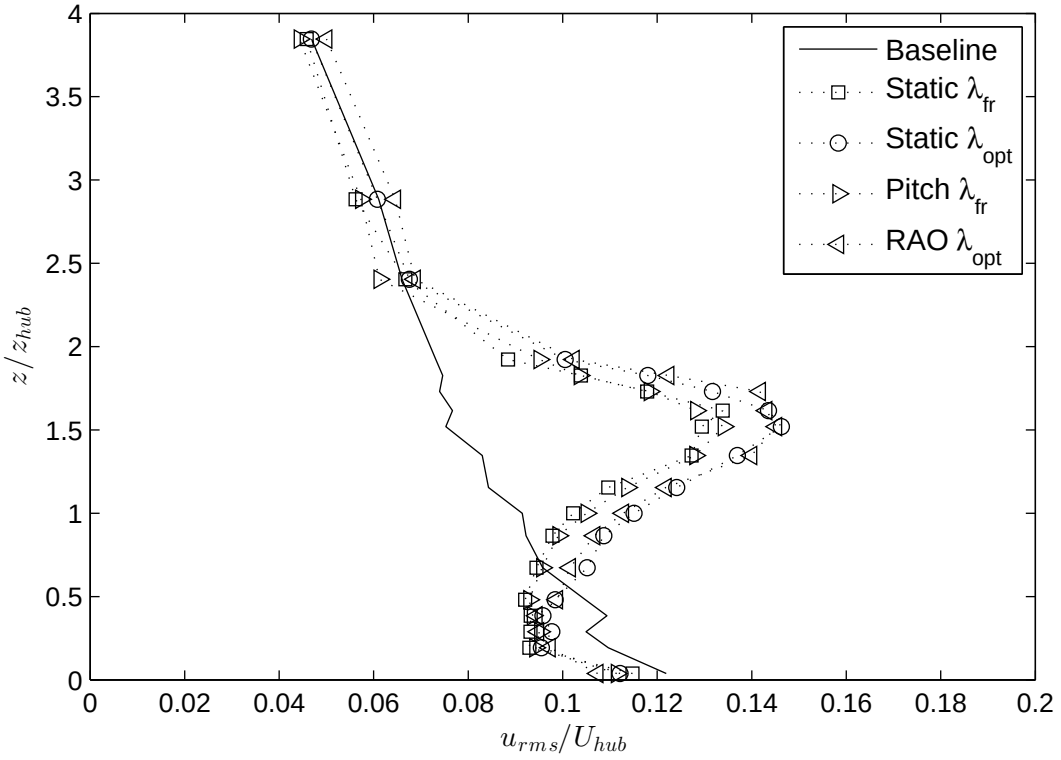

Figure 7.7: Vertical profile of streamwise turbulence intensity, u_{rms}/U_{hub}, in the wake measured at $x/D = 5$ and $y = 0$. Baseline case indicates measurements with no turbine present

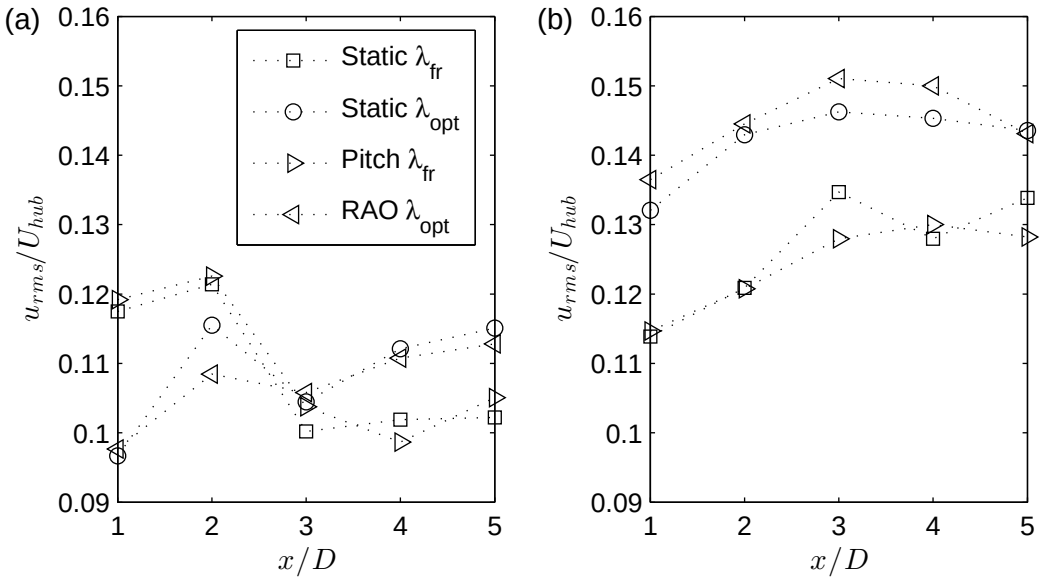

Figure 7.8: Streamwise profiles of turbulence intensity, u_{rms}/U_{hub}, in the wake measured at $x/D = 1, 2, 3, 4$, and 5 at $y = 0$ and (a) $z = z_{hub}$ and (b) $z = z_{top-tip}$

Overall, streamwise velocity fluctuations show weak differences between static and oscillating cases. Within the span of the rotor, differences, of u_{rms}, of $< 3\%$ are observed. A maximum difference of 8% is seen outside the rotor span, just above the top-tip location. This large difference is likely a result of the dynamic top-tip location for the fluctuating turbine.

7.4 Turbine phases statistics

As was presented in §7.2 and §7.3, the mean and fluctuating streamwise velocity statistics between the oscillating and static turbine motion cases do not present any significant differences. This raises the question whether or not turbine motion phases, or position states and direction of travel in heave and/or pitch, have opposing trends on the velocity statistics. For example, a pitching turbine into the wind will impinge the flow creating an increased velocity deficit whereas a turbine pitching with the flow will reduce the velocity deficit. This section will investigate streamwise velocity statistics based on turbine motion phases. That is, conditional statistics based on turbine position and travel

direction.

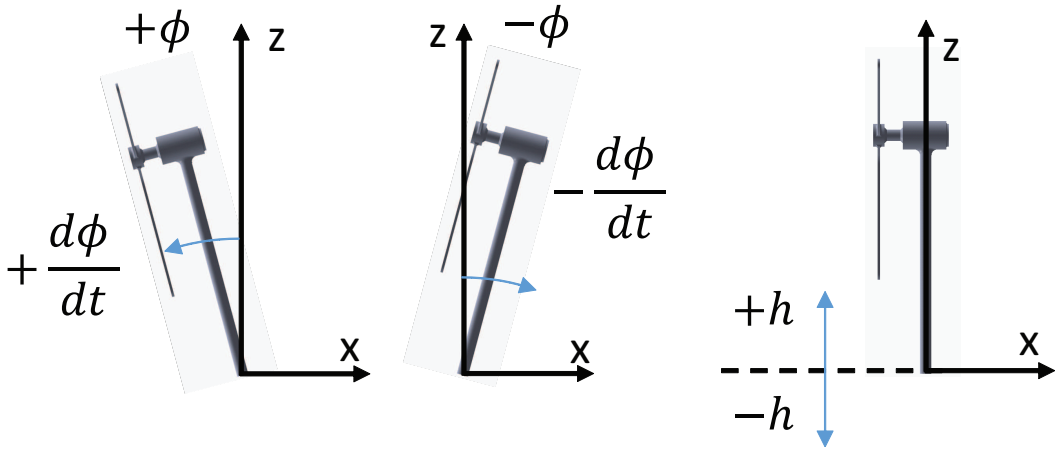

Figure 7.9: Schematic of wind turbine motion phases

The turbine motion phases investigated in this section are based on two states of the model turbine. These two motion phases then create a condition on which statistics are performed on the streamwise velocity component. Turbine phases are also split into two categories based on whether the turbine is undergoing oscillations in pitch or heave. The turbine phases are outlined as follows for pitch:

- positive direction of travel in pitch, $+d\phi/dt$, and positive values of pitch, $+\phi$ (positive phase)
- negative direction of travel in pitch, $-d\phi/dt$, and negative values of pitch, $-\phi$ (negative phase).

Illustration of the pitch phases can be seen in the figure 7.9 with the left and middle images. Similarly, the motion phases for heave are given as:

- positive direction of travel in heave, $+dh/dt$, and positive values of heave, $+h$ (positive phase)
- negative direction of travel in heave, $-dh/dt$, and negative values of heave, $-h$ (negative phase).

The right image in figure 7.9 defines the positive and negative values and motion of heave.

Instantaneous velocity measurements, $u(t)$, from PIV and hotwire results are binned into the two conditions based on the turbine phase. For the pitch only case, velocities were binned based on the pitch phases creating two categories which will be termed $u_{\phi+}$ for positive motion and value of pitch and $u_{\phi-}$ for the negative. Similarly, the heave only case was binned based on heave phases and results in bins for instantaneous velocities u_{h+} and u_{h-}. The RAO case includes binning based on heave and pitch.

Statistics were then performed on each bin of instantaneous velocities for each motion case. Specifically an average streamwise velocity and fluctuation from the mean. These statistics are termed U_ϕ for the averaging based on pitch, U_h for heave based averaging and $u_{rms,\phi}$ and $u_{rms,\phi}$ for pitch and heave based standard deviation of the velocity fluctuations. Each statistic has a value associated with the defined positive phase and negative phase, two values total.

Phase statistics are then used to determine a difference between the velocity statistic based on a motion phase and that of the overall velocity statistic. As applied to the average velocity, this is termed as the phase average velocity difference and is defined as

$$\Delta U_\xi(x_i) = U_\xi(x_i) - U(x_i), \tag{7.2}$$

where $\Delta U_\xi(x_i)$ is the phase average velocity difference for measurement position x_i of a specific motion case (i.e. RAO case) with the phase averaging based on ξ. ξ represents either pitch, ϕ, or heave, h. $U_\xi(x_i)$ is the phase average streamwise velocity and $U(x_i)$ is the overall average. The phase average difference is used to give insight into any large scale fluctuations in the mean flow. $\Delta U_\xi(x_i)$ is non-dimensionalized by $u_{rms}(x = 5D, y = 0, z = z_{hub})$ of the static turbine in order to compare it's value with the turbulence intensity present in the flow of the static turbine. $u_{rms}(x = 5D, y = 0, z = z_{hub})$ will either have a value associated with the free-spinning rotor static case or the optimal TSR static case, depending on what oscillating turbine case is being discussed.

Figures 7.10, 7.11, 7.12, and 7.13 give contours of the phase average streamwise velocity difference, $\Delta U_\xi(x, y)$, from wall-parallel PIV located in the hub plane for the cases summarized in table 7.1. In each of the figures, (a) gives the positive phase and (b) the negative phase of the turbine position. Results where a pitching motion is present, i.e. pitch only and RAO (figures 7.10, 7.12, and 7.13), show clear, opposing trends in the

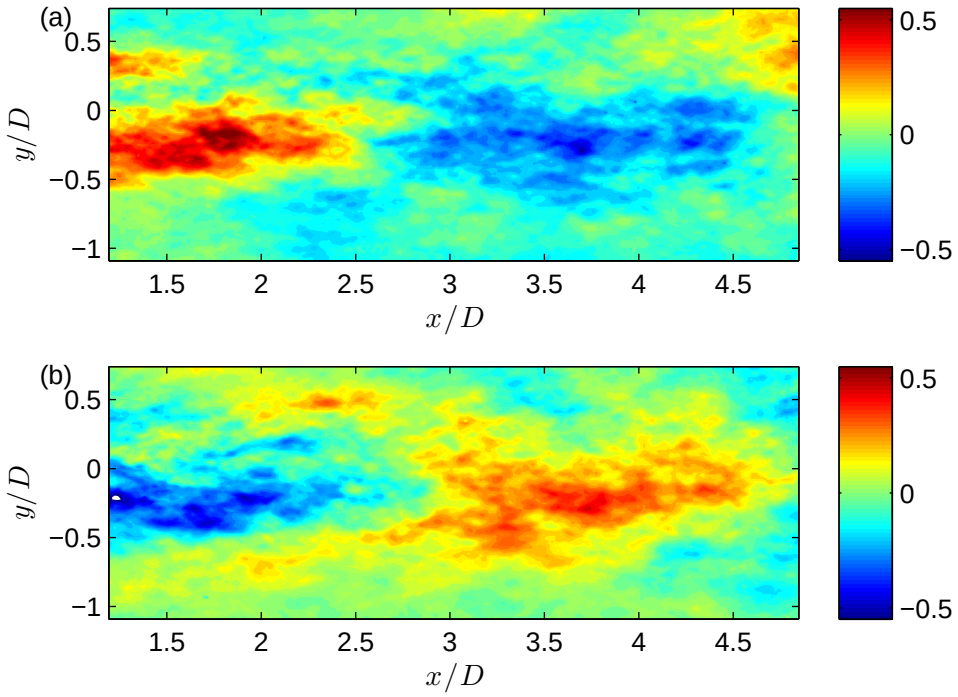

Figure 7.10: Contours of phase average streamwise velocity difference, $\Delta U_\phi(x, y)/u_{rms}$, for pitch only case at $z = z_{hub}$ plane, (a) positive phase, (b) negative phase. ΔU_ϕ is normalized by $u_{rms}(x = 5D, y = 0, z = z_{hub})$ of the static turbine

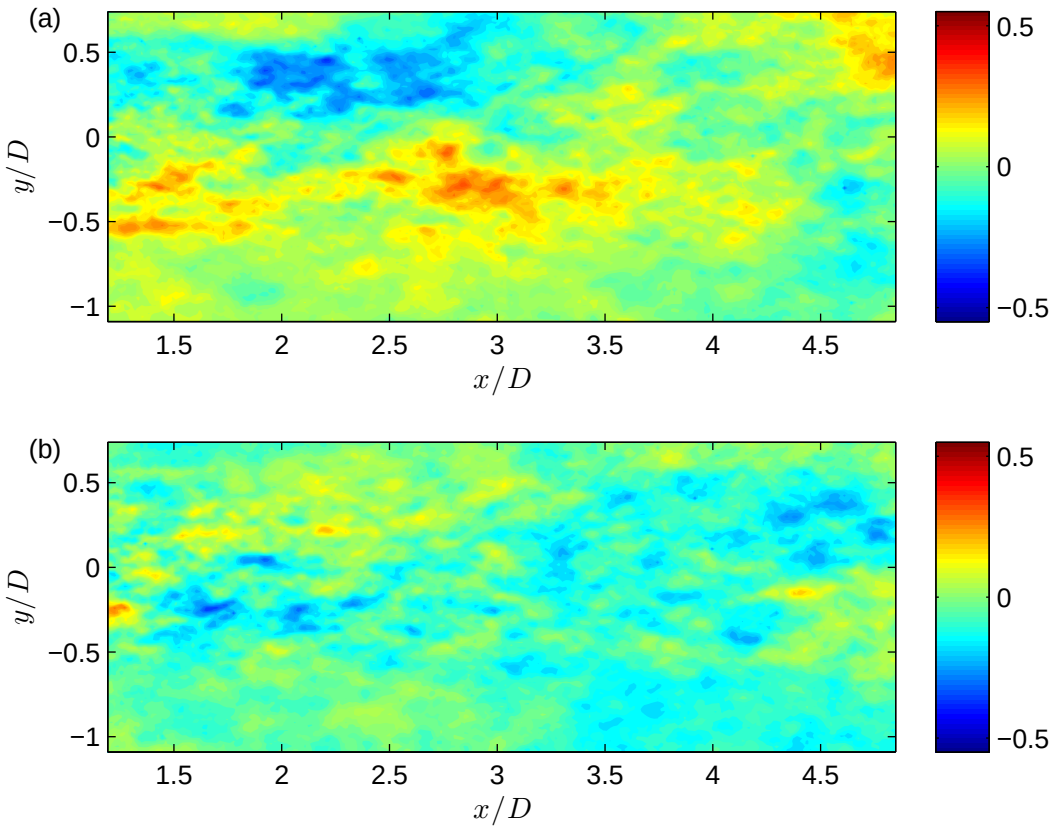

Figure 7.11: Contours of phase average streamwise velocity difference, $\Delta U_h(x, y)/u_{rms}$, for heave only case at $z = z_{hub}$ plane, (a) positive phase, (b) negative phase. ΔU_h is normalized by $u_{rms}(x = 5D, y = 0, z = z_{hub})$ of the static turbine

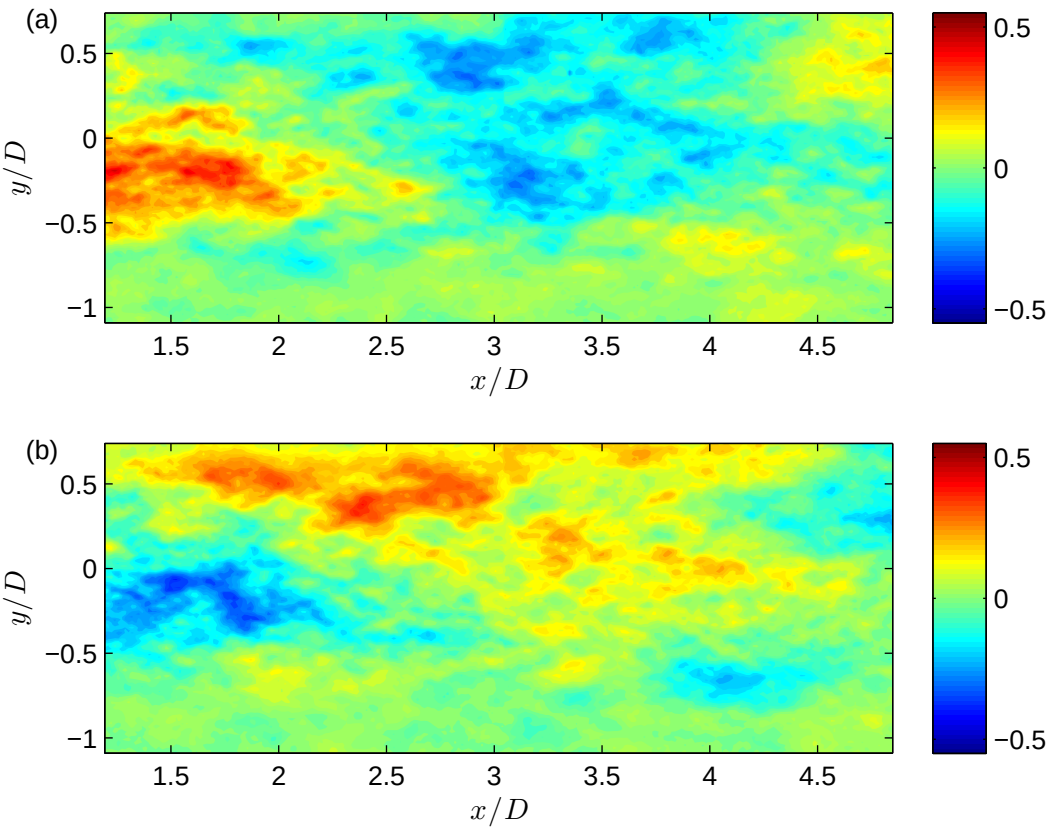

Figure 7.12: Contours of phase average streamwise velocity difference, $\Delta U_\phi(x, y)/u_{rms}$, for RAO case with pitch conditioning at $z = z_{hub}$ plane, (a) positive phase, (b) negative phase. ΔU_ϕ is normalized by $u_{rms}(x = 5D, y = 0, z = z_{hub})$ of the static turbine

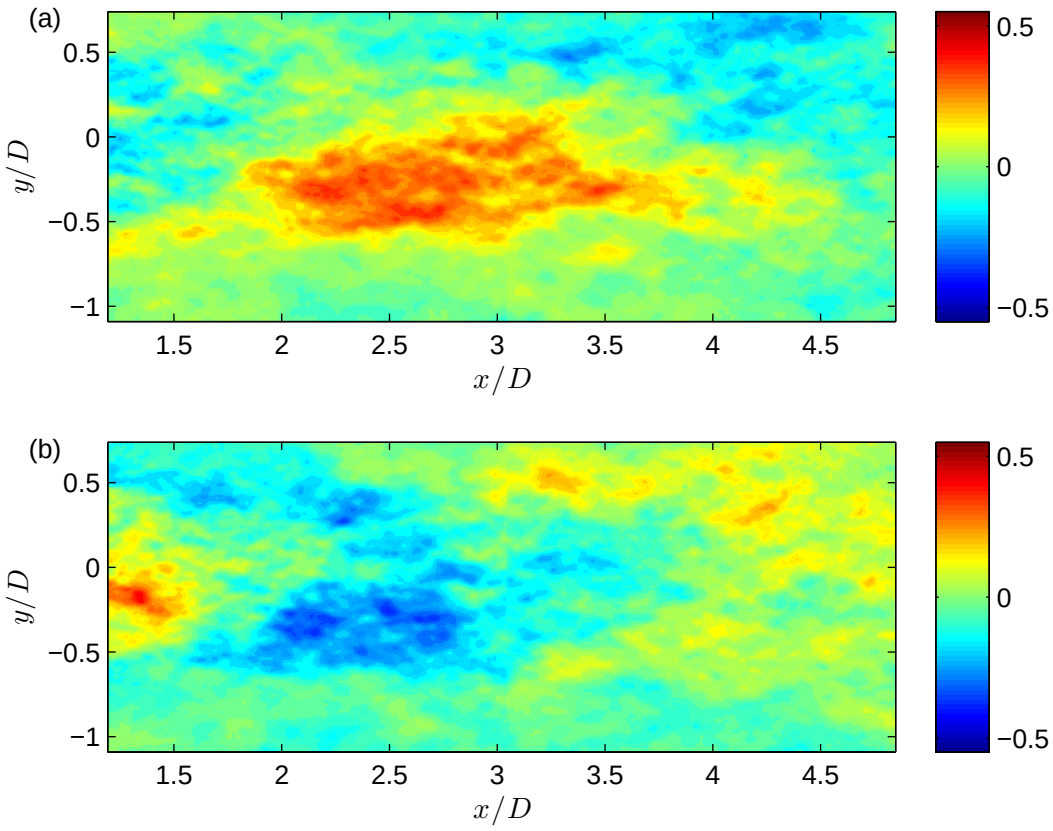

Figure 7.13: Contours of phase average streamwise velocity difference, $\Delta U_h(x, y)/u_{rms}$, for RAO case with heave conditioning at $z = z_{hub}$ plane, (a) positive phase, (b) negative phase. ΔU_h is normalized by $u_{rms}(x = 5D, y = 0, z = z_{hub})$ of the static turbine

spatial distribution of the streamwise velocity between turbine phases. That is, a pocket of velocity reduction is seen in figure 7.10 (a) located in the range of $x/D = [3-4.5]$ with a value of $(-)30-40\%$ of u_{rms}. This same region is characterized by a velocity increase of $(+)30-40\%$ of u_{rms} as seen in figure 7.10 (b) which corresponds with the negative phase, indicating phase specific velocity fluctuations. The velocity pockets are biased towards the $(-)y$ direction approximately spanning from $y/D = [-0.5$ to $0.25]$. The spatial and motion phase velocity trends can also be observed in figure 7.14, streamwise cuts from the contour plots for $\Delta U_\xi(x)$ at $y = 0$ (hub axis). The phase specific velocity trends are easily observed in subfigures (a), (b), and (c) which correspond with the pitch only case and the RAO case with pitch conditioning and heave conditioning, respectively.

Coupling of the pitch and heave motions in the RAO case results in a less defined spatial velocity distribution for the phase specific $\Delta U_\xi(x, y)$. This is evident in figures 7.12 and 7.13. However, phase specific fluctuations, $\Delta U_\xi(x, y)$, of $\pm 30-40\%$ are still observed. Figure 7.11 shows results of $\Delta U_h(x, y)$ for the heave only case. In the hub plane, there are no clear trends between the motion phases indicating the heaving motion alone has limited effect on the velocity in the hub plane.

Vertical profiles, at $x/D = 5$ and $y = 0$, and streamwise profiles, at $y = 0$ and $z = z_{hub}$ and $z_{top-tip}$, from hotwire measurements show similar opposing trends for ΔU_ϕ, seen in figures 7.15 and 7.16. Important to note is that the results for ΔU_ϕ are phase and measurement location specific. That is, depending on the condition chosen, i.e. the positive and negative phases used here, the window of time used to look at the flow field for a specific turbine position or motion direction will vary the location and magnitude of the so called velocity pockets. These pockets are a result of the phase oscillation of the streamwise velocity which has a 2D ($xandz$ planes) spatial structure like a wave. This wave propagates through the wake and depending on the measurement location and turbine phase, different amplitudes of the fluctuations will be recorded. The lengthscale of the wave, as can be approximated from figures 7.14 and 7.16, is $L \approx 3-4D$.

The vertical profiles shown in figure 7.15 show the influence of the coupled motion for heave and pitch. Figure 7.15 (a) gives the results of ΔU_ϕ for the pitch only case. The largest variation in velocity between the two phases is observed near z_{hub}. In contrast,

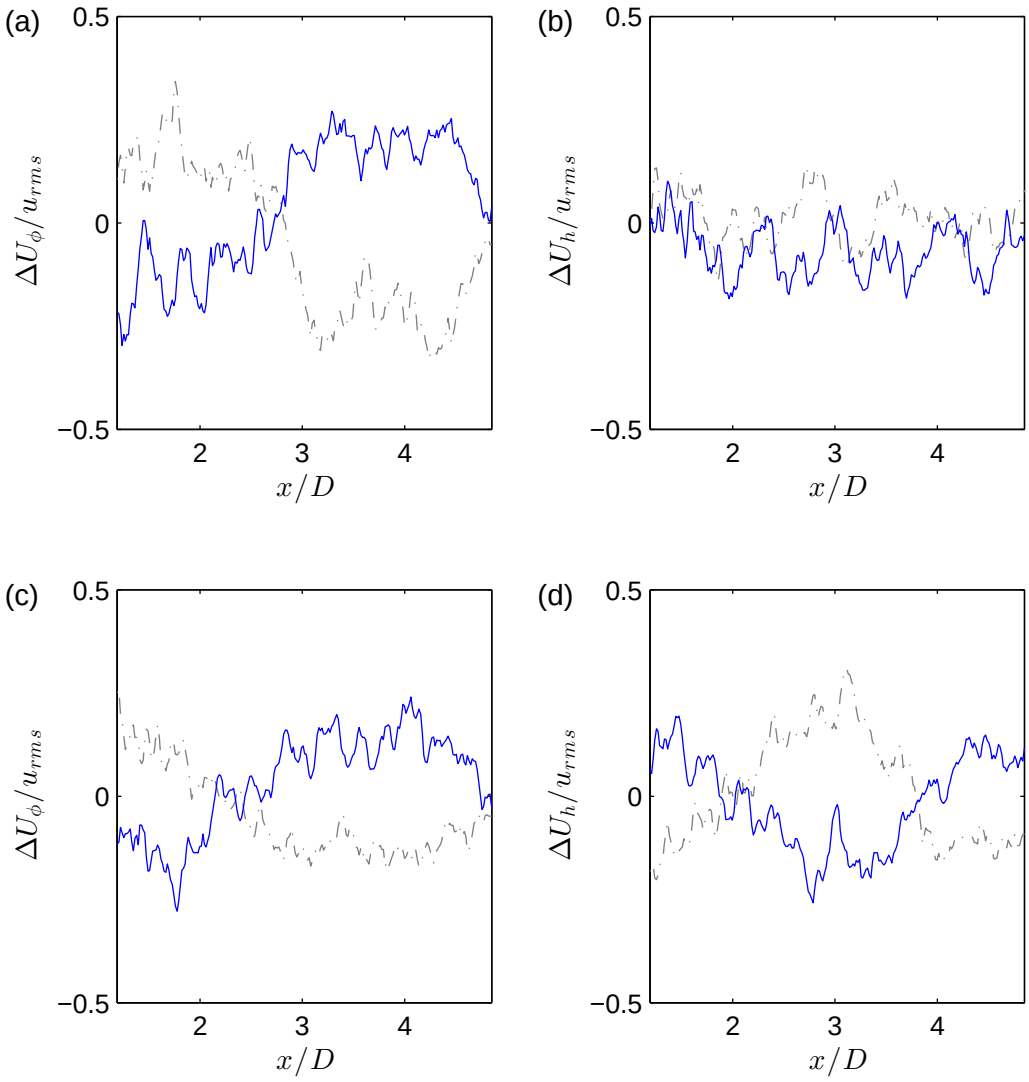

Figure 7.14: Phase average streamwise velocity difference, streamwise profile at $z = z_{hub}$ and $y = 0$, $\Delta U_\xi(x)/u_{rms}$ for (a) pitch only $\xi = \phi$, (b) heave only $\xi = h$, (c) RAO $\xi = \phi$, and (d) RAO $\xi = h$. ΔU_ξ is normalized by $u_{rms}(x = 5D, y = 0, z = z_{hub})$ of the static turbine. Sold blue line represents positive phase, dash-dot gray line negative phase

the RAO case shown in figure 7.15 (b) has minimal velocity variations near z_{hub} and largest values near the rotor tips, $z_{top-tip}$ and $z_{bottom-tip}$. General conclusions about phase average velocity difference are, the positive and negative turbine phases have opposite signs for $\Delta U_\phi(x_i)$ which results in a cancelling effect and minimal differences are observed of the average U velocity between the static and oscillating turbine cases. The resulting fluctuation, $\Delta U_\phi(x_i)$, is a wave like structure with lengthscale $L \approx 3-4D$. Measurement position and phase condition highly influence the observed velocity fluctuations. The amplitude of $\Delta U_\phi(x_i)$ is relatively small (30-40%) as compared to the standard deviation of the mean velocity. However, the flow variations associated with the turbine movement is organized/predictable and has a large lengthscale.

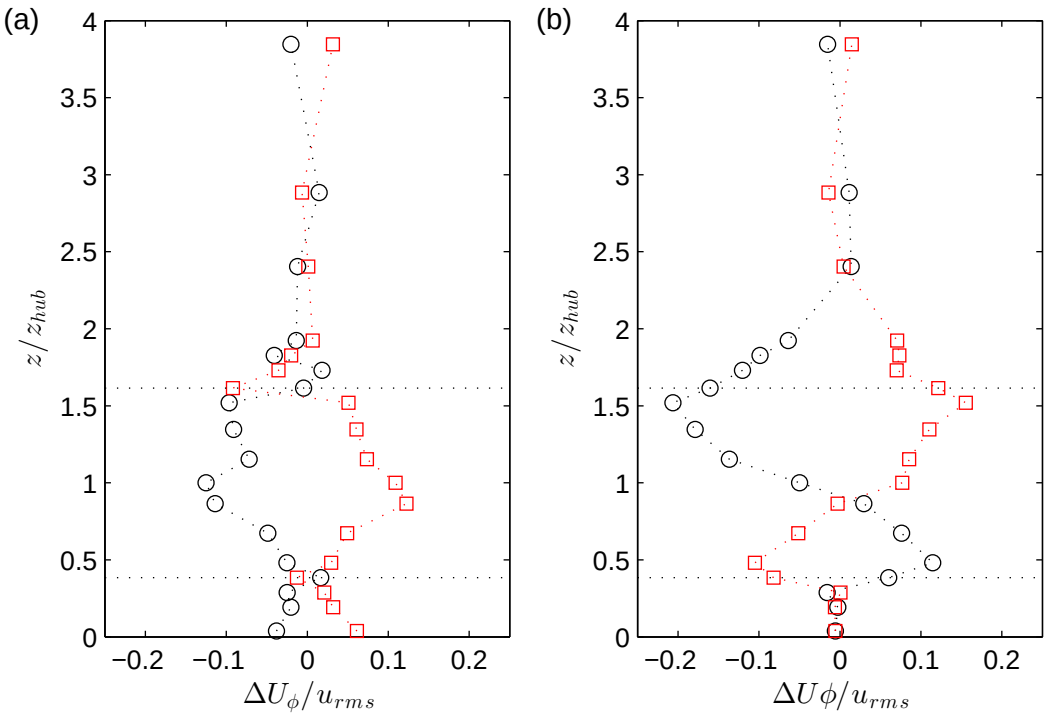

Figure 7.15: Phase average streamwise velocity difference, vertical profile at $x/D = 5$ and $y = 0$, $\Delta U_\phi(z)/u_{rms}$ for (a) pitch only and (b) RAO (pitch conditioning). ΔU_ϕ is normalized by $u_{rms}(x = 5D, y = 0, z = z_{hub})$ of the static turbine. Black cirlce: positive phase, red square: negative phase

An organized, large scale fluctuation with a significant amplitude resulting from the

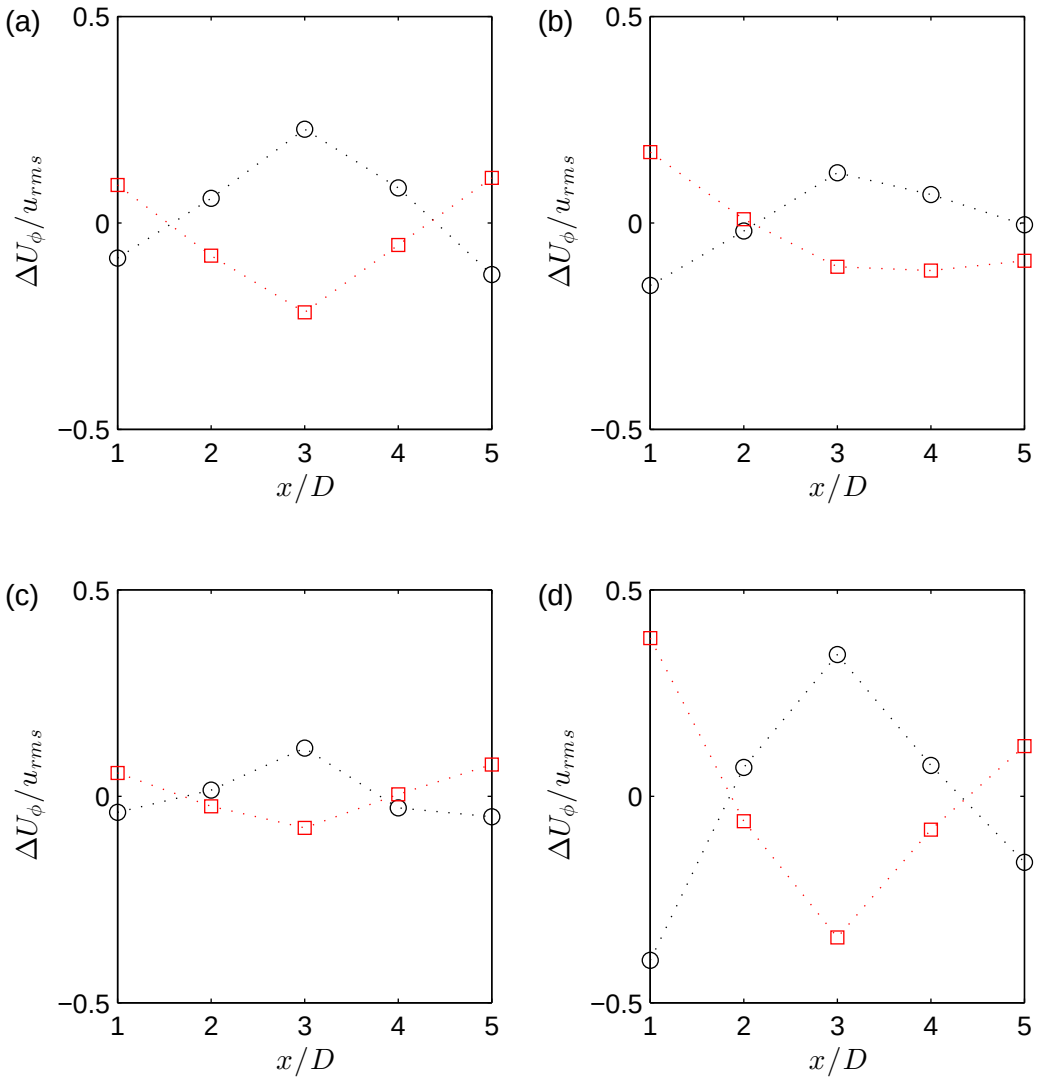

Figure 7.16: Phase average streamwise velocity difference, streamwise profiles at $y = 0$. $\Delta U_\phi(x)/u_{rms}$ for (a) pitch only $z = z_{hub}$, (b) pitch only $z = z_{top-tip}$, (c) RAO $z = z_{hub}$, and (d) RAO $z = z_{top-tip}$. ΔU_ϕ is normalized by $u_{rms}(x = 5D, y = 0, z = z_{hub})$ of the static turbine. Black cirlce: positive phase, red square: negative phase

turbine motion is present, however, this raises the question why there is not a significant increase in u_{rms} over the static turbine. To understand why, the phase average difference is applied to u_rms velocity and is similarly defined as

$$\Delta u_{rms,\xi} = u_{rms,\xi} - u_{rms}, \tag{7.3}$$

where $u_{rms,\xi}$ is the phase specific rms velocity, has a value associated with the negative phase and positive phase defined earlier, and u_{rms} is the overall rms velocity for each case. As with U_ξ, $u_{rms,\xi}$ is determined from the binned, instantaneous velocities and binning is based on turbine phase. $\Delta u_{rms,\xi}$ is also normalized by $u_{rms}(x = 5D, y = 0, z = z_{hub})$ of the static turbine, either the free-spinning or optimal TSR case.

The phase specific $\Delta u_{rms,\phi}$ profiles are given in figures 7.17 and 7.18. As was observed in the profiles of ΔU_ϕ, opposite values of $\Delta u_{rms,\phi}$ are associated with the positive and negative phases in both the vertical and streamwise profiles. These fluctuations in $\Delta u_{rms,\phi}$ result in a cancelling effect on the overall u_{rms} and accounts for the minimal differences between the static and oscillating turbine profiles of u_{rms}. Comparing the positive phase value of ΔU_ϕ in figure 7.15 (b) and the positive phase value of $\Delta u_{rms,\phi}$ in figure 7.17 (b), a clear trend can be observed. Negative values of ΔU_ϕ correspond with a positive $\Delta u_{rms,\phi}$, most notably shown near the top-tip location. Likewise, positive values of ΔU_ϕ are associated with a negative $\Delta u_{rms,\phi}$, or a decrease in rms velocity. This same trend is observed in the negative phase statistics as well as in the streamwise profiles shown in figures 7.16 and 7.18.

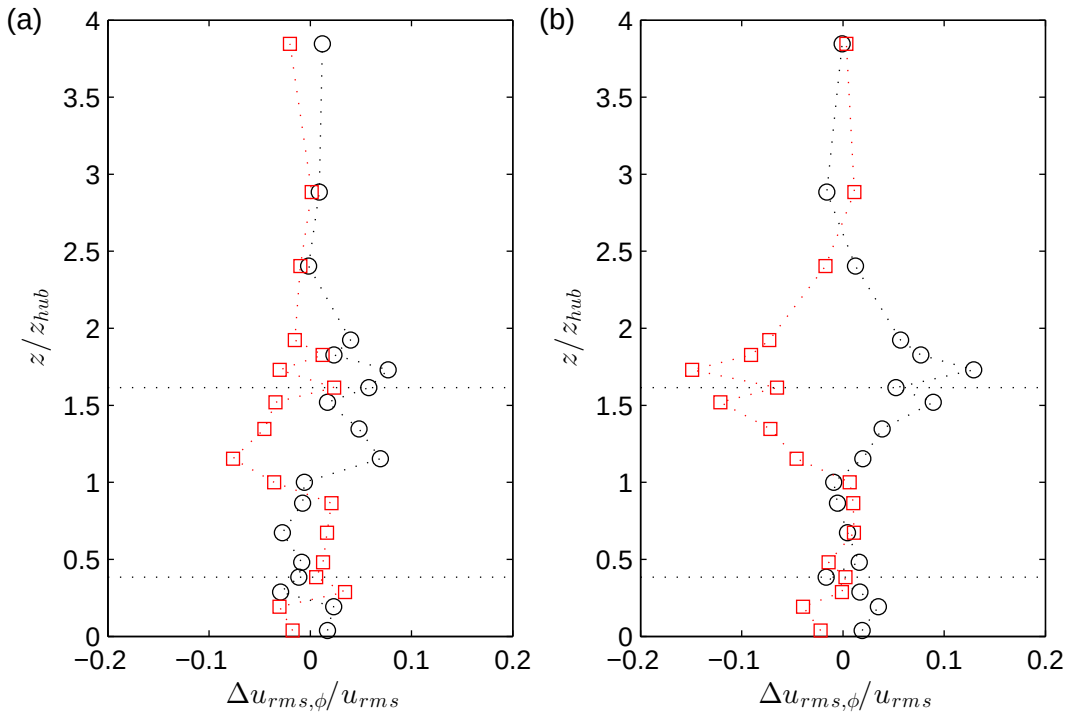

Figure 7.17: $\Delta u_{rms,\phi}$ vertical profile at $x/D = 5$ and $y = 0$, (a) pitch only and (b) RAO (pitch conditioning). $\Delta u_{rms,\phi}$ is normalized by $u_{rms}(x = 5D, y = 0, z = z_{hub})$ of the static turbine. Black circle: positive phase, red square: negative phase

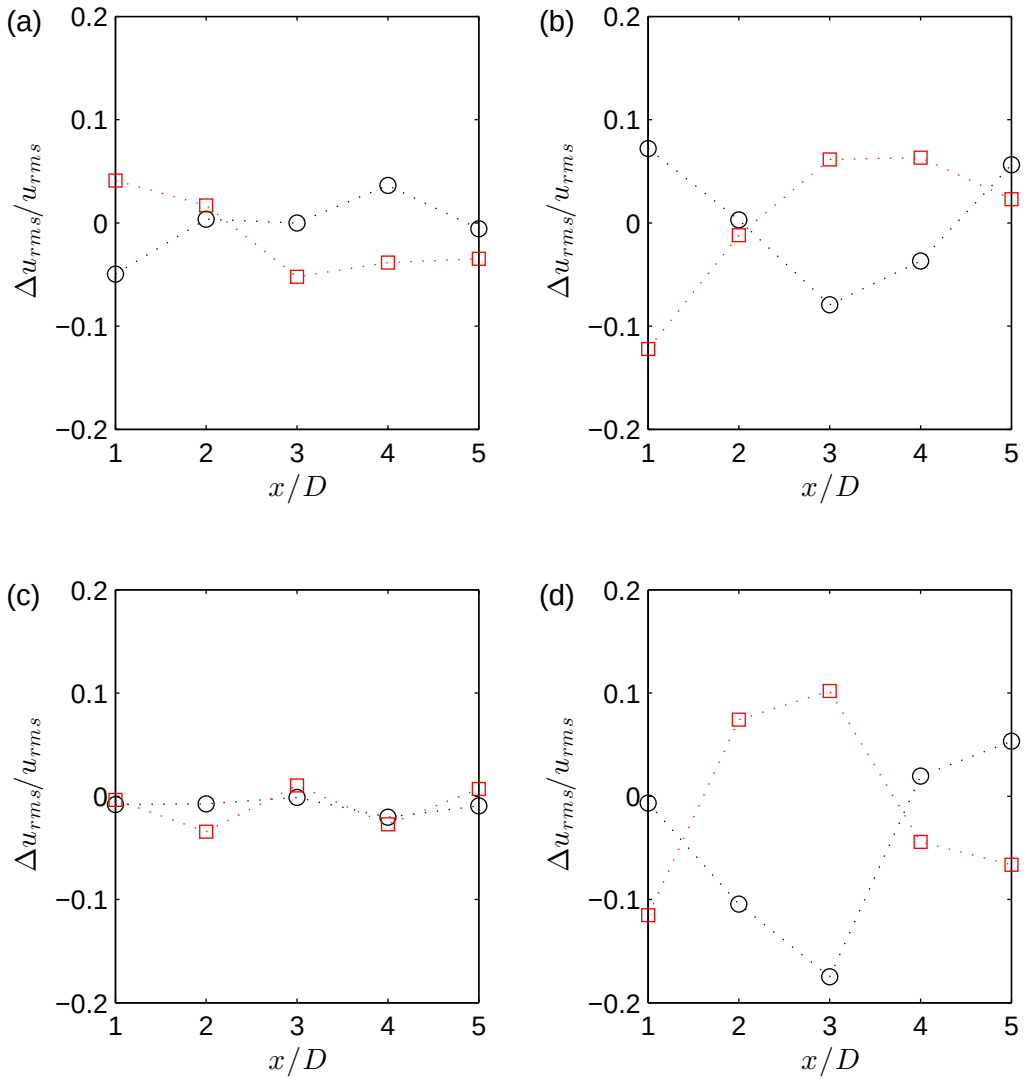

Figure 7.18: $\Delta u_{rms,\phi}$ streamwise profiles at $y = 0$ for (a) pitch only $z = z_{hub}$, (b) pitch only $z = z_{top-tip}$, (c) RAO $z = z_{hub}$, and (d) RAO $z = z_{top-tip}$. $\Delta u_{rms,\phi}$ is normalized by $u_{rms}(x = 5D, y = 0, z = z_{hub})$ of the static turbine. Black circle: positive phase, red square: negative phase

Chapter 8

Conclusion and Discussion

An experimental investigation on the aerodynamic wake behind a pitching and/or heaving model wind turbine was performed. The study was split into two quasi-coupled phases; the first phase characterized the motion of a offshore floating wind turbine subjected to linear wave forcing, the second phase replicated specific motion cases, which were driven by results from the first phase, on a model wind turbine within a turbulent boundary layer. The following is an overview of the quasi-coupled relationship:

1. model offshore floating wind turbine was subjected to wave forcing and pitch and heave motions were recorded
   - prototype to wave basin scale using geometric scale factor of 1:100 and Froude number similarity
   - wave environment was a representation of data gathered from the Pacific Northwest
2. response amplitude operator (RAO) was generated for pitch and heave due to a given wave period and height
   - a point on the RAO will be chosen to investigate in the wind tunnel
3. heave and pitch amplitude and frequency is scaled to the wind tunnel and implemented in motion control software

- $h(t)$ and $\phi(t)$ are scaled up from wave basin to prototype scale (Froude similarity), then scaled to wind tunnel scale using geometric similarity, ratio w.r.t. rotor diameter (1/1562.5)
- Strouhal number used to determine frequency of h and ϕ at wind tunnel scale (3 Hz at $U_{hub} = 2.5$ m s^{-1})
- h and ϕ are transformed into motor position commands

4. turbine motion is realized within the turbulent boundary layer

5. wake measurements, PIV and hotwire, are performed and synced in time with turbine position.

Wake measurements were made in an effort to quantify fluctuations in the flow associated with the motion of the turbine. Weak differences were observed in the mean, streamwise velocity and turbulent fluctuations between the static and oscillating turbine cases, $< 3\%$ of U_{hub} everywhere. These weak differences were a result of opposing trends in the mean and fluctuating velocity quantities based on turbine motion phases. The wake oscillations created by the turbine motion was characteristic of a 2D wave (with convection in the x plane and amplitude in the z plane) with a relatively small amplitude as compared to u_rms, ΔU_ξ value of $\pm 30 - 40\%$ of the u_{rms} for the static turbine. However, the lengthscale of the oscillation is relatively large, $3 - 4$ rotor diameters, and organized with respect to the wave frequency. Therefore, the turbine structure and controls (generator and blade pitch control) should perceive the fluctuations and make corrections.

References

[1] DOE, "20% wind energy by 2030: Increasing wind energys contribution to us electricity supply," tech. rep., U.S. Department of Energy, 2008.

[2] W. Musial and B. Ram, "Large-scale offshore wind power in the united states: Assessment of opportunities and barriers," tech. rep., National Renewable Energy Laboratory (NREL), Golden, CO., 2010.

[3] D. Roddier, C. Cermelli, A. Aubault, and A. Weinstein, "Windfloat: A floating foundation for offshore wind turbines," *Journal of Renewable and Sustainable Energy*, vol. 2, no. 3, p. 033104, 2010.

[4] C. P. Butterfield, W. Musial, J. Jonkman, P. Sclavounos, and L. Wayman, *Engineering challenges for floating offshore wind turbines*. National Renewable Energy Laboratory, 2007.

[5] Y. Sheinman and A. Rosen, "A dynamic model of the influence of turbulence on the power output of a wind turbine," *Journal of Wind Engineering and Industrial Aerodynamics*, vol. 39, no. 1, pp. 329–341, 1992.

[6] S. B. Pope, *Turbulent flows*. Cambridge university press, 2000.

[7] L. Vermeer, J. N. Sørensen, and A. Crespo, "Wind turbine wake aerodynamics," *Progress in aerospace sciences*, vol. 39, no. 6, pp. 467–510, 2003.

[8] L. P. Chamorro and F. Porté-Agel, "A wind-tunnel investigation of wind-turbine wakes: boundary-layer turbulence effects," *Boundary-layer meteorology*, vol. 132, no. 1, pp. 129–149, 2009.

[9] L. Chamorro, M. Guala, R. Arndt, and F. Sotiropoulos, "On the evolution of turbulent scales in the wake of a wind turbine model," *Journal of Turbulence*, no. 13, 2012.

[10] A. Singh, K. B. Howard, and M. Guala, "On the homogenization of turbulent flow structures in the wake of a model wind turbine," *Physics of Fluids (1994-present)*, vol. 26, no. 2, p. 025103, 2014.

[11] K. Howard, J. Hu, L. Chamorro, and M. Guala, "Characterizing the response of a wind turbine model under complex inflow conditions," *Wind Energy*, 2014.

[12] X. Yang, K. B. Howard, M. Guala, and F. Sotiropoulos, "Effects of a three-dimensional hill on the wake characteristics of a model wind turbine," *Bulletin of the American Physical Society*, vol. 59, 2014.

[13] J. Hong, M. Toloui, L. P. Chamorro, M. Guala, K. Howard, S. Riley, J. Tucker, and F. Sotiropoulos, "Natural snowfall reveals large-scale flow structures in the wake of a 2.5-mw wind turbine," *Nature communications*, vol. 5, 2014.

[14] R. B. Cal, J. Lebrón, L. Castillo, H. S. Kang, and C. Meneveau, "Experimental study of the horizontally averaged flow structure in a model wind-turbine array boundary layer," *Journal of Renewable and Sustainable Energy*, vol. 2, no. 1, p. 013106, 2010.

[15] X. Yang, S. Kang, and F. Sotiropoulos, "Computational study and modeling of turbine spacing effects in infinite aligned wind farms," *Physics of Fluids (1994-present)*, vol. 24, no. 11, p. 115107, 2012.

[16] L. P. Chamorro, R. Arndt, and F. Sotiropoulos, "Turbulent flow properties around a staggered wind farm," *Boundary-layer meteorology*, vol. 141, no. 3, pp. 349–367, 2011.

[17] L. P. Chamorro and F. Porté-Agel, "Turbulent flow inside and above a wind farm: a wind-tunnel study," *Energies*, vol. 4, no. 11, pp. 1916–1936, 2011.

[18] D. Yang, C. Meneveau, and L. Shen, "Effect of downwind swells on offshore wind energy harvesting–a large-eddy simulation study," *Renewable Energy*, 2014.

[19] D. Yang, C. Meneveau, and L. Shen, "Large-eddy simulation of offshore wind farm," *Physics of Fluids (1994-present)*, vol. 26, no. 2, p. 025101, 2014.

[20] D. T. Griffith and T. D. Ashwill, "The sandia 100-meter all-glass baseline wind turbine blade: Snl100-00," *SAND2011-3779, Sandia National Laboratories, Albuquerque, June*, 2011.

[21] S. Chakrabarti, *Handbook of Offshore Engineering (2-volume set)*. Elsevier, 2005.

[22] E. Wayman, P. Sclavounos, S. Butterfield, J. Jonkman, W. Musial, *et al.*, "Coupled dynamic modeling of floating wind turbine systems," in *Offshore technology conference*, vol. 139, Houston, 2006.

[23] W. Turbines, "Part 1: Design requirements, iec 61400-1," 2005.

[24] J. Jonkman, "Dynamics modeling and loads analysis of an offshore floating wind turbine," tech. rep., National Renewable Energy Laboratory (NREL), Golden, CO., 2007.

[25] V. L. Okulov, I. V. Naumov, R. F. Mikkelsen, I. K. Kabardin, and J. N. Sørensen, "A regular strouhal number for large-scale instability in the far wake of a rotor," *Journal of Fluid Mechanics*, vol. 747, pp. 369–380, 2014.

[26] K. B. Howard, "Wind turbine performance and wake development for various atmospheric, operational and siting conditions," 2014. Copyright - Copyright ProQuest, UMI Dissertations Publishing 2014; Last updated - 2014-12-04; First page - n/a.

[27] D. Medici and P. Alfredsson, "Measurements on a wind turbine wake: 3d effects and bluff body vortex shedding," *Wind Energy*, vol. 9, no. 3, pp. 219–236, 2006.

[28] L. Chamorro, C. Hill, S. Morton, C. Ellis, R. Arndt, and F. Sotiropoulos, "On the interaction between a turbulent open channel flow and an axial-flow turbine," *Journal of Fluid Mechanics*, vol. 716, pp. 658–670, 2013.

[29] S. Kang, X. Yang, and F. Sotiropoulos, "On the onset of wake meandering for an axial flow turbine in a turbulent open channel flow," *Journal of Fluid Mechanics*, vol. 744, pp. 376–403, 2014.

[30] H. H. Bruun, "Hot-wire anemometry: principles and signal analysis," *Measurement Science and Technology*, vol. 7, no. 10, p. null, 1996.